Predicting seizure spread and neurosurgical outcomes in epilepsy by combining neuroimaging, machine learning, and computer modelling

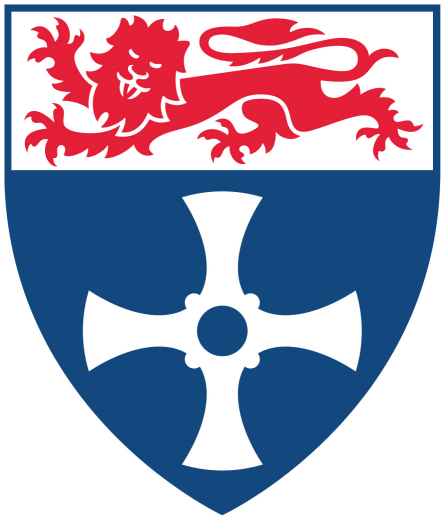

Nishant Sinha

Translational and Clinical Research Institute
Faculty of Medical Sciences
Newcastle University

This thesis is submitted for the degree of
Doctor of Philosophy

July 2021

Abstract

Background: Epilepsy is a neurological disorder of abnormal brain network in which seizures originate and spread via patient-specific spatial and temporal pathways. Disrupting these epileptic networks can enable seizure control; therefore, it is crucial to map, quantify, and understand these networks. This thesis aims to quantify the whole-brain structural network abnormalities of patients with focal and generalised epilepsy along with patient-specific network disruptions caused by epilepsy surgery.

Method: We developed a novel patient-specific metric to quantify structural network abnormality at every brain region by standardising whole-brain structural networks of patients with healthy structural networks. To quantify local changes in the white-matter structure, we applied quantitative neuroimaging techniques and a computational model for making predictions on mechanisms of epilepsy development. We combined the network-based measures in robust cross-validated machine learning models to predict neurosurgical outcomes and seizure spread.

Results: In drug-resistant focal epilepsy patients, structural network abnormality associated with post-surgical seizure recurrence and patient history of focal to bilateral tonic-clonic seizures. Combined with routinely acquired clinical variables, we predicted the patient-specific probability of seizure recurrence after surgery. In patients with idiopathic generalised epilepsy, we found localised abnormalities in major white-matter fascicles. The thalamocortical computer model of spike-wave seizures implicated the role of cortico-reticular connections in mechanism of epileptogenesis.

Significance: This thesis highlighted the heterogeneity between patients that may be making them susceptible to a varied response for the same treatment. We offer practical tools to quantify these heterogeneities to complement clinical decision-making for effective patient stratification and tailored treatments.

Dedicated to Priyansh, Reyansh, and Swara.

Acknowledgements

I am grateful to my supervisor Peter Taylor for his guidance, inspiration, and constant support throughout this PhD and before. Peter provided me with an excellent research environment in his lab, a generous amount of time for scientific discussions, and freedom to explore whilst keeping a check that I do not diverge too much. Many thanks to the funding and support from the Research Excellence Academy Faculty of Medical Sciences and School of Computing that enabled me to undertake this work.

I want to thank my mentors, Yujiang Wang, Rob Forsyth, and Marcus Kaiser, for their guidance and feedback. I also thank Roger Whittaker and Stuart Baker for providing me with their input during my yearly PhD progression reviews. I thank my examiners, Dr Victoria Morgan and Dr Rhys Thomas, for reviewing my PhD thesis.

I am thankful to the various people I have enjoyed working with at Computational Neurology, Neuroscience & Psychiatry Lab and Interdisciplinary Computing and Complex BioSystems research group. I especially thank my co-authors and colleagues: Joe Necus, Gabrielle Schroeder, Nádia Silva, Sriharsha Ramaraju, Paweł Widera, and Yiming Huang. Apart from having stimulating discussions with them as my fellow scientists, I cherish some of them as my close friends.

Finally, I would like to express my gratitude towards my parents, my wife Priyanka Sinha, and my family. No words can describe enough the enormous support I receive from them; thank you for everything.

Contributions

I acknowledge here the specific contributions made by people[1] involved in the projects undertaken during this thesis.

- Chapters 1 and 5 were written entirely by NS and updated with suggestions from PNT.
- Chapters 2 was drafted by NS and updated with suggestions from YW, NMS, AM, AWM, JT, SBV, GPW, JSD, PNT, and peer-reviewers assigned by the Neurology journal. All figures were produced by NS. All experiments were performed by NS. All codes were written by NS. Connectivity matrices and manual drawing of resection masks were initially done by PNT. Appendix Figure A.2 was produced by NMS. Raw data were collected and organised by AM, AWM, JT, SBV, GPW, JSD.
- Chapters 3 was drafted by NS and updated with suggestions from NP, GMS, JT, SBV, GPW, JSD, YW, PNT, and peer-reviewers assigned by the Epilepsia journal. All figures were produced by NS. All experiments were performed by NS. All codes were written by NS. All network data of patients and controls were generated by NS. Initial data exploration using network based statistics was done by NP, a master student supervised by NS. Raw data were collected and organised by JT, SBV, GPW, JSD.
- Chapters 4 was drafted by NS and updated with suggestions from YW, JD, MK, TT, RF, PNT, and peer-reviewers assigned by the NeuroImage:Clinical journal. All figures were produced by NS. All experiments and simulations were performed by NS. All codes were written by NS. Imaging data were preprocessed by NS. Initial dynamical model construction in equations 4.1-4.5, section 4.3.4 was performed by YW. Raw data were collected and organised by TT.

[1] NS: Nishant Sinha; PNT: Peter N Taylor; YW: Yujiang Wang; NMS: Nádia Moreira da Silva; AM: Anna Miserocchi; AWM: Andrew W McEvoy; JT: Jane de Tisi; SBV: Sjoerd B Vos; JSD: John S Duncan; GPW: Gavin P Winston; NP: Natalie Peternell; GMS: Gabrielle M Schroeder; JD: Justin Dauwels; TT: Thomas Thesen; MK: Marcus Kaiser; RF: Rob Forsyth

Declaration

I hereby declare that except where specific reference is made to the work of others, the contents of this dissertation are original and have not been submitted in whole or in part for consideration for any other degree or qualification in this, or any other university. This dissertation is my own work and contains nothing which is the outcome of work done in collaboration with others, except as specified in the text and Acknowledgements.

Nishant Sinha

July 2021

Publications

The following publications have been produced as part of the work undertaken during the writing of this thesis:

Nishant Sinha, Natalie Peternell, Gabrielle M. Schroeder, Jane de Tisi, Sjoerd B. Vos, Gavin P. Winston, John S. Duncan, Yujiang Wang, and Peter N. Taylor "Focal to bilateral tonic-clonic seizures are associated with widespread network abnormality in temporal lobe epilepsy." *Epilepsia* 2021; 62(3):729-741, doi:10.1111/epi.16819.

Nishant Sinha, Yujiang Wang, Nadia Silva, Anna Miserocchi, Andrew W. McEvoy, Jane de Tisi, Sjoerd B. Vos, Gavin P. Winston, John S. Duncan, and Peter N. Taylor. "Structural brain network abnormalities and the probability of seizure recurrence after epilepsy surgery." *Neurology* 2021; 96:1–14, doi:10.1212/WNL.0000000000011315.

Nishant Sinha, Yujiang Wang, Justin Dauwels, Marcus Kaiser, Thomas Thesen, Rob Forsyth, Peter N. Taylor. "Computer modelling of connectivity change suggests epileptogenesis mechanisms in idiopathic generalised epilepsy." *NeuroImage:Clinical*, 2019; 21:101655, doi:10.1016/j.nicl.2019.101655.

Peter N. Taylor, **Nishant Sinha**, Yujiang Wang, Sjoerd B. Vos, Jane de Tisi, Anna Miserocchi, Andrew W. McEvoy, Gavin P. Winston, John S. Duncan. "The impact of epilepsy surgery on the structural connectome and its relation to outcome." *NeuroImage:Clinical*, 2018; 18:202-214, doi:10.1016/j.nicl.2018.01.028.

Yujiang Wang, **Nishant Sinha**, Gabrielle M. Schroeder, Sriharsha Ramaraju, Andrew W. McEvoy, Anna Miserocchi, Jane de Tisi, Fahmida A. Chowdhury, Beate Diehl, John S. Duncan, Peter N. Taylor. "Interictal intracranial electroencephalography for predicting surgical success: The importance of space and time." *Epilepsia*, 2020; 61:1417-1426, doi:10.1111/epi.16580.

Joe Necus, **Nishant Sinha**, Fiona E Smith, Peter E Thelwall, Carly J Flowers, Peter N Taylor, Andrew M Blamire, David A Cousins, Yujiang Wang. "White matter microstructural properties in bipolar disorder in relationship to the spatial distribution of lithium in the brain." *Journal of Affective Disorders*, 2019; 253:224-231, doi:10.1016/j.jad.2019.04.075.

Sriharsha Ramaraju, Yujiang Wang, **Nishant Sinha**, Andrew W. McEvoy, Anna Miserocchi, Jane de Tisi, John S. Duncan, Fergus Rugg-Gunn, Peter N. Taylor. "Removal of Interictal MEG-Derived Network Hubs Is Associated With Postoperative Seizure Freedom." *Frontiers in Neurology*, 2020, 11:1099, doi:10.3389/fneur.2020.563847.

Joe Necus, Fiona E Smith, Peter E Thelwall, Carly J Flowers, **Nishant Sinha**, Peter N Taylor, Andrew M Blamire, Yujiang Wang, David A Cousins. "Quantification of brain proton longitudinal relaxation (T1) in lithium-treated and lithium-naive patients with bipolar disorder in comparison to healthy controls." *Bipolar Disorder*, 2019; 00:1-8, doi:10.1111/bdi.12878.

Yujiang Wang, Gabrielle Schroeder, **Nishant Sinha**, Peter N Taylor. "Personalised network modelling in epilepsy." *A Complex Systems Approach to Epilepsy: Concept, Practice, and Therapy* 2019 (in press), arXiv:1901.01024.

Table of contents

List of figures

List of tables

List of abbreviations

MRI	Magnetic Resonance Imaging
FLAIR	Fluid-Attenuated Inversion Recovery
sMRI	Structural Magnetic Resonance Imaging
dMRI	Diffusion Magnetic Resonance Imaging
fMRI	Functional Magnetic Resonance Imaging
EEG	Electroencephalography
iEEG	Intracranial Electroencephalography
ECOG	Electrocorticography
SEEG	Stereoelectroencephalography
MEG	Magnetoencephalography
PET	Positron Emission Tomography
SPECT	Single-Photon Emission Computed Tomography
TLE	Temporal Lobe Epilepsy
FBTCS	Focal to Bilateral Tonic-Clonic Seizures
GGE or IGE	Genetic Generalised Epilepsy or Idiopathic Generalised Espilepsy

ILAE International League Against Epilepsy

AED Anti Epileptic Drugs

SVM Support Vector Machine

ROC Receiver Operating Characteristic curve

AUC Area Under the ROC Curve

FA Fractional Anisotropy

MD Mean Diffusivity

DTI Diffusion Tensor Imaging

AAL Automated Anatomical Parcellation

DKT Desikan-Killiany Atlas

ROI Region of Interest

NBS Network Based Statistics

SUDEP Sudden Unexpected Death in Epilepsy

JME Juvenile Myoclonic Epilepsy

GTCS Generalise Tonic Clonic Seizure

CAE Childhood Absence Epilepsy

DMN Default Mode Network

PCC Posterior Cingulate Cortex

MPFC Medial Prefroontal Cortex

TBSS Tract-based Spatial Statistics

SWD Spike Wave Dynamics

Chapter 1

Introduction

1.1 Epilepsy

Epilepsy is a debilitating brain disorder in which patients have unprovoked recurrent seizures. There are approximately 60 million people worldwide with epilepsy, with an incidence rate of 61.44 per 100,000 person-years (Fiest et al., 2016). Seizures in epilepsy can be either focal or generalised. In focal seizures, the abnormal activity in the brain originates from a well localised focus. These seizures can either remain localised to a few brain areas—focal only—or they can spread bilaterally recruiting other brain areas—focal to bilateral tonic-clonic seizures. In generalised seizures, the seizure focus is unclear, and the abnormal brain activity, typically captured electrographically, are seen simultaneously across all recording channels (Fisher et al., 2017).

The primary line of treatment for controlling seizures is seizure suppressing medications[1]. With an appropriate regimen of up to three drugs, seizures remit in approximately 60-70% patients (Brodie et al., 2012). If the seizures do not remit, the chances of a patient becoming seizure-free, solely on pharmacotherapy, is unlikely (Brodie et al., 2012; Jobst and Cascino, 2015). These drug-resistant epilepsy patients can benefit significantly from more advanced therapies such as epilepsy surgery or brain stimulation (Sheikh et al., 2020). To determine the best treatment strategy, a neurologist should typically direct a drug-resistant epilepsy patient to a specialised epilepsy centre for advanced diagnosis.

[1] https://www.nice.org.uk/guidance/cg137

1.2 Brain imaging in epilepsy

Brain imaging is fundamental to the advanced diagnosis of epilepsy, especially when a patient is under consideration for neurosurgical treatments (Duncan et al., 2016). High-quality brain imaging can reveal atypical changes in the brain of epilepsy patients. The main objective of these diagnoses is to delineate brain areas that are causing seizures. The goal is to plan the best treatment pathway that controls seizures while minimising any neurological or cognitive deficits to a patient. Therefore, an epilepsy-specific image acquisition protocol and a multidisciplinary team are crucial to devising a potential treatment pathway (Bernasconi et al., 2019; Wellmer et al., 2013).

Current clinical diagnoses involve multiple imaging modalities for capturing different aspects of brain structure, function, and metabolism (Duncan et al., 2016). *Structural abnormalities*, such as a lesion, dysplasia, or sclerosis, are mapped from a combination of T1-weighted MRI, T2-weighted MRI, and FLAIR sequences. *Functional abnormalities*, such as interictal epileptiform discharges and seizure activities, are detected from EEG-based methods like long-term video-EEG telemetry, or invasive SEEG/ECoG recordings. *Metabolic abnormalities*, such as hypometabolism or hyperperfusion of an injected tracer, are mapped for locating the seizure focus using PET and SPECT imaging. Information from these imaging data is combined with demographic, historical, and semiological data of a patient to identify the epileptogenic tissue. These currently established clinical practices effectively remit chronic seizures in approximately half of all the drug-resistant epilepsy patients (Tisi et al., 2011).

The need to improve these established diagnosis protocols is well recognised; therefore, new modalities are increasingly being adopted (Zijlmans et al., 2019). Many specialised epilepsy centres often complement the EEG-based methods with fMRI and MEG imaging. fMRI and MEG are whole-brain non-invasive modalities that can provide a high spatial resolution to capture the functional changes (Englot et al., 2015, 2020). Another promising imaging modality which is beginning to emerge of a high clinical value is the diffusion-weighted MRI. Diffusion MRI is the only non-invasive imaging modality that can map the white-matter structure. Some specialised centres have incorporated diffusion MRI to guide surgery, specifically to avoid surgical damage to white matter connections during tumour resection and prevent postoperative neurological deficits after epilepsy surgery (Winston et al., 2014).

Each neuroimaging modality captures some aspect of brain spatial and temporal activity; when these individual aspects integrate, we can reconstruct and understand the underlying pathological phenomenon. Clinically, it is desirable to have a concordance between different modalities; discordant findings between imaging modalities suggest further investigation and careful consideration of the treatment pathway (Duncan et al., 2016; Zijlmans et al., 2019). Therefore, there is an ongoing paradigm shift towards multimodal integration of different imaging data, preferably in a common stereotactic space, for planning treatment and better estimating its risk-benefit ratio.

1.3 Treatment gaps and clinical needs

The current clinical practices for advanced diagnosis and treatment of epilepsy bring considerable improvement in seizure control, quality of life, and overall functioning in patients compared to those continuing on intensive pharmacotherapy (Sheikh et al., 2020). Despite the benefits, the risk of misdiagnosis and uncertainty about the patient's response to treatment—medication, surgery, or neurostimulation—are high (Jehi, 2020; Mithani et al., 2019; Vakharia et al., 2018). We highlight three critical treatment gaps and challenges encountered by the current neurological practice in delivering better care for epilepsy patients.

First, the heterogeneity between patients presents as a significant treatment challenge. Individual patients are heterogeneous in their history, demography, seizure semiology, and biology. Depending on the disease severity and progression, each patient needs a treatment tailored to them. There is a clinical need to quantify where a patient falls on the disease spectrum. Several studies have shown that we can address heterogeneity by applying quantitative neuroimaging methods and formal approaches to combine multivariate data, thus stratifying patient on the disease spectrum and minimising misdiagnosis (Marquand et al., 2016; Morgan et al., 2017; Taylor et al., 2018). While these methods can reconcile heterogeneity, it is also essential to strike the right balance in recruiting patients from a homogeneous disease cohort. Specifically, accounting for patient-specific heterogeneity in a homogenous cohort can be hugely beneficial in elucidating pathological disease-specific mechanisms.

Second, the exact mechanisms of epileptogenesis and ictogenesis are unclear. Mechanisms underlying epileptogenesis would inform about the development of epilepsy; thus enabling treatments to prevent epilepsy in those at risk. Mechanisms underlying ictogenesis would inform about the development of seizures; thus allowing seizure prediction and treatments for

suppressing its manifestation. A general understanding suggests that loss of balance between excitation and inhibition causes epilepsy (Scharfman, 2007). However, our current knowledge does not suffice to develop targeted treatments. Limited therapies exist for patients whose surgery on cortical tissues producing seizures is prohibitive due to neurological complications or due to age. There is a clinical need to understand the pathophysiology of epileptogenesis and ictogenesis to develop targeted interventions (Pitkänen and Engel, 2014; Pitkänen et al., 2016).

Third, after any intervention, neuroplasticity mechanisms reorganise the brain, thus increasing the uncertainties about a patient's response to treatment. For example, the chances of brain network reorganisation after therapy in paediatric patients is higher than adult patients. Predicting how a patient would respond to treatment and suggesting alternative treatment strategies can complement the clinical decision making about which treatment to choose, and which patient to follow-up more closely. Thus, there is a clinical need to identify the biomarkers of treatment response that can enable more accurate computation of a planned intervention's risk-benefit ratio (Bell et al., 2017; Jehi et al., 2015; Larivière et al., 2020a; Silva et al., 2020b).

The treatment gaps highlighted above represent the new frontiers of knowledge discovery for advancing medical practices in epilepsy. Indeed, other treatment gaps, for example, making epilepsy therapy accessible to every patient in need in a resource-constrained setting, is a significant challenge but those studies are beyond the scope of this thesis.

1.4 Epilepsy as a network disease

Network neuroscience has transformed our conceptualisation of the brain as a network. Brain networks that we discuss here are mainly of two types: structural network and functional network. Nodes and edges constitute a network; each node represents a brain region, and the edge represents the connectivity between brain regions. In a structural network, the connectivity characterises a physical/anatomical connection, e.g. white matter fasciculi. In a functional network, the connectivity represents a node's statistical activity over time. By conceptualising the brain as a network, we can study its topology quantitatively by applying graph theory to elucidate how different regions in the brain interact with each other (Bassett and Sporns, 2017; Deleo et al., 2018).

Several studies applied quantitative approaches on brain network of epilepsy patients showing that epilepsy is a disorder of abnormal brain network. For patients with intractable focal epilepsy, alterations to structural and functional connectivity predicted surgical outcome (Bonilha et al., 2015; Englot et al., 2015; Keller et al., 2016; Morgan et al., 2017). Similarly, for patients with generalised epilepsy, typically MRI negative, altered network topology in structural and functional brain network are widely reported (Hatton et al., 2020; Larivière et al., 2020b; Liao et al., 2013; Zhang et al., 2011). These advancements are fundamentally changing the concept of pre-surgical evaluation in epilepsy. The current clinical approach to identify a localised epileptogenic tissue is rapidly shifting towards identifying an epileptic network fused within the healthy brain tissue and network (Zijlmans et al., 2019). It is highly plausible that the seizure onset zone is a part of an extended epileptic network. Incomplete removal of this epileptic network might result in a secondary seizure onset zone formation leading to seizure recurrence (Englot et al., 2015; Keller et al., 2016; Morgan et al., 2017; Sinha et al., 2020). Conversely, manipulating this epileptic network at crucial nodes and edges, even distant from seizure focus, can potentially remit seizures. For example, neuromodulatory therapies such as deep brain stimulation of thalamic structures or vagus nerve stimulation do not mainly target the seizure onset zone; however, they can still control seizures by at least 50% in nearly three-fourth of patients (Englot et al., 2016; Li and Cook, 2018). Therefore, apart from detecting regional abnormalities from routine brain imaging modalities, quantifying *brain network abnormalities* is likely to be of significant complementary value in identifying epileptic networks (Bonilha et al., 2013, 2015).

Static network representations of the brain are useful, but not sufficient to explain the dynamic mechanisms of epilepsy completely (Jirsa et al., 2014; Smith and Schevon, 2016). Epilepsy is a dynamic disease; the time-dependent phenomena at different time-scales like neuronal firing (ms), sleep-wake cycles (hrs), affect seizure occurrences (Baud et al., 2018; Karoly et al., 2018; Kuhlmann et al., 2018). Computational models can provide deeper insights into various dynamical features of seizures (Lytton, 2008). In focal epilepsy, dynamic models described the seizure onset pattern based on the electrographic events of fast oscillations and high-amplitude spikes (Wang et al., 2017). In generalised epilepsy, dynamic modelling explained the underlying bifurcation mechanisms of spike-wave epileptic discharges (Taylor et al., 2013a). However, the challenge is to take into account the evolving dynamics of this disorder to develop effective treatment strategies.

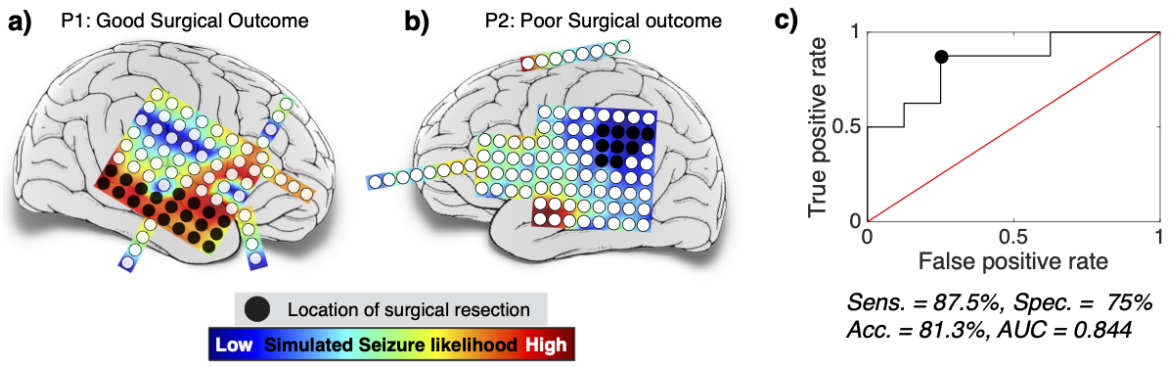

Fig. 1.1 **Virtual brain models can predict surgical outcomes.** Patient-specific functional network data from non-seizure segments of ECoG recordings combined with a bistable dynamical model quantified the seizure likelihood of underlying cortical tissues. Regions with high seizure likelihood overlapped with actual surgeries in 87.5% of patients with a good seizure outcome; panel **(a)** shows an example of a patient with a good surgical outcome. In 75% of patients where the model disagreed with the actual surgery, the patient had continued seizures after surgery; panel **(b)** shows an example of a patient with a poor surgical outcome. Panel **(c)** shows the overall discrimination between good and poor surgical outcomes with an AUC of 84.4% (Sinha et al., 2016).

A significant step towards exploring effective treatment strategies in epilepsy is possible by combining brain connectome with dynamical models (Jirsa et al., 2016; Proix et al., 2017). These connectome models are patient-specific virtual brains that can provide a test-bed for investigating the effect of planned treatment. We developed virtual brains from intracranial ECoG data to predict seizure outcomes after focal epilepsy surgery in our recent work, illustrated in Figure 1.1 (Sinha et al., 2016). We combined functional networks inferred from non-seizure segments of ECoG recordings with a bistable dynamical model to simulate seizures in the model. Through model simulations, we quantified the propensity of a brain region to have seizures. We then performed surgeries in the model by taking out network nodes and analysing if the model produced fewer seizures. By performing multiple virtual surgeries in the model, we could not only predict the outcomes of a planned resection, but we could also suggest alternative resection strategies to perturb the epileptic network. Many other studies have applied similar quantitative approaches to identify treatment targets and predict treatment outcomes in epilepsy (Goodfellow et al., 2016; Khambhati et al., 2016; Kini et al., 2019; Proix et al., 2017; Shah et al., 2019b). These studies reassure our understanding of epilepsy as a network disease and highlight the importance of developing rigorous, standardised, quantitative methods to map epileptic networks.

1.5 Summary and aims of this thesis

In this thesis, I studied epilepsy as a neurological disorder of abnormal brain network in which seizures originate, spread, and terminate via patient-specific spatial and temporal pathways. I believe that disrupting epileptic networks can enable effective seizure control; therefore, it is crucial to map and understand these epileptic networks. The primary underlying hypothesis of this thesis is that the brain network abnormalities could explain the variability in surgical outcomes and seizure spread across patients.

I retrospectively tested my hypothesis on patients with drug-resistant focal epilepsy who underwent temporal lobe surgery in Chapter 2. I mapped the whole-brain structural network of patients and the network disruption caused by epilepsy surgery. My main objective was to develop a quantitative measure of structural network abnormality and test if poor surgical outcomes associated with higher network abnormalities. I aimed to create a predictive model that would integrate routinely collected clinical data with the network abnormality metrics to stratify patients based on their likelihood to have a persistent seizure after surgery.

I next studied secondary generalisation of focal seizures in Chapter 3. Focal to bilateral tonic-clonic seizures signify the involvement of large brain areas and are associated with poor seizure outcomes after surgery. In this chapter, my objective was to test if seizures spreading to multiple brain areas are associated with higher and more widespread abnormalities. I aimed to develop rigorous statistical methods to map the aberrant subnetworks and highlight a patient's predisposition to secondary generalised seizures.

Finally, in Chapter 4 I studied patients with genetic generalised epilepsy (GGE) which are typically deemed radiologically negative. My objective was to assess if localised abnormalities are present in the white-matter fascicles in GGE. I applied quantitative neuroimaging technique to detect localised abnormalities in the white-matter structure of patients with mixed-syndrome GGE. I aimed to explain a potential mechanism of epileptogenesis in GGE using a thalamocortical computer model of spike-wave seizures.

Overall, the findings of this thesis emphasise the importance of quantitative neuroimaging methods to assess seizure spread and neurosurgical outcomes in epilepsy. My novel approach of combining the epileptic network and its disruption by epilepsy surgery shed new light on the pathophysiological mechanisms and paves the way towards individualised treatments.

Chapter 2

Structural network abnormalities and post-surgery seizure recurrence

The data in the following chapter is published in Neurology. Whilst minor adjustments to that article have been made in order to be consistent with this thesis format, the background, methods, results, and conclusions match those of the peer-reviewed article.

Nishant Sinha, Yujiang Wang, Nadia Silva, Anna Miserocchi, Andrew W. McEvoy, Jane de Tisi, Sjoerd B. Vos, Gavin P. Winston, John S. Duncan, and Peter N. Taylor. "Structural brain network abnormalities and the probability of seizure recurrence after epilepsy surgery." *Neurology* 2021; 96:1–14, doi:10.1212/WNL.0000000000011315.

2.1 Abstract

We assessed pre-operative structural brain networks and clinical characteristics of patients with drug resistant temporal lobe epilepsy (TLE) to identify correlates of post-surgical seizure recurrences.

We examined data from 51 TLE patients who underwent anterior temporal lobe resection (ATLR) and 29 healthy controls. For each patient, using the pre-operative structural, diffusion, and post-operative structural MRI, we generated two networks: 'pre-surgery' network and 'surgically-spared' network. Standardising these networks with respect to controls, we determined the number of abnormal nodes before surgery and expected to be spared by surgery. We incorporated these 2 abnormality measures and 13 commonly acquired clinical data from each patient in a robust machine learning framework to estimate patient-specific chances of seizures persisting after surgery.

Patients with more abnormal nodes had lower chance of complete seizure freedom at 1 year and even if seizure-free at 1 year, were more likely to relapse within five years. The number of abnormal nodes was greater and their locations more widespread in the surgically-spared networks of poor outcome patients than in good outcome patients. We achieved 0.84 ± 0.06 AUC and 0.89 ± 0.09 specificity in predicting unsuccessful seizure outcomes (ILAE 3-5) as opposed to complete seizure freedom (ILAE 1) at 1 year. Moreover, the model-predicted likelihood of seizure relapse was significantly correlated with the grade of surgical outcome at year-one and associated with relapses up-to five years post-surgery.

Node abnormality offers a personalised non-invasive marker, that can be combined with clinical data, to better estimate the chances of seizure freedom at 1 year, and subsequent relapse up to 5 years after ATLR.

2.2 Introduction

Epilepsy surgery is an effective treatment for bringing seizure remission in drug-resistant focal epilepsies, however, it is underutilised (Langfitt and Wiebe, 2008; Vakharia et al., 2018; Wiebe et al., 2001). One reason for the under-referral of patients is the reservations regarding the uncertainty of its outcome (Haneef et al., 2010; Vakharia et al., 2018). In around 30-40% of individuals, seizures continue despite surgery and the multidisciplinary team are unable

to accurately predict this risk (Bell et al., 2017; Janszky et al., 2004; Spencer and Huh, 2008; Tisi et al., 2011; Téllez-Zenteno and Wiebe, 2008). Therefore, to better inform this clinical decision making, there is a need to predict seizure outcomes both in the short-term, and the likelihood of seizure relapse in the long-term (Cohen-Gadol et al., 2006; Tisi et al., 2011).

The incomplete removal of a wider epileptogenic network is increasingly being recognised as one of the reasons for continued seizures post-surgery (Richardson, 2012; Spencer, 2002). Many studies, driven by the aforementioned hypothesis, have attempted predicting seizure outcomes from pre-surgical data (Bell et al., 2017; Bonilha and Keller, 2015; Gleichgerrcht et al., 2018; Goodfellow et al., 2016; Keller et al., 2016; Morgan et al., 2017; Munsell et al., 2015; Proix et al., 2017; Sinha et al., 2016). Most studies, however, have investigated brain networks without incorporating the knowledge of the planned/performed surgery into the analysis. Naturally, the outcome of epilepsy surgery will depend not only on the pre-surgery brain network, but also on how the surgery (i.e., its location and extent) will affect the brain network (Taylor et al., 2018). Including surgical data allows the inference of a 'surgically-spared' network – the subnetwork for which none of the connections are altered by surgery and are therefore expected to remain after the surgery. Thus, the presence of epileptogenic structures in the surgically-spared network, a likely cause for seizure recurrence, needs investigation.

Studies employing quantitative imaging have consistently demonstrated that in TLE there are structural abnormalities that involve brain structures beyond the hippocampus and the temporal lobe (Bernasconi et al., 2003; Concha et al., 2012; Deleo et al., 2018; Keller and Roberts, 2007; McDonald et al., 2008; Otte et al., 2012). Accumulating evidence suggests that these abnormalities configure a network of abnormal structures that may be involved in generation of seizures (Bernhardt et al., 2015; Bonilha et al., 2013; Bonilha and Keller, 2015; Duncan et al., 2016; Zijlmans et al., 2019). Indeed, the pathophysiological mechanisms associated with epileptogenesis have a strong basis in aberrant neural connectivity (Besson et al., 2017; Sinha et al., 2019). Therefore, quantifying the abnormalities before, and expected to remain after, surgery may inform postoperative seizure outcome.

The main goal of our study was to understand how structural network abnormalities relate to seizure outcomes after temporal lobe epilepsy surgery. We investigated the abnormality of the 'surgically-spared' networks because, at a conceptual level, post-operative outcomes

will likely be determined by what remains post-surgery. Our study addresses three main questions: a) do patients with more abnormalities in the surgically-spared network have worse postoperative seizure outcomes? b) does surgery reduce node (region) abnormality more in seizure-free patients than in not seizure-free patients? c) if the node abnormality measure is to be used alongside common clinical variables of a patient, would it generalise to make patient-specific predictions on the chances of seizure freedom after surgery? Our study shows that the node abnormality in the surgically-spared network is an important measure to be considered alongside other pre-surgical clinical factors to evaluate the risk of poorer seizure outcomes in patients with refractory TLE.

2.3 Methods

2.3.1 Participants

We studied 51 patients who underwent unilateral anterior temporal lobe resection at National Hospital of Neurology and Neurosurgery, London, United Kingdom. Patients were followed up after surgery and classified according to the ILAE scale of seizure outcome at 12-month intervals (Wieser et al., 2008). One year after the surgery, 34 patients were completely seizure-free (ILAE 1), 8 patients continued to have auras only (ILAE 2), and 9 patients were not seizure-free (ILAE 3-5). No patient had an outcome of ILAE 6.

ILAE surgical outcomes of seizure freedom were recorded annually at years 1 and 2 for all 51 patients, at year 3 for 45 patients, year 4 for 37 patients, and at year 5 for 31 patients. We considered that a patient had a seizure relapse if, at any given year after year 1, the ILAE outcome of the patient changed from ILAE 1-2 to ILAE 3-5. If the ILAE outcome of a patient did not change to ILAE 3-5 and the follow-up duration was less than five years, it cannot be ascertained if the patient would have relapsed upon a full five-year follow-up. Therefore, beyond the known follow-up period, we did not include such patients in our analysis. Based on this criterion, amongst the year 1 ILAE 1-2 patients, the number of patients that relapsed (did not relapse) by the end of each subsequent years were: 3(39) by year 2; 8(29) by year 3; 11(21) by year 4; 13(14) by year 5.

Notably, seizure outcome and seizure relapse are two different measures. Seizure outcome at year 1 categorised all 51 patients based on their ILAE score at one year after surgery. Seizure relapse categorised only those patients who were initially free from disabling seizures i.e.,

ILAE 1 or 2 but then later in 5 years had a seizure reoccurrence. In labelling seizure relapse, we excluded the 9 patients who had seizure recurrence within one year after the surgery (i.e., ILAE 3-5 at year 1) to avoid any bias. The full patient details are provided online in Table S1 at https://doi.org/10.5061/dryad.vx0k6djnv and summarised in this thesis in Table 2.1.

Table 2.1 Demographic and clinical data of patients

Year 1 outcome[*]	*ILAE 1*	*ILAE 2*	*ILAE 3-5*	*Statistics*
Number of patients, n	34	8	9	
Sex (male/female)	16/18	2/6	2/7	not significant
Age at onset (yrs, $\mu \pm \sigma$)	**12.2 ± 10.3**	14.2 ± 11.4	**19 ± 12**	p=0.04;d=0.64
Age at surgery (yrs, $\mu \pm \sigma$)	38 ± 11.9	38.6 ± 10.3	46.5 ± 10.2	not significant
Epilepsy duration (yrs, $\mu \pm \sigma$)	25.8 ± 15.8	24.3 ± 17.3	27.5 ± 7.3	not significant
Side (left/right)	22/12	3/5	5/4	not significant
Hippocampal sclerosis[+]*, n(%)*	24 (70.5%)	6 (75%)	5 (55.5%)	not significant
Number of AEDs (n, $\mu \pm \sigma$)	**6.3 ± 2.4**	7.6 ± 2.9	**9.2 ± 3.3**	p=0.01;d=1.14
Preop MRI (nor./abr.)[++]	5/29	1/7	2/7	not significant
Status epilepticus, n(%)	5 (15.7%)	0 (0%)	3 (33.3%)	not significant
History of FBTCS , n(%)	28 (82.3%)	6 (75%)	6 (66.7%)	not significant
Depression, n	8	5	2	not significant
Psychosis, n	2	0	0	not significant
Psychiatric disorders, n	8	3	4	not significant
[**]*Relapsed by year 2, n(%)*	0 (0%)	3 (37.5%)	9 (100%)	
Relapsed by year 3, n(%)	3 (8.8%)	5 (62.5%)	9 (100%)	
Relapsed by year 4, n(%)	5 (14.7%)	6 (75%)	9 (100%)	
Relapsed by year 5, n(%)	7 (20.6%)	6 (75%)	9 (100%)	

Abbreviations: μ mean; σ standard deviation; *n* number of patients; AEDs anti-epileptic drugs; yrs years

[*]*Seizure outcome* refers to the post-operative seizure outcome, measured on the ILAE scale after surgery at year 1. ILAE 1 for complete seizure freedom at one year after surgery is labelled as good outcome. ILAE 3-5 for continued seizure at one year after surgery is labelled as poor outcome. ILAE 2 for no disabling seizures, only auras, at one-year after surgery is categorised as a separate group between the spectrum of good and poor outcome.

[**]*Seizure relapse* is a binary measure to indicate if patients had a recurrence of seizures at any time up-to five years after remaining seizure-free for at least one-year post surgery i.e., if patients with ILAE 1-2 at year one changed to ILAE 3-5 during the five-year follow-up.

[+]*Hippocampal sclerosis* from MRI was determined by segmentation of hippocampus using anatomical landmarks as described elsewhere (Winston et al., 2013a).

[++]*Preoperative MRI* was deemed abnormal radiologically in presence of hippocampal sclerosis, cavernoma, lesion, cortical dysplasia, or dysembryoplastic neuroepithelial tumors, whereas deemed radiologically normal for MRI negative patients.

We also studied 29 healthy individuals, age and sex matched to patient group, with no significant medical history of neurological or psychiatric problems. The study was approved by the National Hospital for Neurology and Neurosurgery and the Institute of Neurology Joint Research Ethics Committee, and written informed consent was obtained from all subjects. Data were analysed in this study under the approval of the Newcastle University Ethics Committee (reference number 1804/2020).

2.3.2 MRI acquisition, data processing, and surgery network

For each participant, T1-weighted structural (sMRI) and diffusion-weighted (dMRI) data were acquired before surgery. Within one year of surgery, T1-weighted sMRI data was acquired again for patients. As in our previous study (Taylor et al., 2018), we used the postoperative sMRI to manually draw the resection mask in preoperative sMRI space, hence, delineating the resected tissue. We parcellated preoperative T1 image in 114 cortical and subcortical regions of interest (ROIs) derived from the predefined Geodesic Information Flow atlas and separately in 82 ROIs using the Freesurfer Desikan-Killiany atlas in the native space of each participant. Along with streamlines inferred using dMRI tractography, and regions inferred using parcellation, we incorporated the information of resected tissue to infer two networks: pre-surgery network and surgically-spared network. The pre-surgery streamline network is the whole-brain network depicting the number of streamlines connecting predefined parcellated ROIs. The surgically-spared network is a subnetwork of the pre-surgery network which is inferred after removing the streamlines that intersected the resection mask. By definition, surgery can only cause an immediate reduction in the number of streamlines. Therefore, we specified that the surgically-spared network contains only those network edges which are not expected to change in streamline count following surgery (i.e., edges where their streamlines do not pass through/into the resection cavity). The overall concepts are illustrated in Figure 2.1. Detailed imaging protocols and data processing pipeline to infer these networks are described fully in Appendix A.1.

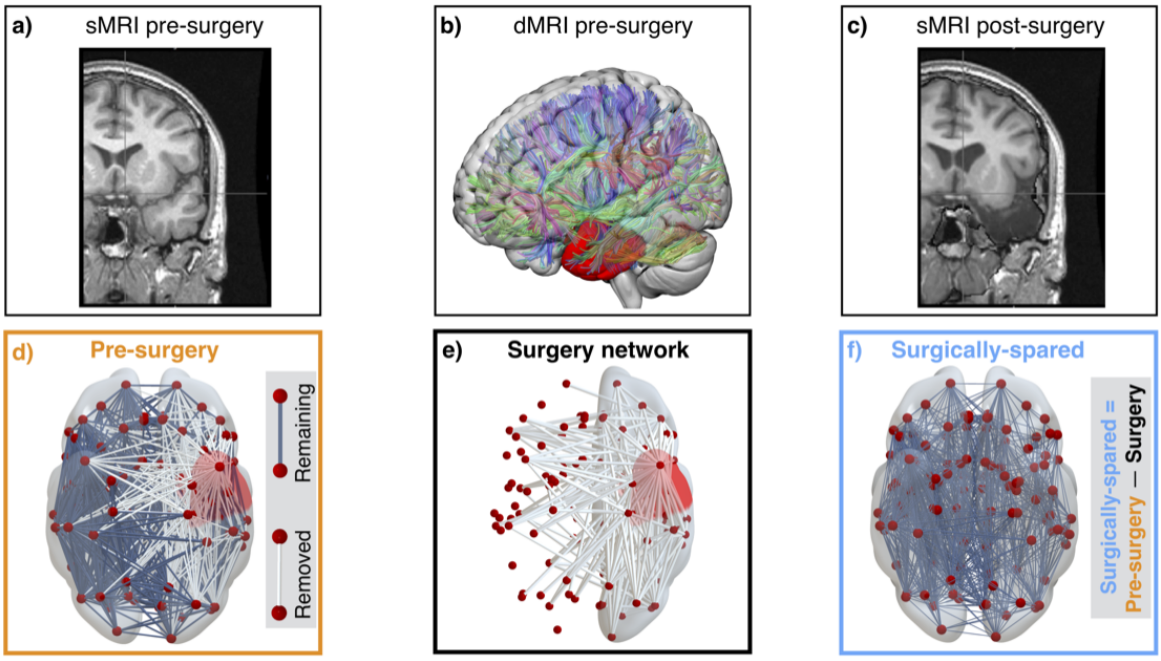

Fig. 2.1 **Estimating patient-specific surgery network.** Preoperative T1 weighted MRI of an example patient in panel **a)** and postoperative T1 weighted MRI in panel **c)** were used to delineate the tissue resected by surgery. The resected tissue shown by the red resection mask in panel **b)** was used with the preoperative diffusion MRI to infer brain networks. Pre-surgery network inferred based on the number of streamlines connecting different ROIs in panel **d)** ignores the surgery information by not taking the resection mask into consideration. The patient-specific surgery network is illustrated in panel e) which shows the connections that were affected by the surgery. Panel **f)** shows the surgically-spared network.

2.3.3 Node abnormality computation

We computed node abnormality on networks based on the mean generalised fractional anisotropy (gFA) property of dMRI streamlines (Tuch, 2004). The pre-surgery networks were standardised patient-specifically against controls as follows: for each connection present between ROIs i and j in a patient, the connection distribution was obtained from the equivalent connection between ROIs i and j from the control networks. The z-score for that connection was calculated as the number of standard deviations away from the mean, where the standard deviation and mean were obtained from the control distribution. Networks inferred from deterministic tractography are sparse, so we z-scored only those connections in patients for which an equivalent connection existed in at least 10 ($\approx$ 35%) controls (Reus and Heuvel, 2013). This is depicted in Figure 2.2a.

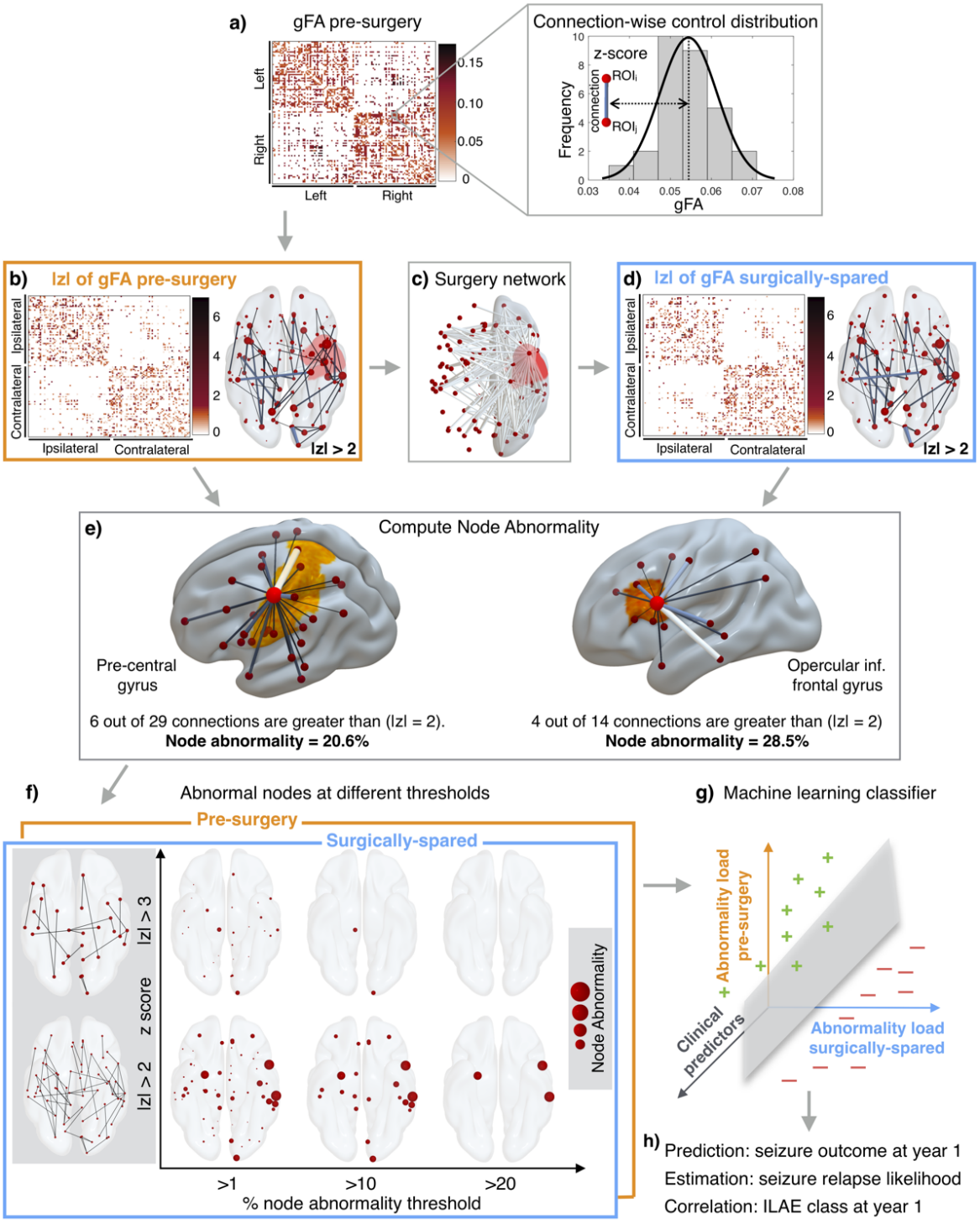

Fig. 2.2 **Overall pipeline.** Pre-surgical gFA network architecture for each patient in panel **a)** is inferred and connections between ROIs are standardised against a control distribution (illustrated for an example connection in the right of panel **(a)**) to obtain a z-score transformed network in panel **b)**. (continued...)

Fig. 2.2 (...continued) The connections affected by the surgery shown in surgery network in panel **c)** are removed to obtain surgically-spared network in panel **d)**. Panel **e)** shows the concept of node abnormality for two example nodes. By normalising the number of abnormal links to a node with its degree, the heterogeneity in the degree of network nodes is accounted for. A high degree node can be less abnormal compared to a low degree node depending on the number of abnormal connections. **f)** Different thresholds required for the computation of node abnormality are shown for surgically-spared network (blue panel front) and the pre-surgery network (orange panel back). z-score at which a link is considered abnormal is on the y-axis and the cut-off at which a node is considered abnormal is shown on the x-axis. **g-h)** Abnormality load in pre-surgery and surgically-spared networks are incorporated in a machine learning classifier along with the clinical predictors to predict seizure outcomes at year 1 both in terms of binary seizure-free (plus in green) vs. not seizure-free (minus in red) outcome as well as in terms of the probability with which each patient was classified as not seizure-free. These probabilities correlated with severity of seizure outcome (i.e. ILAE class) at year-one and associated with the seizure relapse in 5 years. We termed these probabilities as predicted seizure relapse likelihood.

After obtaining the pre-surgery z-scored gFA network, we removed the connections present in the surgery-affected network to obtain the surgically-spared z-transformed gFA network. High |z| indicates high deviation from normality. Thus, the pre-surgery network maps the abnormal links present before the surgery and surgically-spared network maps the abnormal links that would remain unaffected immediately after the surgery. This is illustrated in Figure 2.2b-d.

To study how different regions (nodes) are affected in these networks, we computed node abnormalities (Figure 2.2e) in the pre-surgery and surgically-spared networks by counting the number of abnormal links to each node. We normalised the number of abnormal links to a node by its degree in the pre-surgical network, thus expressing node abnormality in percentage terms.

Quantification of node abnormality load raises two questions: first, what is the definition of an abnormal connection? second, when is a node considered abnormal? The former is essential for the application of a threshold on the abnormality network to count the number of abnormal links at each node. For the latter, another threshold is needed to define beyond what percentage level a node should be considered abnormal. We therefore varied the z-score threshold from 2.1 to 4.5 in increments of 0.1 and the percentage abnormality threshold from 1% to 50% in increments of 1%. At each point on this two-dimensional grid, we computed how many nodes were abnormal in pre-surgery and surgically-spared networks. We term this

the "abnormality load"–the total number of abnormal nodes identified at any given pair of thresholds. This is illustrated in Figure 2.2f for six example threshold pairs. Finally, having quantified the abnormality load for each patient, we assessed its discriminatory ability in predicting seizure outcome at year 1 and seizure relapse in 5 years.

2.3.4 Quantifying the change in abnormality load after ATLR

To investigate the effect of surgical treatment on reduction of abnormalities, we compared the difference in abnormality load between pre-surgery and surgically-spared networks. The ROIs in the left and right hemispheres of patients were expressed as ipsilateral or contralateral to surgery. Then, we categorised each ROI into 6 ipsilateral and 6 contralateral areas i.e., temporal, subcortical, parietal, occipital, frontal, and cingulate cortices. In each area, we determined the number of abnormal nodes in the pre-surgery and surgically-spared networks patient-specifically. Then, we averaged the number of abnormal nodes in each area for seizure-free (ILAE 1) and not seizure-free (ILAE 3-5) groups of patients. Finally, by computing the proportion of abnormal nodes in every area (i.e., ratio of mean abnormal ROIs to the total number of ROIs in each area) for the pre-surgery and surgically-spared network, we noted the change due to the surgery in all patients.

2.3.5 Predictive model design for generalisability assessment

To predict the patient-specific probability of seizure relapse based on preoperative clinical data (in Table 2.1), pre-surgical, and surgically-spared node abnormality, we applied support vector machine (SVM) learning algorithm (Guyon et al., 2002; Platt, 1999). The outcome values for SVMs were the seizure outcome at year 1; ILAE 1 labelled as seizure-free outcome and ILAE 3-5 labelled as not seizure-free outcome. We incorporated a linear kernel in SVM because this enabled a direct interpretation of weights as relative feature importance. We performed nested-cross-validation in which the data was split into three folds: training, validation, and testing. During training, SVM learned from the data in the training fold only; it did not see any data in validation or test fold. Node abnormality measures were computed afresh for each patient in the training fold and the most discriminatory (highest AUC) threshold pairs across patients in the training fold were noted. A trained SVM learned to weigh the 15 preoperative attributes in the order of their relative importance to maximise the training accuracy. We avoided overfitting, by incorporating a regularisation parameter in

SVM. The regularisation parameter was optimised on the validation fold, after which the SVM was tested for generalisability on the unseen data in the test fold. This is akin to a new incoming patient (pseudo-prospective), whereby the learning algorithm has been trained and optimised on existing/past patient records.

During the training phase the SVM draws a linear hyperplane to separate patients who were seizure-free (ILAE 1) from those who were not seizure-free (ILAE 3-5) at year 1. The features of the test patient are then tested on this hyperplane and depending on how confidently the SVM places this patient in the not seizure-free group, a probability is assigned. We refer to these probabilities as the likelihood of seizure relapse because a high probability indicates a predicted propensity towards a not seizure-free outcome. By implementing leave-one-out scheme, we measured a) the net generalisability of the learning algorithm (quantified by AUC, accuracy, sensitivity, and specificity), b) how correlated are the predicted probabilities of seizure relapse with severity of seizure outcomes (i.e., ILAE class at 1-year), and c) the association between actual relapse in 5 years and the predicted probabilities of seizure relapse.

Ranking features indicated metrics that were important for prediction performance as opposed to those that may be confounding. Therefore, to identify the combination of most informative features, we removed the least informative feature and repeated the above process until a single feature remained (Fagerholm et al., 2015; Guyon et al., 2002). More details on data splits and nested-cross-validation are provided in Appendix A.2.

2.3.6 Statistical analysis

To investigate if a greater number of abnormal nodes are associated with not seizure-free (ILAE 3-5) outcomes, we applied non-parametric Wilcoxon rank-sum test. One-tailed p value was computed using ranksum function in MATLAB incorporating the exact method. Results are declared significant for $p<0.05$. We further applied Benjamini-Hochberg false discovery rate correction (Benjamini and Hochberg, 1995) at a significance level of 5%. Effect size between groups was computed using Cohen's d score, and the correlation coefficients between likelihood of seizure relapse and the severity of seizure outcome were determined using Spearman's rank-order. We computed 95% bootstrap confidence intervals of effect size, AUC, and median using a bias-corrected and accelerated percentile method from 10000 bootstrap resamples with replacement.

2.3.7 Data availability

To enable reproducibility, we have made available all the anonymised pre-surgery and surgically-spared brain networks of 51 patients, networks of 29 controls, codes for node abnormality computations, and all the trained machine learning models on the data presented at https://doi.org/10.5061/dryad.vx0k6djnv (in press).

2.4 Results

The results are organised in three parts. First, we assessed if patients with greater number of abnormal nodes (i.e., a higher abnormality load) are predisposed to ILAE 3-5 (poorer) seizure outcome after surgery. Outcomes are initially measured at 12 months and then at later years. Second, we investigated the effect of surgery in reducing the node abnormality load between the seizure-free and not seizure-free groups. Third, we determined the generalisability of node abnormality measure, if it is to be incorporated in a clinical setting alongside other clinical attributes, to estimate the chances of seizure recurrence for new patients.

2.4.1 Abnormality load corresponds with year 1 surgical outcome and later year seizure relapse

We investigated the abnormality load in surgically-spared and pre-surgical networks. Figure 2.3(a-d) illustrates abnormal nodes in the surgically-spared networks for four patients. The patients in panels (a) and (b) were seizure-free (ILAE 1) and having auras (ILAE 2) respectively at one-year after surgery and did not relapse subsequently; they had a relatively low node abnormality load. The patient in panel (c) initially had auras only (ILAE 2) at one-year post-surgery but later relapsed; this patient showed a higher abnormality load. The patient in panel (d), with the highest abnormality load, had the worst surgical outcome of ILAE 5 at one year, which persisted upon follow-up. In these four cases a greater abnormality load was associated with worse outcomes at year 1, and seizure relapse at later years.

Figure 2.3(e) shows the node abnormality load in surgically-spared network for the entire patient cohort. Patients who were not seizure-free (ILAE 3+) at one-year post surgery, had a significantly higher abnormality load than patients who were seizure-free ($p = 0.005, d =$ 1.11 [95%CI 0.42, 2.2] between ILAE 1 and ILAE 3-5 and $p = 0.01, d = 0.61$ [95%CI -0.92, 2.05] between ILAE 2 and ILAE 3-5). Here, we chose to analyse ILAE 2 as a separate group because clinical data (Table 2.1, S1) suggests that these patients, albeit free from disabling seizures at year-one, have a greater propensity to relapse in later years (Fairclough et al., 2017). Studying only the subset of patients who were initially seizure-free (i.e. ILAE 1, 2) at 1 year (Figure 2.3f-g), patients who relapsed had a higher abnormality load than the patients who did not relapse ($p = 0.04; d = 0.77$ [95%CI -0.01, 1.31]).

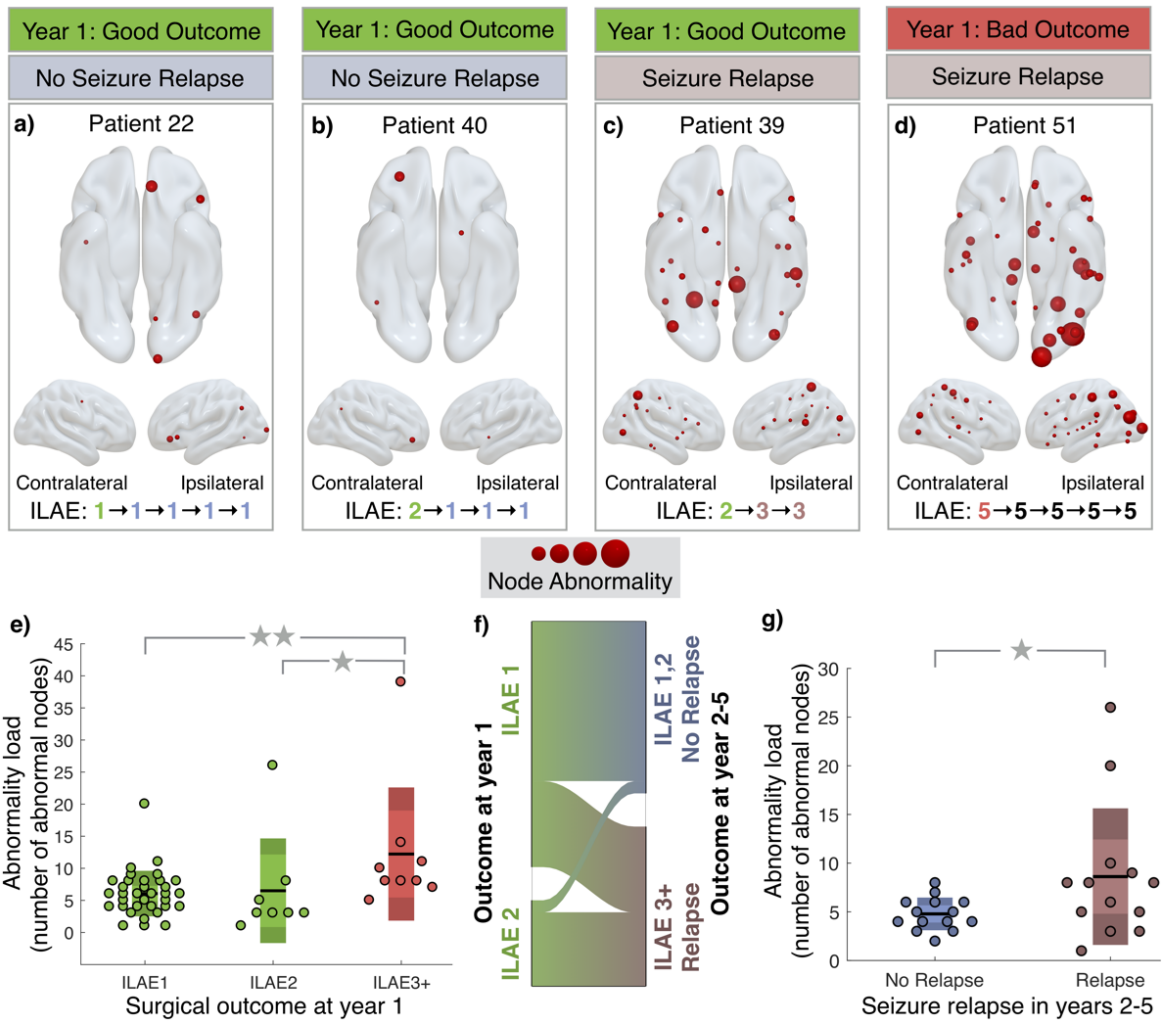

Fig. 2.3 **Association between the number of abnormal nodes in surgically-spared network with year-one surgical outcome and relapse. a-d)** Four patients are shown with their year-one surgical outcome and relapse information. Panel **a)** and **b)** show lower abnormality load in patients with ILAE 1 and ILAE 2 outcomes respectively with no relapse. Panel **c)** shows a patient with many abnormal nodes remaining yet having an ILAE 2 outcome at year-one but relapsing subsequently. Panel **d)** shows a large number of abnormal nodes remaining in a patient who was never seizure-free in five years. **e)** Significantly more abnormal nodes remained in ILAE 3+ patients compared to ILAE 1 and ILAE 2. *Statistical estimates:* ILAE1 ($n = 34$) median 6 [95%CI 5, 7.5]; ILAE2 ($n = 8$) median 3 [95%CI 2, 5.5]; ILAE3+ median 8 [95%CI 5, 10]; p(ILAE1 vs ILAE3+) = 0.005; d(ILAE1 vs ILAE3+) = 1.11 [95%CI 0.42, 2.2]; p(ILAE2 vs ILAE3+) = 0.01; d(ILAE2 vs ILAE3+) = 0.61 [95%CI -0.92, 2.04]. **f)** Alluvial flow diagram showing proportion of relapsed patients with ILAE 1 or ILAE 2 at year-one. **g)** In ILAE 1-2 patients, those who relapsed had significantly more abnormal nodes in the surgically-spared network. Statistical estimates: no relapse ($n = 14$) median 4.5 [95%CI 4, 6]; relapse ($n = 13$) median 8 [95%CI 5, 15]; $p = 0.04$; $d = 0.77$ [95%CI -0.01, 1.31]).

Node abnormality in Figure 2.3, computed from the surgically-spared network, was defined as the nodes with at least 10% of abnormal (z>2.8) connections. At this choice of thresholds, the discrimination (AUC) between the seizure-free and not seizure-free group was the highest. Comparable results are found for other threshold values (Appendix A.4), and with an alternative network parcellation (Appendix A.7). Thus, the discriminatory ability of the node abnormality load measure is consistent across the choice of threshold or the choice of parcellation scheme.

We found similar results in the pre-surgery networks. ILAE 3-5 patients had significantly more abnormal nodes than ILAE 1 patients. However, the size of this effect was less pronounced than in the surgically-spared networks, with relatively poorer discriminatory ability ($p = 0.03; d = 0.78$ [95%CI 0.04, 2.1]) (see, Appendix A.4, A.5). Therefore, our findings suggest that the surgically-spared network, which is the surgically informed subnetwork of the pre-surgery network, is more discriminatory in identifying seizure-free from not seizure-free patients.

2.4.2 Surgery-related effect on reducing abnormality load

How much effect does surgery have on reducing the abnormality load? We investigated the differences between the surgically-spared, and pre-surgery networks in terms of their abnormality load, and whether the projected change in abnormality load due to surgery was greater and more widespread in one outcome group compared to another. The proportion of abnormal nodes in different brain areas for ILAE 1 (seizure-free) and ILAE 3-6 (not seizure-free) groups are shown in Figure 2.4, with the intermediate ILAE 2 patients shown in Appendix A.8.

In terms of the spatial extent of surgery, the expected reduction in the proportion of abnormal nodes was more widespread in the seizure-free group than in the not seizure-free group. The ILAE 1 group had a significant drop in the proportion of abnormal nodes in the surgically-spared network, compared to the pre-surgical network, in four ipsilateral areas: temporal, subcortical, occipital, and frontal (Figure 2.4a-b). In ILAE 3-5 group, however, the drop in the proportion of abnormal nodes was not significant in any of the ipsilateral or contralateral areas (Figure 2.4c-d). Similar surgery related effect was found for node abnormality computed at different threshold values Appendix A.6.

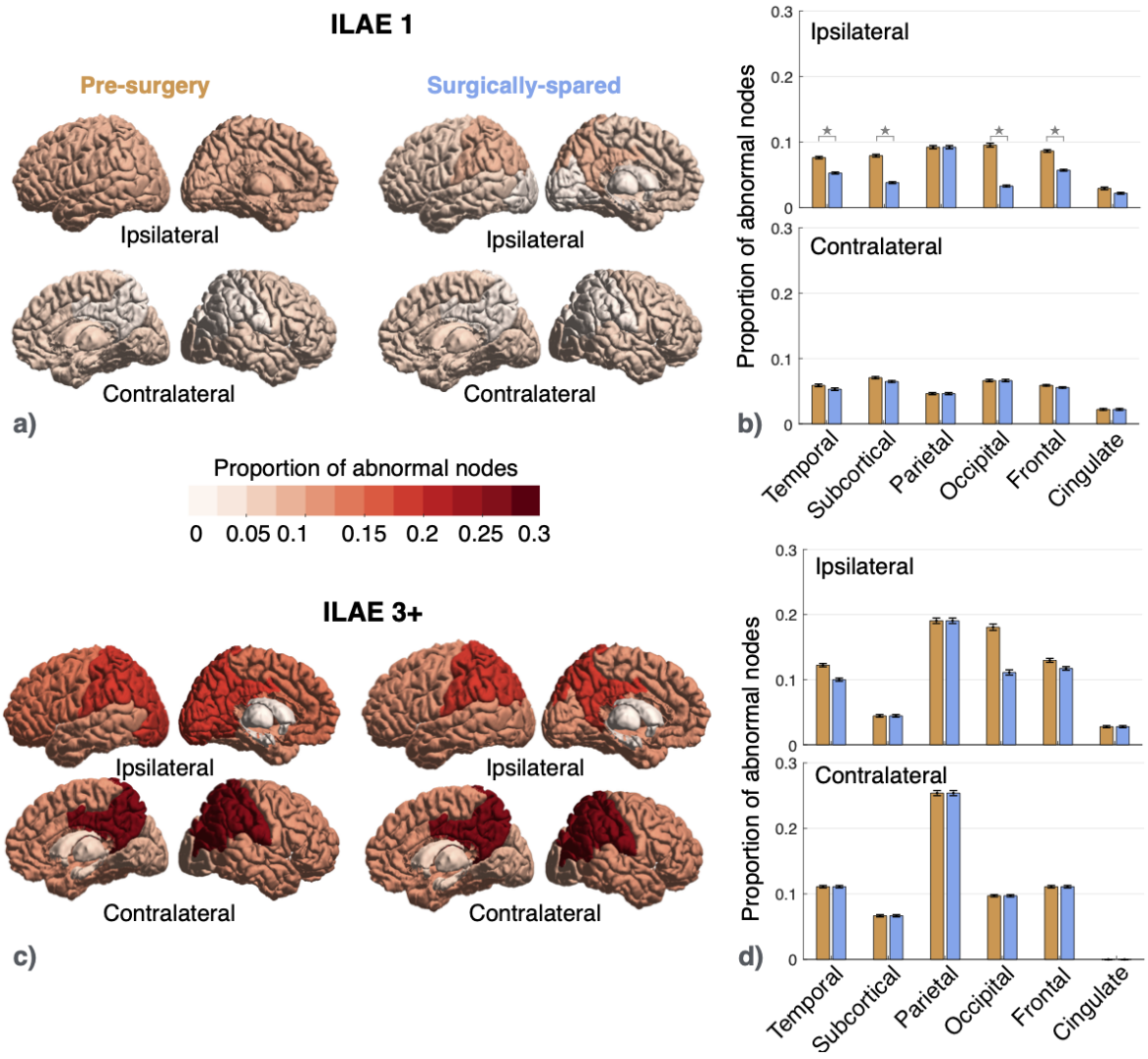

Fig. 2.4 **Effect of surgery in reducing node abnormality is more widespread in the seizure-free group at year-one. a)** Proportion of abnormal nodes computed for pre-surgery and surgically-spared networks are colour coded for six ipsilateral and contralateral brain areas in the seizure-free (ILAE 1) group. **b)** Bar plot shows the drop in the proportion of abnormal nodes in surgically-spared network compared to pre-surgery network. Error bars represent the standard error of the proportion of abnormal nodes in each area. Significant reductions in ipsilateral temporal ($t = 3.19$, mean 0.02 [95%CI 0.01, 0.04], $p = 0.003$), ipsilateral subcortical ($t = 4.31$, mean 0.04 [95%CI 0.02, 0.06], $p < 0.001$), ipsilateral occipital ($t = 2.94$, mean 0.06 [95%CI 0.02, 0.11], $p = 0.006$), and ipsilateral frontal ($t = 3.21$, mean 0.03 [95%CI 0.01, 0.05], $p = 0.002$) areas are indicated in stars. **c)** Different brain areas in pre-surgery and surgically-spared network are colour coded based on the proportion of abnormal nodes in the not seizure-free group (ILAE 3+) **d)** Corresponding bar plot shows the drop in the proportion of abnormal nodes in surgically-spared network compared to pre-surgery network. None of the ipsilateral or contralateral areas showed a significant reduction in the proportion of abnormal nodes.

In terms of reduction in the amount of abnormality load, ILAE 1 patients had larger proportional reductions than ILAE 3-5 patients ($p = 0.01; d = 0.81$ [95%CI 0.2, 1.4]), however, their absolute reduction did not differ significantly ($p = 0.14; d = 0.42$ [95%CI -0.25, 0.84], see Appendix A.8). Thus, we suggest that the temporal lobe epilepsy surgery causes a greater and widespread reduction in abnormality load in the seizure-free group than in the not seizure-free group.

2.4.3 Personalised prediction of 12-month seizure freedom additionally suggests ILAE class and relapse at later years

We assessed the generalisability of the abnormality measure when used alongside other clinical attributes to predict patient-specific chances of poorer outcomes. Implementing nested-cross validation, we built machine learning models which classified new unseen (test) patients as either belonging to ILAE 1 or ILAE 3-5 group at 12 months. Our rationale for omitting ILAE 2 patients from the training phase of the model was that since they have a propensity to develop such seizures in the later years, they therefore lie on a spectrum in between the seizure-free and the not seizure-free group. The model also scored each patient with a probability of belonging to either of the classes. Notably, the models were blind to three aspects of the data (a) all ILAE 2 patients, (b) ILAE classification 3, 4, 5 (the model simply sees these as 'poor outcome'), and (c) outcomes at later years.

We incorporated up to 15 features in the model: 13 clinical attributes, pre-surgical abnormality load, and surgically-spared abnormality load. These features describe the presurgical attributes of patients and we evaluated them based on their combined ability in accurately predicting surgical outcomes at one-year. However, some features may be less informative than others in predicting surgical outcomes; including less informative features causes a drop in the prediction performance. Therefore, by implementing stepwise removal of less informative features, we obtained combinations of preoperative features that identified patients with poor seizure outcome at one-year after surgery in 100% cases (i.e., specificity). The area under the ROC curve (AUC) at every step of feature elimination is plotted in Figure 2.5(a) and magnified at one example point (marked with a star) in Figure 2.5(b) with the corresponding confusion matrix shown in the inset. Average prediction performance across all stepwise feature removals was robust at: AUC$= 0.84 \pm 0.07$, accuracy$= 0.79 \pm 0.05$, specificity$= 0.89 \pm 0.09$, sensitivity$= 0.77 \pm 0.06$.

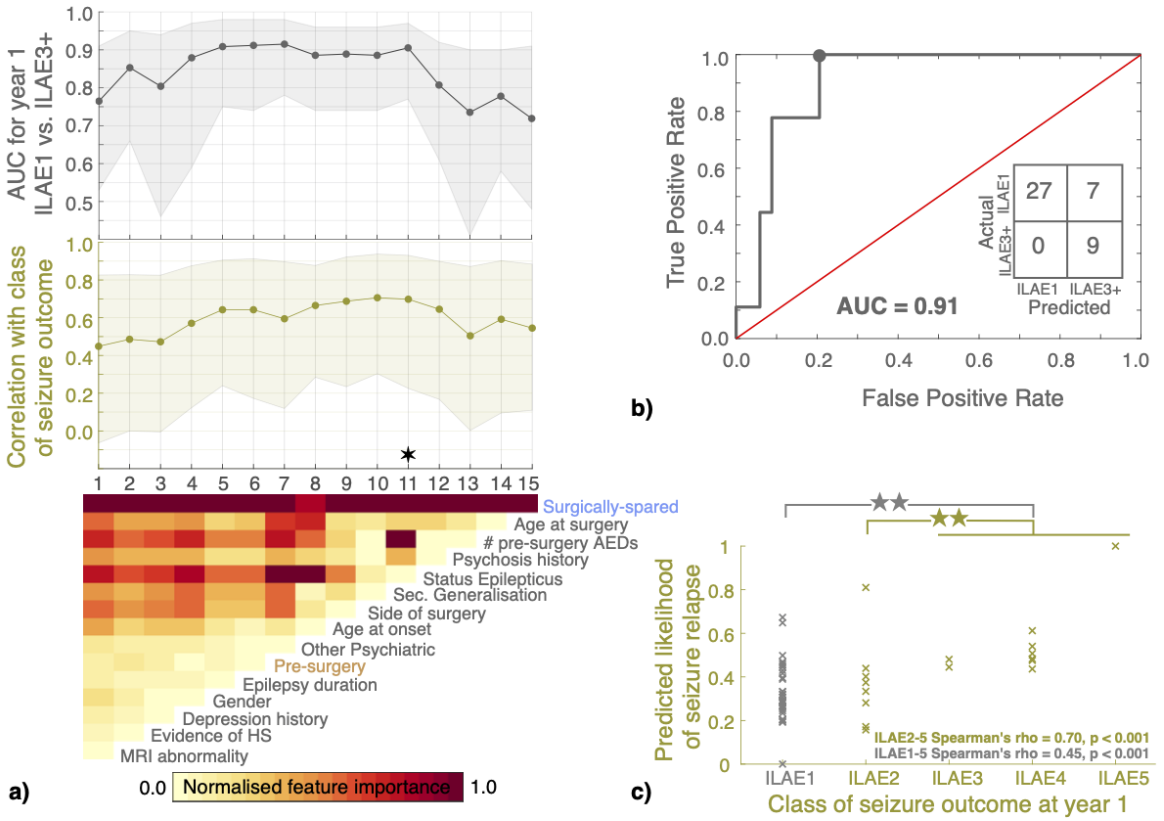

Fig. 2.5 **Prediction of seizure outcomes at year-one.** **a)** AUC of SVMs that predicted seizure-free (ILAE 1) and not seizure-free (ILAE3+) outcomes at one year after surgery are plotted in black with 95% CI shaded. Blinded to the exact ILAE categories, the model predicted 12-month likelihood of seizure relapse for each patient. The Spearman's rank correlation between likelihood of seizure relapse and the severity of surgical outcomes (ILAE class) at year-one are plotted in green with 95% CI shaded. The lower panel of **a)** shows the relative feature importance of each SVM on a normalised scale between 0 and 1. The leftmost SVM, plotted at x = 1, incorporated all 15 features (13 clinical, node abnormality in pre-surgery and surgically-spared networks) to predict seizure-free (ILAE 1) and not seizure-free (ILAE3+) outcomes at one year after surgery. Amongst all features, the relative importance of surgically-spared node abnormality was the highest whereas the relative importance of MRI abnormality was the least. Therefore, in the next iteration at $x = 2$, a new SVM was retrained using the 14 features, after removing the MRI abnormality feature. This stepwise removal of metrics was continued until only a single metric (surgically-spared node abnormality) remained. **b)** ROC curve is plotted at an example combination of features that yielded highest classification performance (AUC=0.91 [95%CI 0.77, 0.97], specificity=1, sensitivity=0.79, accuracy=0.84). **c)** At the same example point, the correlation (Spearman's rho=0.70 [95%CI 0.25, 0.93], $p < 0.001$) between the predicted likelihood of seizure relapse and the severity of seizure outcome at year 1 is shown. The predicted likelihood of seizure relapse was significantly different ($p = 0.003, d = 0.96$ [95%CI -0.29, 2.1]) between ILAE 2 ($n = 8$, median 0.35 [95%CI 0.17, 0.43]) and ILAE 3-5 patients combined ($n = 9$, median 0.48 [95%CI 0.44, 0.61]).

The lower panel in Figure 2.5(a) maps feature importance after each iteration of feature removal. The node abnormality in the surgically-spared network stood out as the most informative feature; it was more than 1.5 standard deviations away from the next most important features: age at surgery, and number of AEDs taken before surgery. Thus, including the abnormality measures to characterise pre-surgical attributes of intractable TLE patients led to a high and robust classification performance in predicting surgical outcomes at one-year after surgery.

We next analysed the scores/probabilities assigned by the model to each patient to have a not seizure-free surgical outcome. Larger probabilities indicated a greater predicted likelihood of postoperative seizure at year 1 (i.e., the ILAE 3+ group). Since the model was trained only on binary ILAE 1 and ILAE 3-5 outcomes it was blind to the spectrum of ILAE class data. We found that despite being blinded to such information, the predicted likelihood of seizure relapse was positively correlated with ILAE surgical outcome scale at year-one (Figure 2.5c). This positive association is consistent, even for the model trained using only the surgically-spared node abnormality feature (Figure 5a). Spearman's rho values are plotted at each step-wise removal of features in Figure 2.5(a) and magnified for an example point in Figure 2.5(c). To confirm this result, we applied robust regression to obtain the regression slope and tested the significance of the steepness of the regression slope using permutation test (1000 permutations, p=0.004 in Appendix A.9. Therefore, our result shows that the pre-surgical clinical profile of patients, when assessed along with the abnormality measures, can inform about the ILAE class of seizure outcomes which a patient would expect after surgery at 1 year.

How informative are the pre-surgical features in predicting seizure recurrences in the long-term? We analysed this by checking the association between the predicted likelihood of seizure relapse and the actual relapse data for patients who were seizure-free (ILAE 1,2) at year one. Patients who were not seizure-free at year one (ILAE 3-5) were not included in the relapse category. We found no association with seizure relapse when the pre-surgical features of patients were characterized using a combination of clinical and network abnormality measures (Appendix A.10). However, significant association with relapse was present at year 3, 4, and 5 when the pre-surgical features of patients were characterized using only the abnormality load in surgically-spared network (Figure 2.6). The mechanism of long-term seizure recurrence may be different from short-term, and pre-surgical clinical attributes may

be less informative. The association we found between abnormality load expected to be present in a patient after surgery and seizure recurrence motivates more investigation.

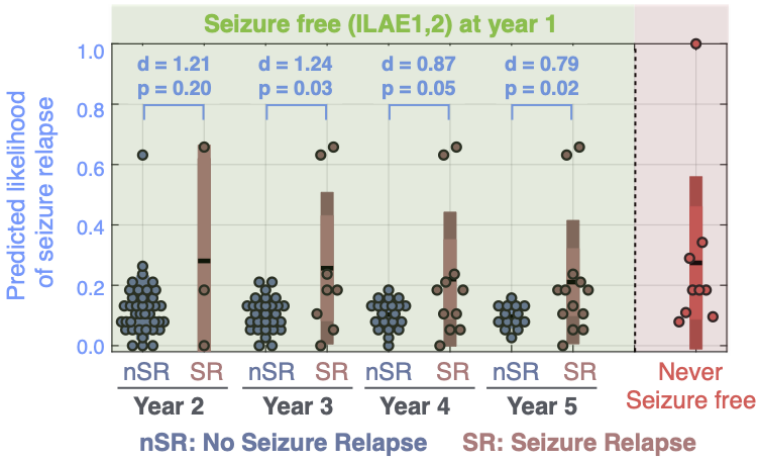

Fig. 2.6 **Predicted likelihood of seizure relapse at one-year was higher in patients who had seizure relapse at later years.** The predicted 12-month likelihood of seizure relapse was estimated from the SVM model trained with only the surgically-spared node abnormality feature. The likelihood of seizure relapse for patients who were never seizure-free (i.e. ILAE 3-5 at year 1) are shown in red. Amongst the patients who were initially seizure-free (i.e., ILAE 1 or ILAE 2 at year 1), higher likelihood of seizure relapse was predicted for those who had a subsequent relapse. This is despite the model being blinded to the outcomes at later years. *Year 2 statistical estimates:* no relapse ($n = 39$) median 0.10 [95%CI 0.08, 0.13]; relapse ($n = 3$) median 0.18 [95%CI 0, 0.66]; $p = 0.20$; $d = 1.21$ [95%CI -0.78, 9.08]. *Year 3 statistical estimates:* no relapse ($n = 29$) median 0.11 [95%CI 0.08, 0.13]; relapse ($n = 8$) median 0.18 [95%CI 0.05, 0.63]; $p = 0.03$; $d = 1.24$ [95%CI -0.19, 2.84]. *Year 4 statistical estimates:* no relapse ($n = 21$) median 0.11 [95%CI 0.08, 0.13]; relapse ($n = 11$) median 0.18 [95%CI 0.05, 0.41]; $p = 0.05$; $d = 0.87$ [95%CI -0.16, 1.7]. *Year 5 statistical estimates:* no relapse ($n = 14$) median 0.09 [95%CI 0.08, 0.13]; relapse ($n = 13$) median 0.18 [95%CI 0.11, 0.24]; $p = 0.02$; $d = 0.79$ [95%CI 0.12, 1.3].

In summary, we achieved excellent performance in predicting seizure outcomes at one year when intractable TLE patients were assessed based on abnormality measures and clinical attributes. This combined pre-surgical profiling of patient attributes was also informative about the grades of seizure outcomes (ILAE class) at year one. Beyond the first year after surgery, node abnormality in the surgically-spared networks suggested an increased risk of seizure relapses in those patients who were initially free of disabling seizures at year one.

2.5 Discussion

We investigated the association of surgical outcomes and relapse with the abnormality load computed in whole-brain pre-surgical network, and surgically-spared subnetwork. Patients were more likely to have a poorer seizure outcome at one-year post surgery or a seizure relapse in five years, if more abnormal nodes were present in the surgically-spared network. Investigating the spatial effect of surgery on abnormality load, we found that the seizure-free group of patients had a more widespread reduction of abnormal nodes. We found that the abnormality load in pre-surgery and surgically-spared networks, combined with clinical attributes of patients, generalised to predict not seizure-free outcome (between ILAE 1 and ILAE 3+) at 12-month after surgery with 100% specificity and 0.91 AUC. With this combined characterization of patient attributes, we predicted the likelihood of seizure relapse patient-specifically which were correlated with the ILAE class, hence, informative of the seizure outcome expected at 12 months after surgery. Finally, we showed that node abnormality located in the surgically-spared networks may be a marker that identifies patients who were initially seizure-free but would relapse after the first year of surgery and up to 5 years.

A recent study on a different dataset with different imaging protocols, investigated network abnormality as a personalised predictor of surgical outcomes (Bonilha et al., 2015). In that study, pre-surgery networks were constructed based on the number of streamlines connecting different regions. Similar to our study, connections between ROIs were normalised (z-transformed) against a control distribution. The similarity between our results suggest that: a) normalised patient networks using a local control distribution may enable reproducibility, comparison, and possibly grouping of patients between sites, and b) non-invasive personalised network biomarkers for predicting the likelihood of specific post-surgery outcomes in TLE are possible. We further showed the benefit of incorporating the information about the location of surgery to predict the surgical outcome.

The current standard for individualised prediction of surgical outcome primarily relies on clinical variables (Jehi et al., 2015). However, a recent review discussed discordant findings between different studies; features found predictive of seizure outcome in some studies are not predictive in others (Bonilha and Keller, 2015). Encouragingly, another study estimated the probability of seizure freedom using combinations of up to 27 clinical variables on a mixed cohort of TLE and ETLE patients (Bell et al., 2017). Our findings indicated that combining clinical variables with brain connectome derived features such as: abnormality

load in pre-surgery and surgically-spared networks, can improve prediction of surgical outcomes in the short-term. Particularly for long-term predictions, the abnormalities in the surgically-spared networks, which are expected to remain after surgery, may be a more reliable measure because they associate with relapses. It is not surprising that long-term seizure relapse is not specifically related to parameters predicting short-term outcome well, because these two responses may have very different mechanisms. Short-term failure may be caused by an incomplete resection at the time of surgery, while long term relapse may be caused by changes in the networks over time after surgery, or the development of another epileptogenic zone (Silva et al., 2020b). Hence, we propose to combine our node abnormality measure with clinical variables in a large mixed-cohort patient (Bell et al., 2017) population, to improve estimation of the probability of seizure freedom/relapse after surgery. We suggest that investigating the abnormality load in the surgically-spared network in specific lobes may reveal a stronger relationship to long-term seizure recurrence.

In combining multivariate data, machine learning techniques delineate, rank, and fit input features of the training set to draw a decision boundary in a high dimensional space that maximises prediction (Bonilha et al., 2015; Gleichgerrcht et al., 2018; Morgan et al., 2020; Munsell et al., 2015; Taylor et al., 2018). While a binary classification of seizure-free and not seizure-free outcomes at 12 months is important, predicting long-term trajectories of seizure freedom is also crucial to inform clinical management decisions. In our study, the classifier not only predicted the surgical outcome at one-year but also predicted the likelihood of seizure relapse. This additional information may be clinically useful for advising patients about their chances of poor outcome post-surgery beyond the first 12 months and represents a key novelty of our work.

The outcome of epilepsy surgery will not just depend on the brain network before the surgery but also on the location and extent of surgery (Ji et al., 2015; Taylor et al., 2018). Here, we retrospectively included the information of surgery by drawing a resection mask and inferring an expected surgically-spared network. We showed that this information improves the prediction performance more so than just the pre-surgery networks which are naïve to surgical information. A limitation of our work is that we are only inferring the expected postoperative network, rather than deriving it from postoperative dMRI data (Silva et al., 2020b; Winston et al., 2013b). However, an analysis using actual postoperative dMRI data would only have very limited value in terms of improving the pre-operative decision making, since the outcome could only be seen after the surgery has been performed. In contrast,

our approach can be used before the actual surgery to evaluate likelihood of success. A prospective application would involve drawing a resection mask for an intended surgery on sMRI of a patient acquired before surgery (Taylor et al., 2018). We envisage a software tool where multiple standard operations or tailored resections could be drawn and their impact on abnormality load compared. Such a tool could then be used to prospectively guide decision making regarding personalised resection strategies.

With regard to the extent of surgical resection, it has been shown that the amount of tissue resected does not necessarily relate to improved surgical outcome (Schramm, 2008). What is included in the resection, however, may have a significant influence on outcome (Bonilha et al., 2011; Siegel et al., 1990). The question arises: will a tailored resection, designed to reduce the number of abnormal nodes, lead to a better outcome? While more investigations are needed to confirm this hypothesis, we found that the seizure-free patient group had a more widespread reduction of abnormality load due to surgery. Simulated computer models may facilitate a more detailed analysis to investigate alternative surgical strategies in a personalised manner (Sinha et al., 2016).

Our findings must be interpreted in the context of some caveats. Node abnormality may be representative of a) network reorganisation in response to seizures, b) neurodegenerative process due to seizures, c) structures facilitating seizures, or combinations of (a)-(c). In our study we could not disentangle these aspects with respect to node abnormality. We did not detect any significant correlation between clinical variables and node abnormalities. Though our sample size is reasonably large (Bonilha et al., 2015; Gleichgerrcht et al., 2018; Keller et al., 2016; Munsell et al., 2015), it is not of the size of typical epidemiological studies. Neural architecture depends on several subject-specific factors including language dominance, handedness, and other physiological variables. These relationships may further influence the node abnormality measure. Thus, our results should motivate a larger study to test its generalisability, ideally across multiple sites. Finally, we highlight, based on the pre-surgical, surgically-spared networks, and clinical variables, the chances of *at least one* relapse in five-years. However, the trajectory of seizure remission and relapse is more complicated. Patients may have repeated remissions and relapses due to drug-effects, environmental factors, or other causes.

In summary, we have shown evidence of node abnormality being an important non-invasive marker of surgical outcome and its severity at year one post-surgery. Node abnormality may

also be related with likelihood of seizure relapse in long-term. We demonstrate improvement in prediction performance when including surgery information with the pre-surgery network and clinical data. We believe this to be an important step towards complementing clinical decision making on patient and surgery selection for intractable TLE as well as for patient counselling regarding the risks of seizure severity expected after surgery.

Chapter 3

Structural network abnormalities and focal to bilateral tonic-clonic seizures

The data in the following chapter is in press for publication in Epilepsia. Whilst minor adjustments to that article have been made in order to be consistent with this thesis format, the background, methods, results, and conclusions match those of the peer-reviewed article.

Nishant Sinha, Natalie Peternell, Gabrielle M. Schroeder, Jane de Tisi, Sjoerd B. Vos, Gavin P. Winston, John S. Duncan, Yujiang Wang, and Peter N. Taylor "Focal to bilateral tonic-clonic seizures are associated with widespread network abnormality in temporal lobe epilepsy." *Epilepsia* 2021 62(3):729-741 doi:10.1111/epi.16819.

3.1 Abstract

To identify if whole-brain structural network alterations in patients with temporal lobe epilepsy (TLE) and focal to bilateral tonic-clonic seizures (FBTCS) differ from alterations in patients without FBTCS.

We dichotomized a cohort of 83 drug-resistant patients with TLE into those with and without FBTCS and compared each group to 29 healthy controls. For each subject, we used diffusion-weighted MRI to construct whole-brain structural networks. First, we measured the extent of alterations by performing FBTCS-negative (FBTCS-) versus control and FBTCS-positive (FBTCS+) versus control comparisons, thereby delineating altered sub-networks of the whole-brain structural network. Second, by standardising each patient's networks using control networks, we measured the subject-specific abnormality at every brain region in the network, thereby quantifying the spatial localisation and the amount of abnormality in every patient.

Both FBTCS+ and FBTCS- patient groups had altered sub-networks with reduced fractional anisotropy (FA) and increased mean diffusivity (MD) compared to controls. The altered sub-network in FBTCS+ patients was more widespread than in FBTCS- patients (441 connections altered at $t > 3, p < 0.001$ in FBTCS+ compared to 21 connections altered at $t > 3, p = 0.01$ in FBTCS-). Significantly greater abnormalities–aggregated over the entire brain network as well as assessed at the resolution of individual brain areas–were present in FBTCS+ patients ($p < 0.001, d = 0.82$ [95 % CI 0.32, 1.3]). In contrast, the fewer abnormalities present in FBTCS- patients were mainly localised to the temporal and frontal areas.

The whole-brain structural network is altered to a greater and more widespread extent in patients with TLE and focal to bilateral tonic-clonic seizures. We suggest that these abnormal networks may serve as an underlying structural basis or consequence of the greater seizure spread observed in FBTCS.

3.2 Introduction

Focal to bilateral tonic-clonic seizures (FBTCS) of temporal lobe origin rapidly propagate to widespread brain areas, although with variable patient-specific propagation patterns and clinical characteristics (Jobst et al., 2001; Yoo et al., 2014). FBTCS are the most severe

form of epileptic seizures that predispose patients to high risk of sudden unexpected death in epilepsy (SUDEP) and seizure-related injuries (Devinsky et al., 2016; Harden et al., 2017; Lawn et al., 2004). FBTCS are an adverse prognostic factor for seizure freedom after temporal lobe resection (Bell et al., 2017; Bone et al., 2012; Keller et al., 2015). It remains unclear why temporal lobe seizures generalise in some patients but not in others (Hemery et al., 2014; Shorvon et al., 2018). It is crucial to identify factors that make some patients susceptible to FBTCS despite taking seizure suppressing medications.

Recognising the need to quantify patient susceptibility to FBTCS, some studies investigated a range of clinical factors to differentiate patients with and without FBTCS (Baud et al., 2015; Bone et al., 2012), showing positive association with the presence of hippocampal sclerosis and negative association with ictal speech and pedal automatism (Bone et al., 2012). Many studies have suggested that impairments in specific brain regions support FBTCS, after finding disrupted structure and function in circuits mediated by thalamus and basal ganglia (Blumenfeld et al., 2009; Caciagli et al., 2020; Chen et al., 2018; He et al., 2019, 2015; Keller et al., 2015; Peng and Hsin, 2017; Yang et al., 2017). It has also been suggested that FBTCS have a different mechanism to primary generalised seizures, with more complex patient-specific spread (Brodovskaya and Kapur, 2019; Dabrowska et al., 2019; Rektor et al., 2009; Shorvon et al., 2018; Sinha et al., 2019; Wieshmann et al., 2015). There is a need to investigate the full complexity of brain networks (Enatsu et al., 2012), beyond the canonical thalamocortical pathways (Blumenfeld et al., 2009), to delineate networks underlying FBTCS.

Patients with drug-resistant TLE are known to have structural abnormalities extending beyond the hippocampus and temporal lobe, forming a network of epileptogenic brain structures (Bonilha et al., 2013; Concha et al., 2012; Deleo et al., 2018; Otte et al., 2012). Greater whole-brain structural network abnormalities predispose patients to persistent seizures after TLE surgery (Bonilha et al., 2015; Sinha et al., 2020). These abnormalities may be associated with the distributed nature of epileptic activity, the pathophysiology of seizure onset and propagation, and the response to medical and surgical therapies (Bernhardt et al., 2015; Sinha et al., 2016). There is a dearth of information on how whole-brain structural network abnormalities differ between patients with and without FBTCS.

In this study, we investigated the abnormalities in the whole-brain structural network of TLE patients with and without FBTCS. We hypothesised that those with FBTCS would have more

widespread abnormalities of white-matter pathways and to test this, we mapped the spatial arrangement of alterations in the whole-brain structural network of TLE patients with and without FBTCS (Bonilha et al., 2015; Sinha et al., 2020; Zalesky et al., 2010). We show that patients with localised spread of focal-onset seizures have localised alterations in brain areas neighbouring seizure onset, whereas patients with FBTCS have marked widespread abnormalities across the whole-brain.

3.3 Methods

3.3.1 Participants

We studied 83 patients with drug-resistant unilateral TLE who were undergoing pre-surgical evaluation at the National Hospital of Neurology and Neurosurgery, London, United Kingdom, and 29 controls. The controls in this study were demographically matched and recruited from the local population through advertisements. All controls were screened as per an institute approved proforma to exclude medical history of neurological or psychiatric problems including drug/alcohol misuse. Clinical diagnosis of FBTCS was based on video-EEG telemetry, EEG, and historical data. Sixty patients had a history of temporal lobe seizures with FBTCS, and 23 patients did not. The three groups–TLE with FBTCS (FBTCS+), TLE without FBTCS (FBTCS-), and controls–were not significantly different in terms of age and gender. Patient details are provided online in Table S1 at doi:10.1111/epi.16819. and summarised in Table 3.1. Data were analysed in this study under the approval of the Newcastle University Ethics Committee (reference number 1804/2020).

3.3.2 MRI acquisition and data processing

MRI data were acquired on a 3T GE Signa HDx scanner (General Electric, Waukesha, Milwaukee, WI). Standard imaging gradients with a maximum strength of $40 mTm^{-1}$ and slew rate $150 Tm^{-1}s^{-1}$ were used. All data were acquired using a body coil for transmission, and 8-channel phased array coil for reception. Standard clinical sequences were performed including a coronal 3D T1-weighted volumetric acquisition (matrix, $256 \times 256 \times 170$; in-plane resolution, 0.9375×0.9375 mm with slice thickness 1.1 mm). For each participant, diffusion-weighted magnetic resonance imaging (dMRI) data was acquired using a cardiac-triggered single-shot spin-echo planar imaging sequence with echo time=73ms.

Table 3.1 Demographic and clinical data of patients

	FBTCS+	*FBTCS-*	*Controls*	*Significance*
Patients (n)	60	23	29	
Sex (Male/Female)	24/36	8/15	12/17	$\chi^2 = 0.03, p = 0.85$ (FBTCS±) $\chi^2 = 0.01, p = 0.91$ (FBTCS+C) $\chi^2 = 0.03, p = 0.84$ (FBTCS-C)
Age at dMRI (yrs, mean ± std)	38.8 ± 12.3	35.3 ± 8.4	38.0 ± 12.0	$p_{\text{FBTCS}\pm} = 0.20$ $p_{\text{FBTCS+C}} = 0.70$ $p_{\text{FBTCS-C}} = 0.67$
Age at onset (yrs, mean ± std)	15.2 ± 11.1	16.1 ± 9.9	N/A	$p = 0.51$
Epilepsy duration (yrs, mean ± std)	24.7 ± 14.5	20.4 ± 12.4	N/A	$p = 0.26$
Side (Left/Right)	32/28	10/13	N/A	$\chi^2 = 0.31, p = 0.57$
HS, n(%)	36 (60%)	9 (39%)	N/A	$\chi^2 = 2.14, p = 0.14$
Surgical outcome (SF/nSF)	28/32	12/11	N/A	$\chi^2 = 0.04, p = 0.84$

Abbreviations: *n* number of patients; *HS* Hippocampal Sclerosis; *yrs* years. Surgical outcomes are defined as seizure free (*SF*) or not seizure free (*nSF*) based on ILAE outcomes recorded in two years after the surgery. Patients who remained ILAE 1 in both year 1 and year 2 after surgery were deemed seizure free or else not seizure free.

Sets of 60 contiguous 2.4mm thick axial slices were obtained covering the whole brain, with diffusion sensitizing gradients applied in each of 52 noncollinear directions (b-value of $1200 mm^2 s^{-1}, \delta = 21 ms, \Delta = 29 ms$ using full gradient strength of $40 mT m^{-1}$) along with 6 non-diffusion weighted scans. The gradient directions were calculated and ordered as described elsewhere Cook et al. (2007). The field of view was 24×24cm, and the acquisition matrix size was 96×96, zero filled to 128×128 during reconstruction, giving a reconstructed voxel size of $1.875 \times 1.875 \times 2.4$mm. The diffusion MRI acquisition time for a total of 3480 image slices was approximately 25min (depending on subject heart rate).

Diffusion MRI data were first corrected for signal drift, then eddy current and movement artefacts were corrected using the FSL eddy_correct tool (Vos et al., 2016). The b-vectors were then rotated appropriately using the 'fdt-rotate-bvecs' tool as part of FSL. The diffusion data for each subject was registered and reconstructed to the standard ICBM-152 space using the q-space diffeomorphic reconstruction implemented in DSI studio (Yeh and Tseng, 2011). DSI studio fitted a diffusion tensor imaging (DTI) model on the diffusion MRI data. DTI

model assumes that the velocity of water diffusion follows a 3D Gaussian distribution, and the tensor calculated is exactly the covariance matrix of the Gaussian. The reconstruction performed eigen analysis on the calculated tensor and exported the fractional anisotropy (FA) and mean diffusivity (MD) maps as implemented elsewhere (Jiang et al., 2006).

3.3.3 Construction of structural brain networks

For each participant, we constructed a structural brain network consisting of nodes and connections between the nodes as described previously (Silva et al., 2020a). We defined 90 contiguous cortical and subcortical regions (nodes) from the AAL parcellation atlas as the nodes of the network (Tzourio-Mazoyer et al., 2002). To identify the connectivity between the nodes, we applied a whole-brain neuroanatomically-verified atlas of the structural connectome comprising of 500,000 streamlines obtained from deterministic fibre tracking (Yeh et al., 2018). Nodes i and j were connected if a streamline ended in them. We weighted the connectivity across all streamlines that connect each pair of nodes by averaging the FA and MD values from the diffusion tensor imaging measurements. Repeating this process for each pair of nodes i and j resulted in two (FA and MD) weighted connectivity matrices of size 90×90 per participant. The density of connections in the connectivity matrices across all participants was constant, which is a desirable graph property for cross-sectional group analysis (Wijk et al., 2010).

3.3.4 Network alterations assessed from network-based statistics

We applied network-based statistics (NBS) to compare the structural brain network connectivity of a) FBTCS+ patients vs controls, and b) FBTCS- patients vs controls. NBS is a widely used statistical approach for comparing network connections in two groups that identifies altered subnetworks (Zalesky et al., 2010).

In NBS analysis, we first used t-statistics to test each connection between nodes i and j of the connectivity matrix between patients and controls, resulting in a t-score matrix. Second, from the t-score matrix, we obtained a binary matrix, identifying those connections that showed a t-value higher than a set t-score threshold, and zeros otherwise. Third, from the binary matrix, we identified the size of the largest connected component, a subnetwork of nodes that showed alteration in patients. The size of the component is defined as the number of connections in the subnetwork, which we refer to as the extent of alteration.

Fourth, we employed permutation testing to determine if the size of altered subnetwork identified in patients occurs by chance. In permutation testing, we randomly permuted the group assignment of connectivity matrices between patients and controls 5000 times and computed the size of the largest connected component to obtain a null distribution. We then assigned a p-value to the observed altered component size by computing the percentage of null-distribution that exceeded the size of the observed altered subnetwork in patients. Fifth, we repeated the entire NBS analysis described above for t-score thresholds ranging from 0.05 to 5 in steps of 0.05 to quantitatively verify the consistency of our findings independent of threshold choice.

3.3.5 Node alterations assessed from node abnormality

Node abnormality is a measure that identifies how the distribution of altered connections in a network may impact the nodes that they connect. Building on the emerging concepts of epilepsy being a disorder of abnormal nodes and networks (Bonilha et al., 2015; Sinha et al., 2020), we premised that nodes with more abnormal connections, relative to their total number of connections, are more likely to have altered function than a node with no or fewer abnormal connections. Notably there are two aspects to our premise: a) identification of abnormal connections, and b) identification of abnormal nodes.

First, we identified the abnormal connections in each subject. For every connection present between node i and j in the structural network of a subject, we obtained a connection distribution from the equivalent connection between node i and j of the control networks. We calculated the z-score of that connection as the number of standard deviations away from the mean, with the mean and standard deviation derived from the control distribution. For control subjects, we held out each control, computed the mean and standard deviation of each connection from the remaining controls, and computed the z-scores of the control's edges relative to these distributions. By repeating this process for every connection, we standardised the FA weighted connectivity matrices against controls, obtaining a 90×90 z-score connectivity matrix per subject. From the z-score connectivity matrix of a subject, we computed a binary matrix with ones for those connections that showed a z-value higher than a set z-score threshold and zeros otherwise. The connections in this binary network are the abnormal connections with a high z-score; we identified different levels of abnormal connections by setting z-score threshold ranging from 1.5 to 3.5 in steps of 0.1.

Second, we identified abnormal nodes. For each node of the structural connectivity matrix we calculated node abnormality, defined as the ratio between the number of abnormal connections to the total number of connections of the node. Specifically, we obtained the ratio between the node degree of the binary network of abnormal connections derived above with the node degree of the non-binarized z-score network. From the node abnormality measure, we categorised each node as either normal or abnormal by applying a node abnormality threshold ranging from 0.01 to 0.20 in steps of 0.01. Thus, the node abnormality threshold identifies abnormal nodes by specifying the required proportion of abnormal connections in a node to render it abnormal.

By counting the total number of abnormal nodes in the whole-brain network at each pair of z-score and node abnormality thresholds, we derived the whole-brain abnormality load. Likewise, for brain sub-networks connecting nodes within six brain areas—temporal (18 nodes), subcortical (14 nodes), frontal (26 nodes), parietal (14 nodes), occipital (12 nodes), and cingulate (6 nodes)—we repeated the above analysis, determining the abnormality load per brain area per subject.

Finally, we compared the abnormality between FBTCS+ patients vs controls and FBTCS- patients vs controls at three spatial resolutions: a) at the gross resolution, the abnormality load of the whole-brain networks; b) at the coarse resolution, the abnormality load of six brain areas; and c) at the fine resolution, the node abnormality of individual abnormal nodes spread throughout the brain. In comparing patients and controls, we treated the abnormality in controls as the baseline measurement and applied estimation statistics to quantify abnormality in patients above and beyond that in controls (Ho et al., 2019). At the fine resolution, we also compared the node abnormality at each ROI directly between FBTCS+ and FBTCS- patient groups.

3.3.6 Statistical analysis and data availability

We followed a case-control approach to evaluate if there are more alterations in structural brain network of FBTCS+ patients compared to controls than FBTCS- patients compared to controls. We assessed the alterations by applying network-based statistic and node abnormality approaches.

Network-based statistic is a non-parametric method available as a MATLAB toolbox. Statistical tests performed within NBS analysis were a) one-tailed t-test to calculate t-score

matrices, and b) one-tailed permutation test (5000 permutations) to assign p-value to the size of the abnormal subnetwork. We set the significance level at 0.05 i.e., an altered subnetwork in NBS was reported only when $p < 0.05$.

In the node abnormality analysis, we identified a z-score and node abnormality threshold pair which was the most discriminatory (highest effect size) between FBTCS+ and FBTCS- patients Appendix B. For statistical quantification, we first applied non-parametric Kruskal–Wallis test to check the null hypothesis that abnormality load in control, FBTCS-, and FBTCS+ originate from the same distribution. We then applied pair-wise estimation statistics reporting Cohen's d score and p-values from one-tailed non-parametric Wilcoxon rank sum test. Estimation statistics uses a combination of effect sizes and confidence intervals to analyse data and interpret results; they are considered more informative than null hypothesis significance testing (Ho et al., 2019). We measured the effect size non-parametrically by computing area under receiver operating characteristic curve (AUROC). We computed 95% bootstrap confidence intervals of Cohen's d and AUROC using a bias-corrected and accelerated percentile method from 5000 bootstrap resamples with replacement.

We have made available all the anonymised QSDR reconstructed brain networks of 83 patients and 29 controls included in this study at http://doi.org/10.1111/epi.16819

3.4 Results

Our main objective was to investigate if the deviation in brain network structure from the normal range would be greater in patients with a history of FBTCS. We inferred the normal range of alterations from control population and assessed the deviation in brain networks of patients in which focal seizures do not generalise (FBTCS-) and generalise (FBTCS+). We hypothesised that most of the brain network structures in FBTCS- patients would be in the normal range, except some localised alterations in the temporal lobe. On the other hand, for FBTCS+ patients, we hypothesised widespread alterations in brain networks given the rapid generalisation of focal seizures to recruit widespread brain areas. Figure 3.1 summarises our overall approach.

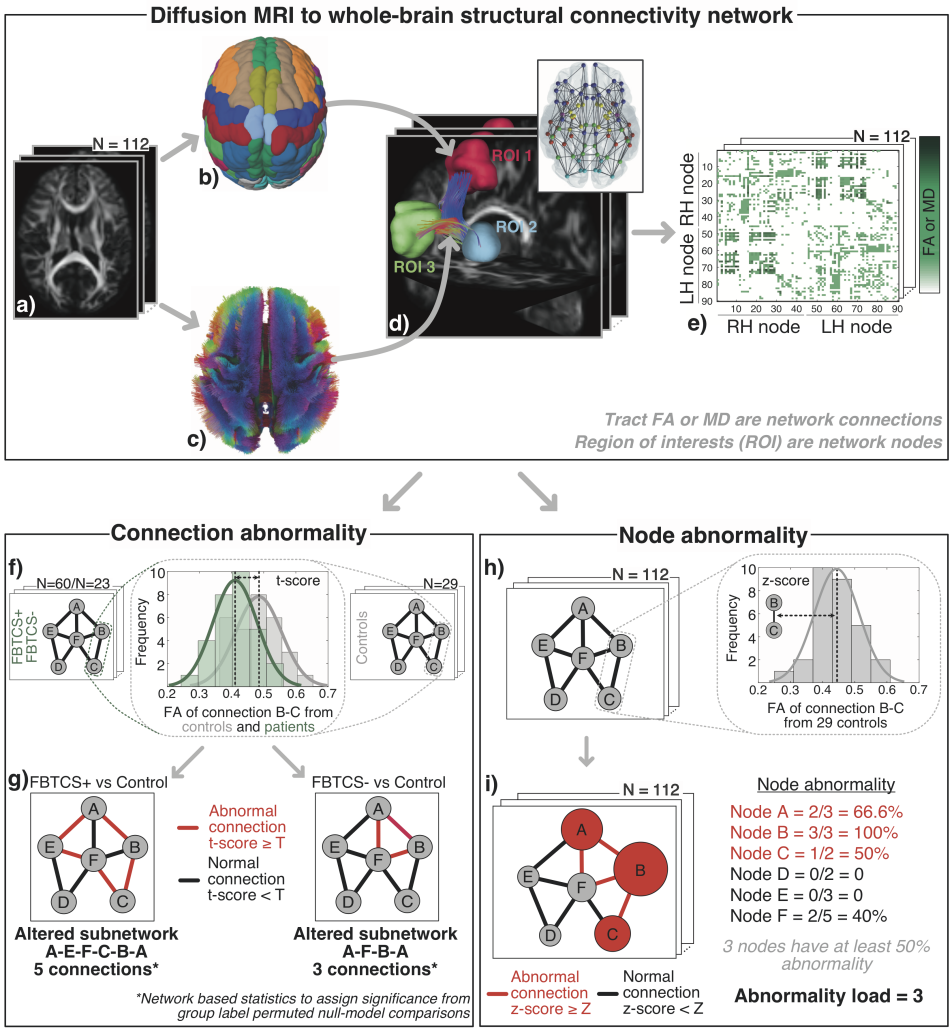

Fig. 3.1 Overall approach (continued...)

Fig. 3.1 **Overall approach: Diffusion MRI to whole-brain structural connectivity network. a)** Diffusion MRI data from 112 participants (60 FBTCS+ patients, 23 FBTCS- patients, and 29 controls) were QSDR reconstructed to align with the ICBM-152 standard space. **b)** AAL parcellation atlas defined 90 cortical and subcortical regions of interest (ROIs). **c)** The white-matter streamlines constrained with neuroanatomical priors defined the connections between the ROIs. Streamlines are colour coded as per the standard convention to indicate direction—red, left-right; green, anterior-posterior; blue, superior-inferior. **d)** Three example ROIs with the streamlines ending in them as connections. By delineating connections between all pairs of ROIs, we derived whole-brain structural network for each participant (illustrated in the inset). **e)** A network represented as connectivity matrix with ROIs as nodes on the x and y axes and connections encoded as the matrix element. We weighted the connections by averaging the fractional anisotropy or mean diffusivity values along the streamlines from diffusion tensor imaging measurements. Next, we assessed connection abnormality and node abnormality on these whole-brain structural connectivity networks. For simplicity, we illustrate these concepts for an example 6 node network. **Connection abnormality. f)** At every connection of FBTCS+/FBTCS- patient group and control group, we computed the t-score as illustrated for an example FA distribution of the connection B-C. **g)** We defined abnormal (normal) connections as those above (below) a set t-score threshold, T. By tracing the interconnected patterns of abnormal connections, we delineated altered subnetwork, as shown in red, for FBTCS+ vs control and FBTCS- vs control comparisons. Network based statistics assessed the size of altered subnetwork from chance-level occurrences in null-models and assigned significance on the extent of alteration detected in FBTCS+ and FBTCS- patient groups. **Node abnormality. h)** We computed z-score at each connection for every participant from the equivalent connection distribution in controls (illustrated for an example connection B-C). **i)** We defined connections with z-score higher or lower than a set threshold, Z, as abnormal (in red) or normal (in black). Node abnormality is ratio of abnormal connections to the total number of connections in a node (illustrated by the size of the nodes). We identified abnormal nodes, shown in red, as those above a set node abnormality threshold, consequently, quantifying abnormality load as the total number of abnormal nodes in the network.

3.4.1 Widespread network alteration associated with secondary generalisation of temporal lobe seizures

We investigated the alterations in brain networks of patients at the resolution of individual connections to identify the abnormal subnetwork and assess how large that subnetwork is in FBTCS+ and FBTCS- patients. We assumed that an interconnected configuration of altered connections—rather than altered connections in isolation or distributed randomly—would be the basis for focal onset seizures either remaining localised to a few areas or rapidly recruiting widespread areas. Therefore, we applied Network Based Statistics (NBS) to identify altered

clusters of connections by comparing (i) FBTCS+ patients and controls, and (ii) FBTCS- patients and controls.

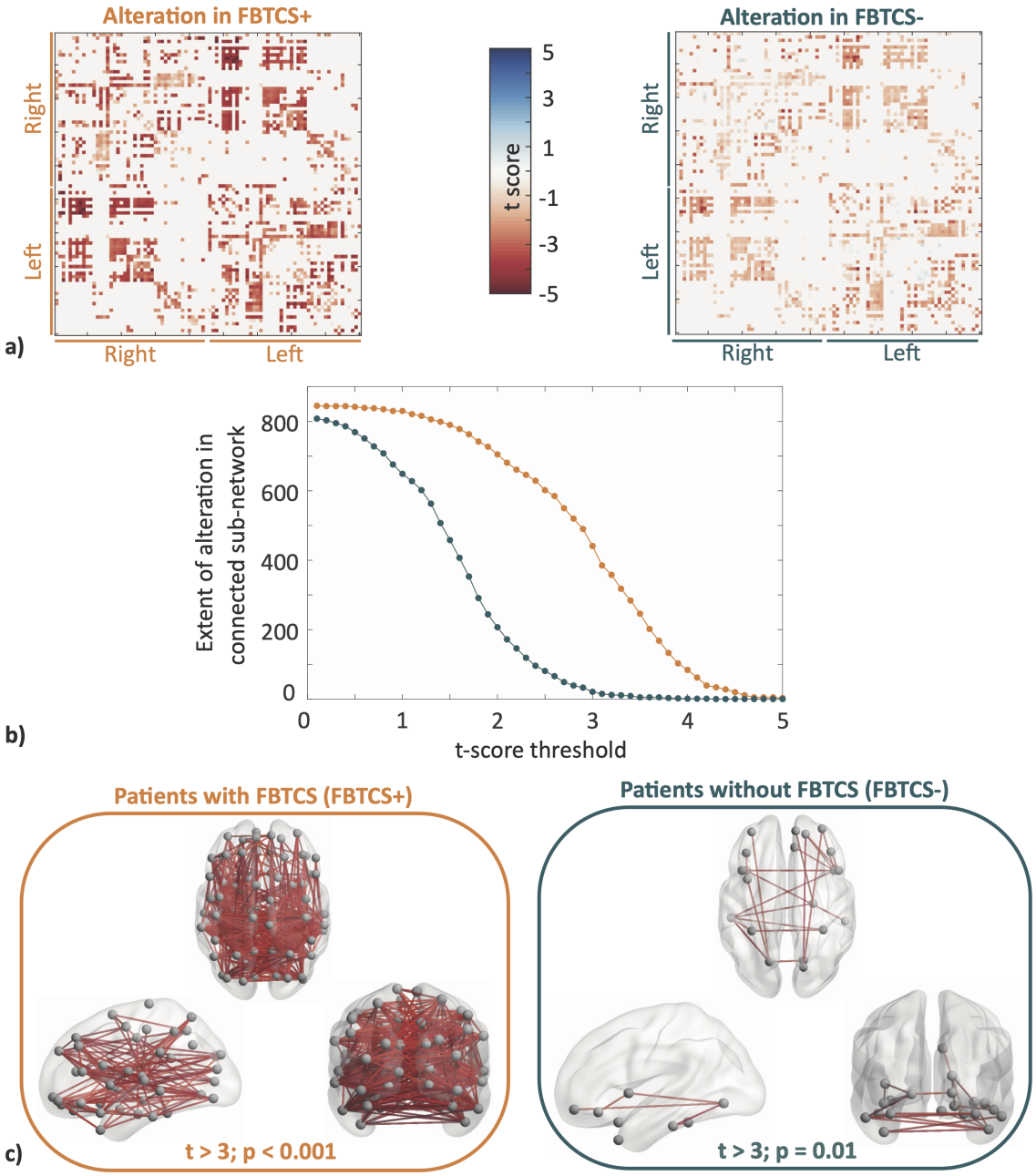

Fig. 3.2 Widespread network alteration associates with secondary generalisation of temporal lobe seizures (continued...)

Comparing FA weighted brain networks, we found that FBTCS+ patients have more widespread reductions in FA in many more connections than FBTCS- patients. Figure

Fig. 3.2 **Widespread network alteration associates with secondary generalisation of temporal lobe seizures.** We applied Network Based Statistics (NBS) to compare FA weighted connectivity matrices of FBTCS+ and FBTCS- patient groups with the control group. Panel **a)** illustrate alteration of each connection quantified by t-scores computed within the NBS analysis for FBTCS+ vs. control group comparison on the left and FBTCS- vs. control group comparison on the right. Negative (positive) t-score indicates reduction (increase) in FA of patients compared to controls. We found that the lower negative t-scores were widespread across many connections in FBTCS+ patients compared to FBTCS- patients. **b)** Applying NBS analysis, we identified significantly reduced subnetwork (connected component) at pre-specified t-score thresholds in FBTCS+ and FBTCS- patient groups compared to control group. The number of edges contained in the altered subnetwork represents the extent of alteration. We detected that the FBTCS+ patients (in orange) have higher extent of alteration than the FBTCS- patients (in teal) across all t-score thresholds. **c)** An example of significantly reduced connected subnetwork in FBTCS+ and FBTCS- patients; FA at every edge of this subnetwork was reduced in patient with respect to controls with $t > 3$. While the altered subnetwork is widespread in FBTCS+ patient group (upper panel), it is limited primarily to the regions in the temporal and frontal lobes in FBTCS- patient group (lower panel).

3.2a illustrates these alterations using t-statistics of the connections between regions. For a range of t-score thresholds we applied NBS delineating altered topological cluster i.e., sub-network of interconnected connections in which the t-score of all connections are more than the specified threshold. Figure 3.2b illustrates the extent of alteration by plotting the number of connections in the altered subnetwork for FBTCS- vs control and FBTCS+ vs control comparisons. We found, across all t-score thresholds, a larger altered subnetwork in FBTCS+ than FBTCS- patients. Figure 3.2c maps the spatial location of the altered connections at an example t-score threshold, $t = 3$. We found that in FBTCS- patients the altered connections were localised in a subnetwork spanning temporal and frontal regions. However, in FBTCS+ patients the subnetwork of altered connections was widespread, spanning many brain regions.

We observed similar results by applying the same analysis on a) networks weighted by mean diffusivity in Appendix B.1, and b) separately analysing left TLE and right TLE patients in Appendix B.2.

In summary, we found that most of the connections in FBTCS- patients were in the normal range of healthy controls; the altered connections formed a subnetwork localising primarily in the temporal and frontal areas. In contrast, in FBTCS+ patients, many connections deviated

from the normal range of healthy controls comprising a widespread subnetwork including brain regions distant from the temporal lobe.

3.4.2 Abnormality load and its spatial distribution associated with secondary generalisation of temporal lobe seizures

Premising that the spatial arrangement of abnormal regions would relate to the site of seizure onset and spread, we mapped the abnormality of each region (or node) in the brain network. Specifically, for every subject we computed node abnormality—the ratio of abnormal connections to the total number of connections in a node—followed by the identification of abnormal nodes (Sinha et al., 2020). We termed the total number of abnormal nodes at any given z-score and node abnormality threshold pairs as the abnormality load (see Appendix B.3 and Methods for details). By comparing the abnormality load in controls, FBTCS+, and FBTCS- patients, we determined the regions that had abnormalities outside the normal range of controls.

First, at the entire brain network level we found significant difference in abnormality load by comparing controls, FBTCS-, and FBTCS+ patients ($\chi^2 = 13.9$, Kruskal-Wallis $p < 0.001$). The abnormality load in the FBTCS+ patient group was significantly higher than the FBTCS- patient and control groups (Figure 3.3a, upper panel). The estimation plot (Figure 3.3a, lower panel) shows that the effect size of abnormality load between FBTCS- vs control is lower than FBTCS+ vs control. Statistical estimates: FBTCS- vs. control: $p = 0.04, d = 0.4$ [95%CI -0.17, 1]; FBTCS+ vs control: $p < 0.001, d = 0.82$ [95%CI 0.32, 1.28]; FBTCS+ vs FBTCS-: $p = 0.03, d = 0.44$ [95%CI -0.07, 0.92]. Therefore, our results indicated that the whole-brain abnormality load in FBTCS- patient group was similar to the control group, and both were substantially lower compared to the FBTCS+ patient group.

Second, at the resolution of individual lobes/areas (Figure 3.3b), we found that abnormality load in FBTCS+ patients was substantially higher than controls across all lobes. In contrast, FBTCS- patients had substantially more abnormality load than controls only in the left temporal and left frontal lobes; other lobes, where seizures typically do not spread to, were not different from the baseline control level.

Third, at a finer spatial resolution of 90 parcellated regions, we compared the node abnormality of every node between FBTCS- vs control and FBTCS+ vs control. By flipping the ROIs between left and right hemisphere of the left TLE patients, we expressed each ROI as either

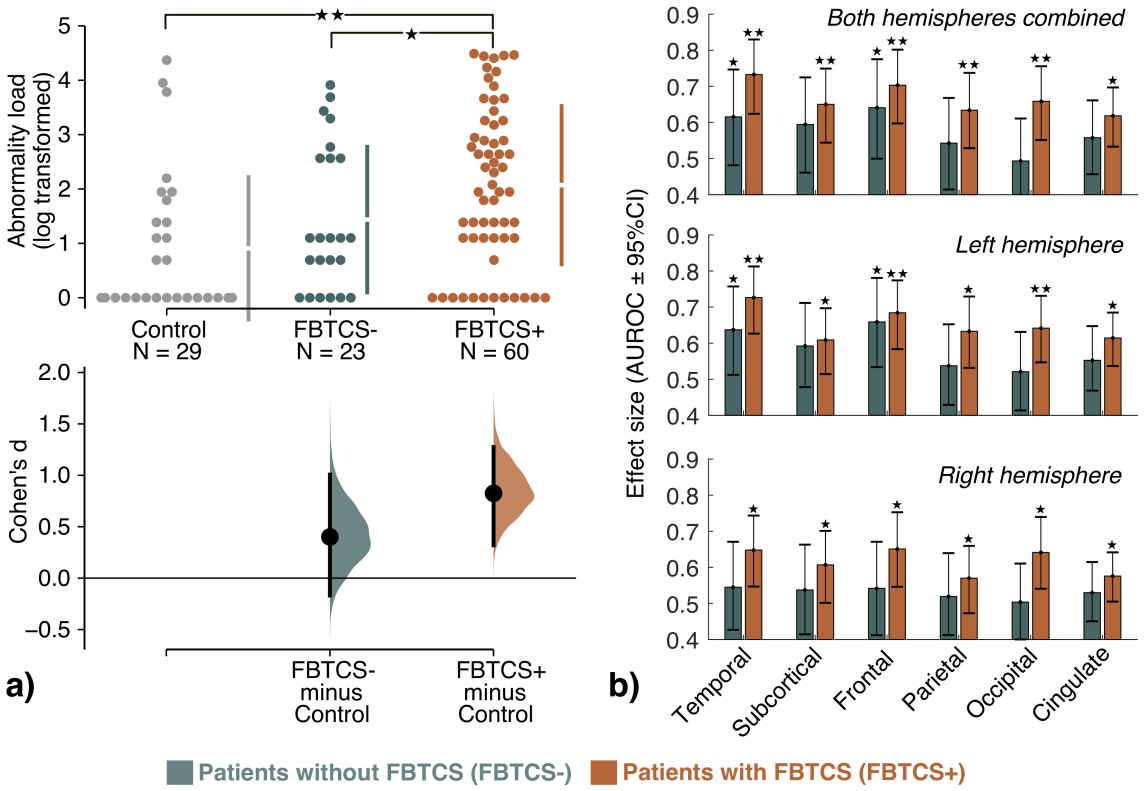

Fig. 3.3 **Abnormality load and its spatial distribution associate with secondary generalisation of temporal lobe seizures. a)** Abnormality load i.e., the total number of abnormal brain regions, is plotted on the estimation plot for control, FBTCS-, and FBTCS+ groups. Each dot represents a subject, the vertical lines represent the group mean with group standard deviation, and the lower panel shows the point estimate of Cohen's d with 95%CI from 5000 bootstrap resampling with replacement. We found that the abnormality load was significantly higher for FBTCS+ vs. control group comparison as opposed to FBTCS- vs control group comparison. We also detected that the abnormality load in FBTCS+ group was significantly higher than FBTCS- group. Statistical estimates— FBTCS- vs. control: $p = 0.04, d = 0.4$ [95%CI -0.17, 1]; FBTCS+ vs control: $p < 0.001, d = 0.82$ [95%CI 0.32, 1.28]; FBTCS+ vs FBTCS-: $p = 0.03, d = 0.44$ [95%CI -0.07, 0.92]. **b)** At the resolution of individual lobes, the bar plot illustrates the effect size of abnormality load to discriminate between FBTCS- vs. control (in teal) and FBTCS+ vs. control (in orange). We found that across all lobes, taken individually as left/right or combined, abnormality load in FBTCS+ was significantly higher than the control group. In contrast, in FBTCS- group only the abnormality load in temporal lobe (left and left-right hemisphere combined) was significantly higher than the control group. Two stars represent $p < 0.005$ and single star represents $0.005 < p < 0.05$.

ipsilateral or contralateral to seizure focus. The mean node abnormality in FBTCS+ patients was significantly higher than FBTCS- patients in 29 ipsilateral and 27 contralateral ROIs, with the highest prevalence in the ROIs belonging to subcortical and parietal areas (Figure

3.4a). Appendix B.4 shows consistency of these results across a range of z-score thresholds. Figure 3.4b-c maps the node abnormality at each ROI for FBTCS- and FBTCS+ patient group, the size of ROIs is drawn proportional their mean node abnormality. Many nodes in FBTCS+ patients have abnormalities greater than controls; abnormal nodes in FBTCS- patients are mostly localised in the ipsilateral temporal and frontal lobes.

In summary, we found that the abnormal nodes are spatially correlated with the site of seizure onset and spread. Patients in the FBTCS- group displayed localised abnormalities mainly in the temporal and frontal lobes whereas FBTCS+ patients displayed widespread abnormalities. On average, FBTCS+ patients have significantly higher node abnormality than FBTCS- patients across many widespread ROIs, including subcortical and parietal areas.

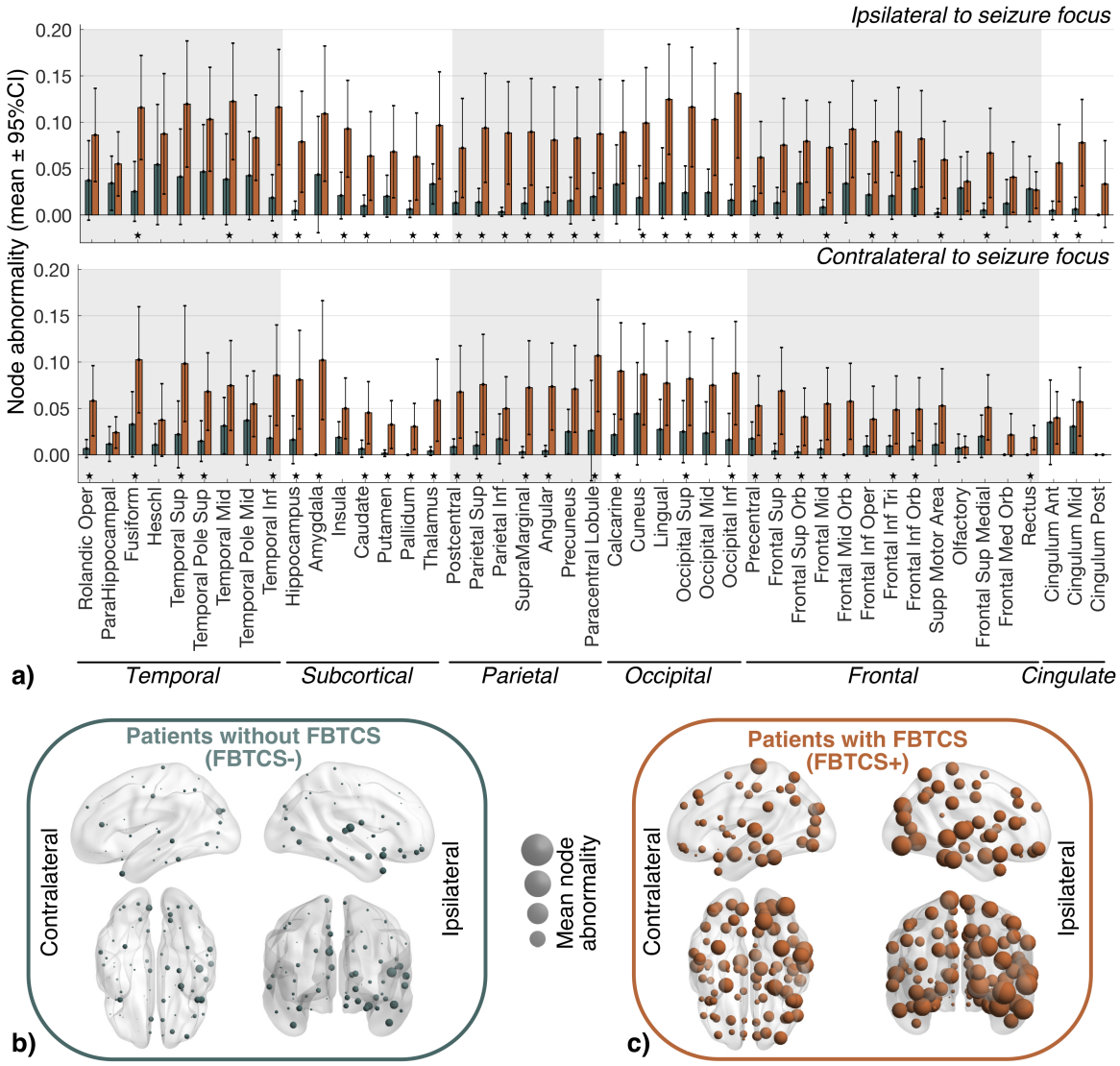

Fig. 3.4 **Node abnormality in regions ipsilateral and contralateral to seizure focus between patients with and without FBTCS. a)** At every ROI expressed as ipsilateral or contralateral to seizure focus, we computed the mean node abnormality with 95%CI at z-score>2.5. Node abnormality in ipsilateral hemisphere was higher than the contralateral hemisphere. FBTCS+ patient group (in orange) had greater node abnormality than FBTCS- patient group (in teal) across all ROIs. Specific ROIs with significantly higher node abnormality in FBTCS+ group than in FBTCS- group are highlighted by stars representing $p < 0.05$ after Benjamini-Hochberg FDR correction for multiple comparisons. Lobe-wise occurrence of ROIs with significantly higher node abnormality in FBTCS+ group were: temporal 8/18 (44%), subcortical 11/14 (78%), parietal 12/14 (85%), occipital 8/12 (66%), frontal 15/26 (57%), cingulate 2/6 (33%). **b-c)** Mean node abnormality is mapped for FBTCS- patients in panel **(b)** and FBTCS+ patients in panel **(c)**. The size of the nodes, shown by spheres, are scaled by their mean node abnormality value. We found that in both patient groups node abnormality is higher in the ipsilateral temporal lobe relative to the abnormality in rest of the brain. High node abnormality was widespread in FBTCS+ patient group, whereas in FBTCS- patient groups the abnormal nodes were localised mainly in the temporal and frontal areas.

3.5 Discussion

We investigated if widespread brain network abnormalities were present in patients with a history of FBTCS and drug-resistant TLE. By comparing controls and patients with and without FBTCS, we mapped alterations in brain networks at the resolution of individual connections, nodes, lobes, and the whole-brain. In patients without a history of FBTCS, abnormalities were localised mainly in temporal and frontal areas. In contrast, abnormalities were widespread and bilateral in patients with FBTCS. Regions in the subcortical and parietal lobes, showed a marked increase in node abnormality in TLE patients with FBTCS. Abnormality load, a subject-specific measure of whole-brain abnormality, placed FBTCS patients at the higher end of the abnormality spectrum, followed by patients without FBTCS and then controls.

Alterations of white-matter tracts, generally characterized by reduced anisotropy and increased diffusivity, are a feature of TLE (Otte et al., 2012). Here, we additionally showed higher and more widespread alterations in TLE patients with FBTCS. Pseudo-prospective analysis (i.e., holding-out a few patients as test cases, akin to new incoming patients) from cross-validated machine learning models suggested the amount of abnormality expected to remain after surgery is an important factor determining seizure recurrence (Sinha et al., 2020; Taylor et al., 2018). Other studies have shown an association between history of FBTCS and seizure outcome after TLE surgery (Bone et al., 2012; Keller et al., 2015). Taken together, we suggest abnormality in whole-brain structural connectivity may underpin both post-surgical seizure recurrence and pre-surgery FBTCS occurrence.

The pathophysiology of FBTCS are understood to involve disrupted network interactions between different brain areas. Local ictal discharges bilaterally propagate to brainstem motor areas via the corpus callosum to trigger the tonic-clonic phase (Brodovskaya and Kapur, 2019; Wieshmann et al., 2015). Motor areas project excitatory activity to the thalamic nuclei and subcortical structures. From the thalamocortical projections, the excitatory seizure activity propagates to widespread areas after the inhibitory process fails at the basal ganglia (Blumenfeld et al., 2009; He et al., 2019). Indeed, structural and functional abnormalities have been reported in these areas in patients with FBTCS (Blumenfeld et al., 2009; Chen et al., 2018; Peng and Hsin, 2017; Wieshmann et al., 2015; Yang et al., 2017). This hypothesis about the propagation model of FBTCS has primarily been supported by studies incorporated functional imaging modalities and/or T1-weighted MRI. Surprisingly, only a few studies

have utilised diffusion MRI to study FBTCS, limiting its application to thalamus associated fibre bundles (Chen et al., 2018; Peng and Hsin, 2017). We utilised diffusion MRI to study the whole-brain structural network in FBTCS. Studying one of the largest patient cohorts at a single centre, we found bilateral structural network abnormalities in regions belonging to the subcortical and parietal areas. These abnormal regions included the bilateral thalamus and motor areas, as described in the aforementioned propagation model of FBTCS. Therefore, our analysis provides complementary evidence from the diffusion MRI domain in support of the propagation model of FBTCS. In addition, our whole-brain structural network analysis revealed abnormalities in other brain areas, thus suggesting that wider network disruption is present in individuals with FBTCS. Patients without FBTCS also have network disruption, but more localised. Though causality is difficult to infer, it is plausible that the recruitment of recurrent excitation pathways may have reinforced seizure generation and seizure propagation networks, thus leading to widespread abnormality in secondary generalised seizures vs. localised abnormality in focal-only seizures (Tavakol et al., 2019). Hence, we postulate abnormal neuroplasticity as the pathological mechanism underlying FBTCS.

Our novel application of the node abnormality metric allows the mapping of abnormalities on the whole-brain structural network in a patient-specific manner. Our analysis showed structural brain network abnormalities are greater and more widespread in patients with FBTCS. The node abnormality method reconciles the widespread alterations into a single patient-specific metric: the abnormality load that was associated with FBTCS. Although we detected abnormalities in specific regions known to be involved in the pathophysiology of FBTCS, we also found abnormalities outside of those regions. Our results therefore suggest that while thalamocortical pathways, including the regions in subcortical and parietal lobes, are altered in FBTCS and might be important in understanding population-level mechanisms of FBTCS, there may not be any one region that is specific for stratifying patients on FBTCS spectrum. Instead, it is the total number of abnormal regions–a patient-specific property–that is associated with the predisposition to FBTCS.

Our findings have implications for both existing and new treatments. Individual patients have different susceptibility to FBTCS and there is a high clinical value in identifying who is at a higher risk of FBTCS. While identifying mean group differences pertaining to a disease is crucial to develop mechanistic insights, personalised medicine requires quantifying patient-specific heterogeneities (Marquand et al., 2016). Metrics such as, node abnormality

(Sinha et al., 2020), network abnormality (Bonilha et al., 2015), or deviation score (He et al., 2019, 2015) can quantify patient-specific heterogeneities, thus stratifying patients on a spectrum of disease severity rather than dichotomised groups. Multivariate combinations of clinical factors associated with FBTCS (Baud et al., 2015; Bone et al., 2012) with our proposed patient-specific abnormality measure may be able to determine patient susceptibility to FBTCS. Identifying predisposition of patients to FBTCS may be particularly relevant in epilepsy monitoring units where anti-seizure drug tapering carries a risk of FBTCS (Ryvlin et al., 2013). For neuromodulation therapies, regions with high abnormality in a patient might be hypothesised as choke-points for terminating seizures (Paz and Huguenard, 2015). We propose exploring the usefulness of patient-specific abnormality measures for personalised treatment options.

Our findings should be interpreted with some caveats. First, the case-control design of our study could not detangle the cause-effect mechanisms underlying abnormality. Widespread abnormalities in the whole-brain structural network could either be the cause or the effect of FBTCS. A longitudinal study of patients with new-onset epilepsy is best suited to address these questions. Second, we could not study the left TLE and right TLE patients separately with high statistical power due to fewer patients remaining in FBTCS- group. However, to some extent this limitation is mitigated due to the balance between left and right TLE patients in FBTCS+ and FBTCS- groups and partly addressed by our combined ipsilateral-contralateral abnormality analysis (Figure 3.4). Third, we focused only on what makes a patient susceptible to FBTCS and not on which seizure would generalise. The importance of within-patient seizure-variability and seizure-specific treatment has been underscored recently (Schroeder et al., 2020). Identifying features associated with secondary generalisation of seizures is also important (Karthick et al., 2018; Khambhati et al., 2016; Yoo et al., 2014) and a future multimodal analysis combining whole-brain structural and functional networks would allow identification of seizure spreading on abnormal structural network substrates.

In conclusion, we have shown using diffusion MRI that widespread brain network abnormalities are present in patients with FBTCS. Measuring the extent and amount of abnormality on patient-specific whole-brain structural network is a likely indication of patient susceptibility to secondary generalised.

Chapter 4

White-matter abnormalities in idiopathic generalised epilepsy

The data in the following chapter was published in NeuroImage Clinical. Whilst minor adjustments to that article have been made in order to be consistent with this thesis format, the background, methods, results, and conclusions match those of the peer-reviewed article.

Nishant Sinha, Yujiang Wang, Justin Dauwels, Marcus Kaiser, Thomas Thesen, Rob Forsyth, Peter N. Taylor. "Computer modelling of connectivity change suggests epileptogenesis mechanisms in idiopathic generalised epilepsy." *NeuroImage:Clinical*, 2019; 21:101655 doi:10.1016/j.nicl.2019.101655.

4.1 Abstract

Patients with idiopathic generalised epilepsy (IGE) typically have normal conventional magnetic resonance imaging (MRI), hence identifying IGE based on MRI is challenging. Anatomical abnormalities underlying brain dysfunctions in IGE are unclear and their relation to the pathomechanisms of epileptogenesis is poorly understood.

In this study, we applied *connectometry*, an advanced quantitative neuroimaging technique for investigating localised changes in white-matter tissues *in vivo*. Analysing white matter structures of 32 subjects we incorporated our *in vivo* findings in a computational model of seizure dynamics to suggest a plausible mechanism of epileptogenesis.

Patients with IGE have significant bilateral alterations in major white-matter fascicles. In the cingulum, fornix, and superior longitudinal fasciculus, tract integrity is compromised, whereas in specific parts of tracts between thalamus and the precentral gyrus, tract integrity is enhanced in patients. Combining these alterations in a logistic regression model, we computed the decision boundary that discriminated patients and controls. The computational model, informed with the findings on the tract abnormalities, specifically highlighted the importance of enhanced cortico-reticular connections along with impaired cortico-cortical connections in inducing pathological seizure-like dynamics.

We emphasise taking directionality of brain connectivity into consideration towards understanding the pathological mechanisms; this is possible by combining neuroimaging and computational modelling. Our imaging evidence of structural alterations suggest the loss of cortico-cortical and enhancement of cortico-thalamic fibre integrity in IGE. We further suggest that impaired connectivity *from* cortical regions *to* the thalamic reticular nucleus offers a therapeutic target for selectively modifying the brain circuit for reversing the mechanisms leading to epileptogenesis.

4.2 Introduction

Idiopathic generalised epilepsies (IGEs) constitute nearly a third of all epilepsies and can manifest with typical absences, myoclonic seizures, and generalised tonic-clonic seizures, alone or in varying combinations (Berg et al., 2009; Panayiotopoulos, 2005). The “idiopathic” modifier implies an unknown cause in contrast to, for example, epilepsies where an underlying

structural cause is evident. Routine MR imaging is unremarkable. There is strong empirical evidence for heritability (Berg et al., 2009), reflected in the recently proposed change in terminology to genetic generalised epilepsies (Berg et al., 2010). However, the IGE term is still widespread in non-clinical literature and will be used here.

Electrographically, seizures in IGE are characterised by simultaneous bilateral epileptiform discharges. However, on standard MR imaging, patients with IGE appear normal. While more advanced methods have identified some changes, these findings are inconsistent (Duncan, 2005). It has long been suggested that there are shared pathophysiological mechanisms across the spectrum of IGE syndromes (Andermann and Berkovic, 2001; Benbadis, 2005). Therefore, investigation of mixed-syndrome IGE populations is important in identifying shared pathophysiology (Pitkänen et al., 2016; Whelan et al., 2018).

Although there is a paucity of studies on white-matter changes in IGE, some studies have demonstrated regional white matter alterations. In patients with JME, anterior thalamo-cortical radiations to frontal lobe networks have been consistently found abnormal (Deppe et al., 2008; Keller et al., 2011; Liu et al., 2011; O'Muircheartaigh et al., 2012). Additionally, motor networks, along with callosal abnormalities have also been found to be implicated (Gong et al., 2017; O'Muircheartaigh et al., 2011; Vollmar et al., 2012). For patients with GTCs, while Liu et al. 2011 found no aberration in the white-matter, Li et al. 2010 applied multiple analysis techniques and found abnormalities in parts of cerebellum but not elsewhere. However, Zhang et al. 2011 and Liao et al. 2013 detected abnormalities in the non-cerebellar regions by applying graph theory and found altered node topological characteristics in default mode network, mesial frontal cortex and in subcortical structures. Combining functional and structural connectivity, Zhang et al. 2011 demonstrated loss in structure-function coupling and epilepsy duration. Ji et al. 2014 found subtle reduction in lengths of commissural tract bundles connecting the anterior cingulate cortex and the cuneus bilaterally, which were also found to have altered functional connectivity. In childhood absence epilepsy (CAE), white-matter has been shown to be impaired by analysing specific structures (Luo et al., 2011; Yang et al., 2012) and also by applying network-based graph theoretical measures (Xue et al., 2014). Furthermore, Qiu et al. 2016 found impairments in default mode network regions. In mixed syndrome IGE, aberrant increases in thalamic, precentral, and parietal areas have been shown (Groppa et al., 2012) in addition to differences in callosal and cortico-spinal tracts amongst others (Focke et al., 2013). On the other hand, McGill et al. 2014 found no structural difference in patients with IGE. In summary, the existing white matter findings

vary widely between studies, possibly due to different methods applied for detecting complex patterns of microstructural alterations.

Diffusion MRI Connectometry is a recently developed analytical method that is more sensitive to local structural differences in fibre pathways (Yeh et al., 2016, 2013a). This is fundamentally different from conventional whole-tract based approaches where end-to-end tracking between different regions is performed first and then differences in connectivity sought. A summary measure derived for the entire track may obscure localised pathological changes (Keller et al., 2016; Yeh et al., 2016). In contrast, connectometry first maps the difference in a parameter of interest at each fibre orientation in a voxel. It then connects the differences using fibre tracking, thus delineating an entire altered pathway (Abhinav et al., 2014b). The exact location and extent of the abnormality can be detected with high specificity. Connectometry has been applied in a number of studies investigating structural alterations such as in chronic stroke, amyotrophic lateral sclerosis, depression amongst others (Abhinav et al., 2014a; Yeh et al., 2013a). However, to our knowledge, connectometry has not been applied to examine white-matter changes in IGE.

Beyond the analysis of static properties of brain connectivity, computational models additionally allow the prediction of time-varying activity (Baier et al., 2012; Lytton, 2008). Models simulate time series of cerebral activity, constrained by model parameters. In recent years, models constrained with parameters derived from clinical data have provided mechanistic insights into the pathophysiology of seizure genesis, maintenance, spread, and termination (e.g., Bauer et al. 2017; Jirsa et al. 2016; Kramer et al. 2012; Proix et al. 2017; Sinha et al. 2016). In the context of spike-wave seizures, models of thalamocortical interactions have been proposed (Breakspear et al., 2006; Destexhe, 1998; Marten et al., 2009; Robinson et al., 2002; Taylor et al., 2014b). However, it is only recently that models of IGE have been constrained by subject-specific data (Benjamin et al., 2012; Nevado-Holgado et al., 2012; Schmidt et al., 2014, 2016; Taylor et al., 2013a; Yan and Li, 2012)). Combining a dynamical model with subject-specific neuroimaging data permits exploration of possible mechanistic consequences of observed connectivity change (Proix et al., 2017; Taylor et al., 2014a).

The focus of this study is to elucidate white matter changes that are common to mixed-syndrome IGE, using diffusion MRI Connectometry, a potentially more sensitive method. We then explored possible mechanistic consequences of the connectivity changes in a computational dynamic model, constrained by our neuroimaging observations.

4.3 Methods

4.3.1 Participants

We studied a total of 32 subjects recruited by the New York University Comprehensive Epilepsy Centre. Our subject cohort included 14 patients with IGE (7 males and 7 females, age range 20.6-49.6 years, mean age 34 years). Patients were age and gender matched with 18 healthy control subjects (9 males and 9 females, age range 20.9-46.5 years, mean age 30.2 years). Details of functional connectivity change in this cohort have been previously reported (McGill et al., 2012, 2014). The details of patients are provided in Table 4.1 and information on control subjects is in Appendix C.6. Patients met the criteria for IGE and had no history of developmental delay or structural brain abnormalities. Standard diagnostic anatomical imaging studies were normal. Electrophysiological evaluation with interictal, and in most cases, ictal EEG demonstrated typical generalised epileptiform spikes. Patients with focal epileptiform discharges or focal slowing on EEG were excluded (McGill et al., 2012, 2014). Patients with IGE were classified according to the International League Against Epilepsy (ILAE) classification as having absence seizures (35.7%), myoclonic seizures (50%), generalised tonic-clonic seizures (85%), or combinations thereof as shown in Table 4.1. All people diagnosed with IGE were receiving active medical treatment at the time of study. All subjects gave their written informed consent to participate in this study, which was approved by the Institutional Review Board of NYU Langone School of Medicine.

4.3.2 Data acquisition and processing

All 32 subjects underwent scanning on a Siemens Allegra 3.0T scanner at New York University Centre for Brain Imaging. Participants had a T1-weighted MRI sequence optimised for grey-white matter contrast (TR $=$ 2530 ms, TE $=$ 3.25 ms, T1 $=$ 1100 ms, flip angle $= 7^{\circ}$, field of view (FOV) $=$ 256 mm, matrix $= 256 \times 256 \times 192$, voxel size $= 1 \times 1.33 \times 1.33$ mm). Images were corrected for non-linear warping caused by non-uniform fields created by the gradient coils. All participants also had diffusion MRI scans. Diffusion-weighted echo-planar MRI were acquired by applying diffusion gradients along 64 directions (b-value = 1000 s/mm^2) with the following parameters during the 6 min 3s scan (TR $=$ 5500 ms, TE $=$ 86 ms, FOV $=$ 240 mm, slice thickness $=$ 2.5 mm, voxel size $= 2.5 \times 2.5 \times 2.5$ mm). Diffusion data were corrected for eddy current and motion artefacts using the FSL eddy

Table 4.1 Patient information and seizure types

	Demographics				Seizure types		
Patient	Gender	Age	Epilepsy duration	Onset Age	Absence	Myoclonic	GTC
1	M	49.6	30.6	19		×	
2	F	48.7	31.7	17	×	×	×
3	M	47.4	31.4	16			×
4	M	27.5	7.7	19.8		×	
5	F	32.1	12.1	20			×
6	F	21.7	3.6	18.1	×		×
7	F	38.8	26.8	12		×	×
8	M	27.7	26.2	1.5			×
9	M	35.6	26.6	9	×		×
10	M	36.3	5.3	31			×
11	F	24.6	9.6	15	×	×	×
12	M	20.6	5.6	15			×
13	F	37.9	23.9	14		×	×
14	F	27.6	17.8	9.8	×	×	×

correct tool (Andersson and Sotiropoulos, 2016). We then rotated the *b* vectors using the 'fdt-rotate-bvecs' tool (Jenkinson et al., 2012; Leemans and Jones, 2009).

4.3.3 Diffusion weighted imaging analysis

Tractography

We analysed the data obtained from eddy corrected diffusion-weighted MRI and T1-weighted MRI in the DSI Studio (http://dsi-studio.labsolver.org) software pipeline. The diffusion data were reconstructed in standard space using q-space diffeomorphic reconstruction (QSDR) (Yeh and Tseng, 2011) to obtain the spin distribution function (SDF) (Yeh et al., 2010). The diffusion sampling length ratio was 1.25 and the QSDR reconstruction yields maps of SDFs at 2 mm isotropic resolution. We applied an 8-fold orientation distribution function (ODF) tessellation with 5 peaks of the ODF, allowing for crossing fibers within voxels. For fibre tracking, we seeded the regions and the tracts were terminated when the quantitative anisotropy of the voxel through which the streamline entered was below 0.6*(Otsu's threshold). Otsu's threshold is calculated to give the optimal separation threshold that maximises the variance between background and foreground (Otsu, 1979). We choose deterministic tractography due to the likelihood of it generating fewer false positive connections than

probabilistic approaches. Streamlines with implausible lengths (> 300 mm and < 10 mm) and extreme turning angles (> 60 degrees) were excluded. Other parameters were as follows: step size: 1 mm, smoothing: 0, seed orientation: primary, seed position: subvoxel, randomise seeding: 0, direction interpolation: trilinear, tracking algorithm: runge-kutta order 4, streamlines threshold: 1,000,000. We assessed the integrity of tracts by analysing the generalised fractional anisotropy of the tract profiles. The gFA measure is a generalised version of the widely used FA measure of white matter integrity (Tuch, 2004).

Connectometry

We investigated the structural alterations in white matter pathways using diffusion MRI connectometry to compare patient and control groups (Yeh et al., 2016). Connectometry permits analysis of the white-matter characteristics locally in contrast to the conventional end-to-end, whole-tract approaches. It has been shown that when the structural change involves only a segment of the white-matter pathways, global connectivity and tractography based approaches have a much lower sensitivity in capturing the regional variability in the white matter as compared to connectometry (Faraji et al., 2015; Yeh et al., 2016, 2013a). The overall procedure of the connectometry analysis is illustrated in Figure 4.1.

First, we created a connectometry database of all 32 subjects (14 patients and 18 controls) with generalised fractional anisotropy (gFA) as the index of interest (Figure 4.1(a,b)). In creating the connectometry database we used the default Human Connectome Project HCP842 atlas as the common atlas from which the local fibre directions are sampled to create the local connectome matrix. To aid reproducibility, we provide an anonymised version of the Connectometry database we used in this study on https://doi.org/10.5281/zenodo.2535418.

Second, we set-up the group connectometry analysis in DSI studio to correlate the local connectome matrix with age, gender, and subject category (patient or control) in a multiple linear regression model while selecting the subject category as the study variable. In this step, we also assigned a seed region to study the regional differences of the local connectomes emanating from that region (Figure 4.1(c)). Specifically, we seeded (i) the whole brain to visualise the consistent trend of connectome alterations, (ii) all regions defined in the JHU white-matter atlas excluding the regions in cerebellum and brain-stem, and (iii) corpus callosum and thalamic regions from the freesurfer Destrieux atlas. All the regions studied along with their anatomical locations are shown in Appendix C.1 and C.2.

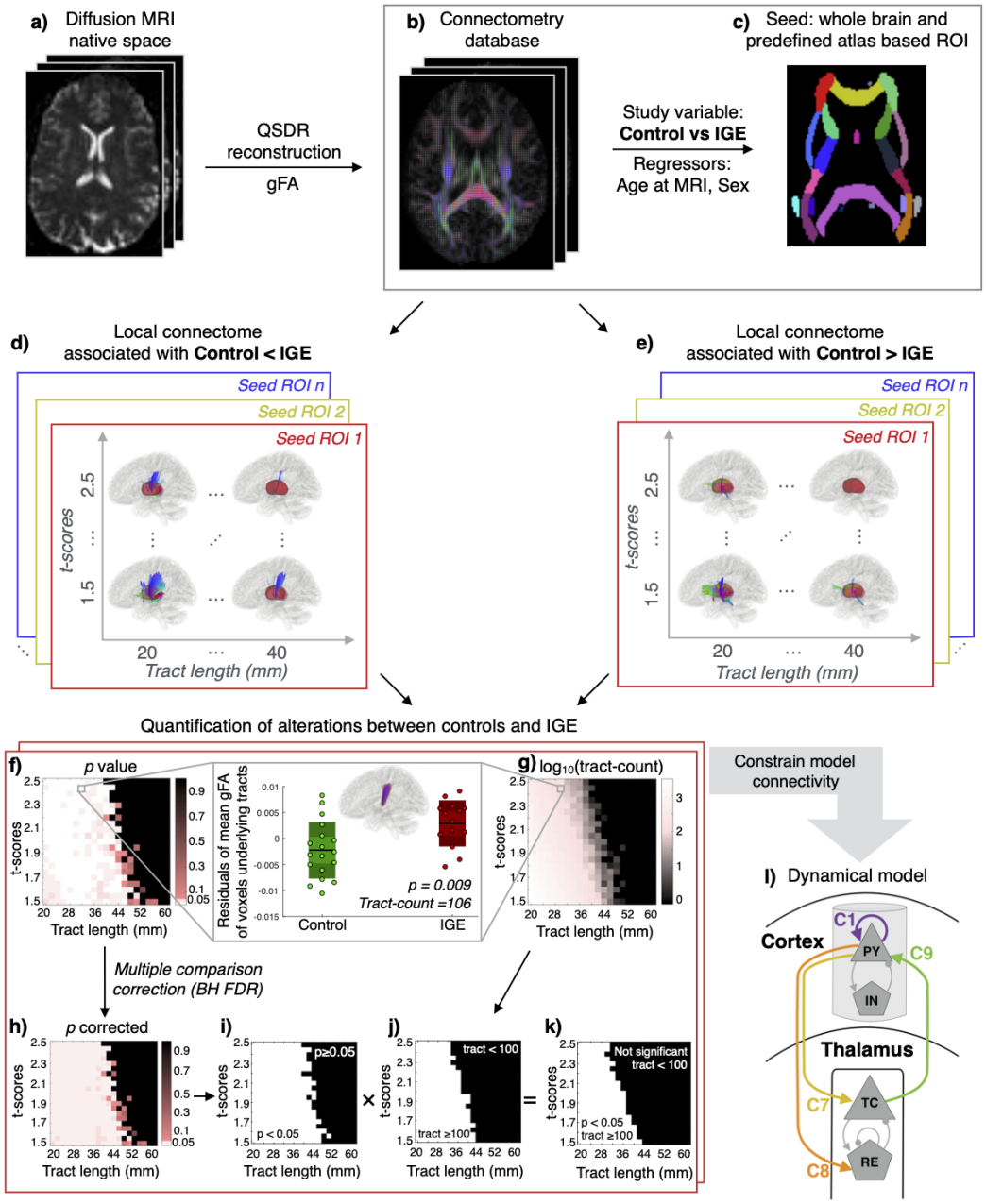

Fig. 4.1 **Overall procedure.** **(a-b)** Diffusion MRI of each subject in the native space was reconstructed to the standard space for creating a connectometry database using QSDR reconstruction with gFA as the index of interest. **(c)** Group connectometry analysis was performed to study the local alterations in the white-matter tracts between controls and IGE patients using a multiple regression model with age at MRI acquisition and sex as covariates. Local connectome differences were studied for the whole brain seeding and seeding predefined atlas based regions. (continued)

Fig. 4.1 **(d-e)** For each seeded region of interest (ROI), connectometry was performed for a wide range of tract lengths and *t*-thresholds as represented by the two-dimensional space. At each point of the two-dimensional space, the local connectomes associated with the reduction and increase in IGE were delineated. **(f-g)** Output of connectometry were quantified by computing the significant mean gFA differences defined by the *p*-value between the groups and the tract count. **(h)** *p*-values were corrected for multiple comparisons using Benjamini-Hochberg FDR and a binary threshold was applied at 0.05 in **(i)**. Similarly, on the tract count matrix, a binary threshold of 100 was applied to obtain a matrix shown in **(j)**. The matrices in **(i)** and **(j)** were multiplied at each point to result in a two-dimensional space in **(k)** that highlights a region (in white) where the difference between the groups are significant with a minimum of 100 tracts detected. **(l)** Schematic of the thalamo-cortical model. Tract alterations from the imaging data were incorporated in the model to constrain the thalamo-cortical (C7, C8, C9) and cortico-cortical (C1) connectivity parameters.

Third, we ran connectometry analysis for tract length threshold varying from 20*mm* to 60*mm* in increments of 2*mm* (voxel resolution) and *t*-score threshold varying from 1.5 to 2.5 in increments of 0.05. Connectometry analysis allows selecting the affected tracts with length greater than a threshold, which is termed as the length threshold. *t*-score is another threshold at which the tracts, compared between the two groups, would be detected as altered. At each point on this two dimensional grid, local connectomes for every seed region under study are delineated with positive and negative associations of gFA and the subject category (Figure 4.1(d,e)). The local connectomes were tracked using a deterministic fibre tracking algorithm (Yeh et al., 2013a), track trimming was iterated once, and the seed count was set to 10000. These are the default settings for fibre tracking in connectometry analysis from the 9 August 2018 version of DSI Studio. Connectometry analysis controls for the true positive and false positive rate by comparing the positive and negative associations of gFA with a null distribution by randomly permuting the group labels. Further details of this procedure can be referred in the section on "Local connectomes and their statistical inference" in (Yeh et al., 2016) and also in the method section of (Yeh et al., 2013a). In our study, we set the permutation count to 1500 which is reasonably high and a pragmatic choice for speed.

Fourth, we quantified the output of the connectometry analysis at each point of the two-dimensional grid for every seeded region of interest. We computed the mean gFA of the voxels traversed by the altered tracts detected from the connectometry analysis for each subject. These mean gFA values were exported in MATLAB and effects of age and gender were regressed out to compute the residuals. The residual gFA were compared between the patient and the control groups by applying a non-parametric Wilcoxon rank sum test (Figure

4.1(f)). We corrected the p-values for multiple comparison by applying Benjamini-Hochberg false discovery rate procedure at 5% significance level (Figure 4.1(h)) and then applied a binary threshold at $p = 0.05$ (Figure 4.1(i)). Identifying bundles of adjacent, altered, streamlines is also important in avoiding Type-I errors. Therefore, we noted the number of streamlines detected at each point of the two-dimensional grid (Figure 4.1(g)). An arbitrary binary threshold of $n = 100$ was applied to visualise the range of tract length and t-score values for which the connectometry analysis identified at least 100 streamlines as aberrant (Figure 4.1(j)). This binary matrix was multiplied element-wise with the binary matrix generated from the FDR corrected p-values (Figure 4.1(k)). Thus, we determined a range of tract lengths and t-scores where there exist significant microstructural alterations in at least 100 tract bundles for each seeded region.

4.3.4 Dynamical model

Model description

To investigate how aberrations in connectivity may lead to seizure dynamics, we related our data-driven neuroimaging findings to an established mathematical model which simulates dynamic thalamocortical interactions. The model is illustrated schematically in Figure 4.1(l). This neural population model is based on the Wilson-Cowan formalism (Wilson and Cowan, 1972) which is one of the best-studied population level models (see e.g., Borisyuk et al. 1995; Destexhe and Sejnowski 2009; Meijer et al. 2015; Wang et al. 2012).

In this neural population model, the cortex is treated as one subsystem and the thalamus as the other. The cortical subsystem is composed of excitatory pyramidal (PY) and inhibitory interneuron (IN) populations. The thalamic subsystem includes variables representing populations of thalamo-cortical relay cells (TC) and neurons located in the reticular nucleus (RE). The connection schemes, shown by the arrows in Figure 4.4(b) between various cell populations, have the following interpretation: the PY variable is self-excitatory and also excites the IN population. In addition, PY excites the TC and RE cells of thalamus. IN inhibits local cortical PY cells only. Direct thalamic output to the cortex comes only from the excitatory TC populations to the PY populations. Intra-thalamic connectivity is incorporated as the TC cells having excitatory projections to RE, which in turn inhibit the TC population along with self-inhibition of RE. The dynamics of the model are governed by the following differential equations inspired by the model in Taylor et al. 2014b:

$$\tau_1 \frac{dPY}{dt} = -PY + S(C_1 PY - C_3 IN + C_9 TC + h_{py}) \tag{4.1}$$

$$\tau_2 \frac{dIN}{dt} = -IN + S(C_2 PY + h_{in}) \tag{4.2}$$

$$\tau_3 \frac{dTC}{dt} = -TC + C_7 PY - C_6 RE + h_{tc} + \alpha N(t) \tag{4.3}$$

$$\tau_4 \frac{dRE}{dt} = -RE + C_8 PY - C_4 RE + C_5 TC + h_{re} \tag{4.4}$$

where $h_{py,in,tc,re}$ are external input parameters which can be interpreted as the general excitability level, as they determine how much input is required to activate a population (Amari, 1977; Wilson and Cowan, 1972). $\tau_{1,\cdots,4}$ are time scale parameters, $C_{1,2,\cdots,9}$ are connectivity parameters between the cortical and thalamic subsystems, $N(t)$ is normally distributed noise input with zero mean and unit standard deviation; α modulates the noise amplitude. The noise term was added to the TC population following previous modelling literature of the thalamo-cortical loop, and represents non-specific ascending noise input from the brain stem (Breakspear et al., 2006; Marten et al., 2009; Robinson et al., 2002; Taylor et al., 2014b). The formalism for the noise term used here is adopted in (Wang et al., 2014, 2017). $S[\cdot]$ is the sigmoid activation function defined as follows:

$$S[x] = \frac{1}{(1 + \exp(-a(x - \theta)))} \tag{4.5}$$

where, $a = 1$ is the steepness of the sigmoid function, and $\theta = 4$ is the x offset (Wang et al., 2012, 2014).

We simulated the model numerically in MATLAB (The MathWorks, Natick, MA). We computed the solutions of the deterministic model (i.e., noise term $N(t)$ in equation 4.3 is set to zero) by using the ode45 solver. For the stochastic model, in which the noise term is included to simulate seizure transitions, we implemented the equations as a stochastic differential equation, and used the Euler-Maruyama solver with step size $\delta = (1/15000)s$. Tutorials and MATLAB codes for numerically simulating SDEs are explained in (Higham, 2001). The simulated EEG dynamics in the model correspond to the activity of PY after filtering out the DC component with a high pass filter at 1 Hz (see, Jirsa et al. 2014; Wang et al. 2017).

Model parameter selection using phase space approach

We reconstructed a regime where the spike-wave attractor was bistable to the fixed point by understanding the bifurcation structure of our model using a phase space approach. This was done through the reconstruction of subsystems which, when operating on different timescales can be combined (Fenichel, 1979; Jirsa et al., 2014; Wang et al., 2012). The parameter values incorporated in the model are provided in Appendix C.7. Their choice was guided by previous works that highlighted the necessary bifurcation structures (Taylor et al., 2014b; Wang et al., 2012). Briefly, the state space is deconstructed into slow and fast dimensions and treated independently at first. The two-dimensional fast cortical system is placed near a bistability between limit cycle and stable fixed point. For such a bistability to occur in a two-dimensional system, only a limited number of bifurcation structures exist. These possible bifurcations in two dimensions in the Wilson-Cowan model have been characterised extensively (see e.g., Borisyuk et al. 1995; Borisyuk and Kirillov 1992). Thus, the parameters for the fast subsystem are limited to a sub-region in the parameter space; this is the region we choose for our model.

When coupling the slow subsystem to the cortical fast subsystem, it is known from established previous work on bursting that the slow manifolds need to intersect the bifurcation structure of the fast manifolds. This must occur within the geometric constraints to create spike-wave type waveforms as a limit cycle attractor (see, Wang et al. 2012 for details). Essentially, bursting-type waveforms are created with one spike, which is the limit cycle in the fast subsystem, and one slow wave, which is the bistable fixed point in the fast subsystem. The geometric construction thereof is described in the classic textbook[1] (Izhikevich, 2006) in chapter 9.2 and 9.3. Thus, even for the slow subsystem, the parameters allowing for spike-wave waveforms are restricted to a sub-region in the parameter space.

In essence this can be considered as a type of model selection/inference. It should be noted that this does not necessarily represent the infinite dimensional space of all possible models and parameters thereof. Instead, we use our model as a tool for explaining current data and making predictions of unknown data (i.e., the directionality of the connectivity which is unknown from the diffusion MRI). N.B. in the infinite dimensional space of all other models, there may exist others that were not selected by our approach but can explain the data. Hence our modelling approach serves as a *suggestion* of a *plausible* mechanism, rather than serving as a definitive proof of a mechanism and should be interpreted as such.

[1] https://www.izhikevich.org/publications/dsn.pdf

4.3.5 Discriminatory decision boundary

We used a logistic regression model to infer a linear decision boundary that optimally discriminates IGE patients and controls. Recognising the two different patterns of alterations, i.e., *decreases* in cortico-cortical tracts and *increases* in thalamo-cortical tracts, we chose to derive two features from our data. Specifically, we considered the mean gFA of voxels traversed by the abnormal thalamo-cortical tracts as one feature. Similarly, we incorporated the mean gFA of all the voxels underlying the abnormal cortico-cortical tracts as the second feature. Age and gender were regressed out from both the features using a multiple linear regression model. Therefore, our feature space can be represented as $A \in \mathbb{R}^{n \times m}$, where $m = 2$ indicates the total number of features and $n = 32$ denotes the total number of subjects in our study.

The linear decision boundary between IGE patients and controls was determined using a logistic regression model by minimising the following regularised objective function:

$$\min_{x} \sum_{i=1}^{n} \log(1 + e^{(-y_i(x^T a_i + c))}) + \frac{\rho}{2}\|x\|_2^2 \tag{4.6}$$

where, $y = (y_1, y_2, \cdots, y_n)$ is the n dimensional vector representing the two groups (0 for healthy subjects and 1 for patients with IGE); ${a_i}^T$ denotes the i-th row of feature space $A \in \mathbb{R}^{n \times m}$; c is the scalar intercept; and $\frac{\rho}{2}\|x\|_2^2$ is the l_2 (ridge) regularisation term. We optimized the cost function 4.6 by applying stochastic gradient descent algorithm as implemented in the *fitclinear* method in MATLAB in which ρ is set to $1/n$. Optimising the cost function in equation 4.6 with the entire data, we computed the discriminatory decision boundary between patients and controls.

4.3.6 Statistical analysis and visualisation

We applied the non-parametric Wilcoxon rank sum test for comparing the white matter differences between the patients and controls. We corrected for multiple comparisons by applying Benjamini-Hochberg false discovery rate correction at a significance level of 5% (Benjamini and Hochberg, 1995). Results were declared significant at $p < 0.05$. To illustrate the anatomical location of the observed differences in the white matter tracts, we reconstructed the section-wise t-score plots. Cohen's d measures the standardised difference between two means (Cohen, 1988). Therefore, we computed the Cohen's d-score to measure

the effect size of alteration of white matter differences between the patient and control groups. We created the scatter plots using the UniVarScatter function in MATLAB (https://github.com/GRousselet/matlab_visualisation).

4.4 Results

Our results are presented in three main sections. First, we demonstrate *microstructural* connectivity alterations in the white matter tracts of the default mode network (DMN), complementing previous demonstrations of DMN resting-state fMRI *functional* connectivity alterations in the same subjects (McGill et al., 2012, 2014). Second, we illustrate the white matter aberrations found in patients after analysing the entire white-matter structures of the two groups. Finally, we demonstrate how alterations in connectivity affect IGE seizure dynamics in the computational model.

4.4.1 Microstructural changes in the default mode network

Recent studies have highlighted that anatomical connectivity between brain regions underpins functional connectivity (Chu et al., 2014; Honey et al., 2009). Impaired functional connectivity in the default mode network has been shown previously by (McGill et al., 2012) for the same idiopathic generalised epilepsy patients as in our study. Specifically, (McGill et al., 2012) demonstrated that with the seed placed in the posterior cingulate cortex (PCC), its functional connectivity to the ventral part of the medial prefrontal cortex (MPFC) is reduced in IGE patients (results reproduced in Figure 4.2(a)). These regions are located within the PCC and MPFC, two of the prominent nodes of the default mode network. Previous studies have identified the cingulum tracts as the only direct anatomical connection between these two regions of the default mode network (see, Table 1 in Heuvel et al. 2009). Here, we investigate if the demonstrated alterations in functional connectivity have a basis in the corresponding altered structural connectivity.

First, we delineated all the cingulum tracts connecting PCC and MPFC by performing conventional end-to-end tractography. These tracts are shown in Figure 4.2(b). Next, for detecting any partial abnormalities in these tracts, we performed connectometry by setting the cingulum region from the JHU white-matter atlas as seed. The tract profile of cingulum fibres are colour coded in accordance with their t-scores that quantifies how different the tracts are with respect to controls. Across a wide range of t-score and tract length thresholds, we found that in IGE patients there is a significant loss of tract integrity in segments of the cingulum tracts. In Figure 4.2(b), we have shown these alterations at a representative t-threshold of $t = 1.94$ and length threshold of $l = 30mm$. Significant reduction at these thresholds are

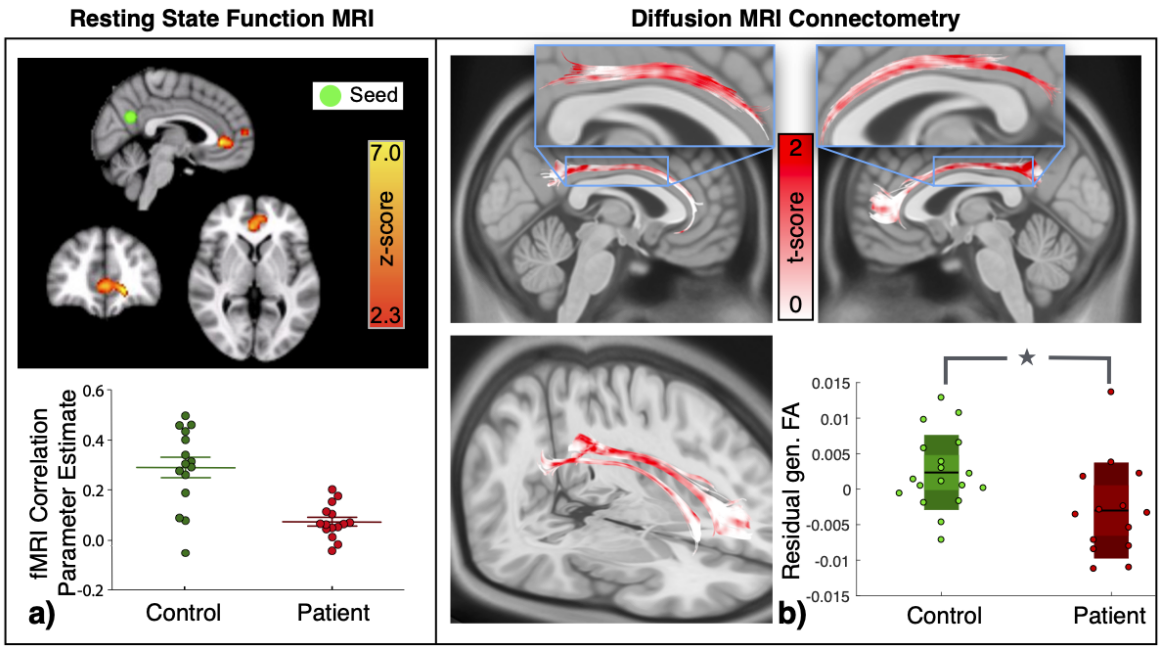

Fig. 4.2 **Microstructural white matter alterations in default mode network detected from connectometry analysis correspond to functional alterations.** **a)** Functional connectivity between posterior cingulate cortex (PCC) and ventral part of medial prefrontal cortex (MPFC) has been shown to be reduced in patients with IGE (figure modified from (McGill et al., 2012)). Functional MRI correlation parameter estimates were obtained using a general linear model after controlling for the effects of covariates on fMRI correlation. z-score represents the threshold at which the difference between the groups were examined by direct voxel-wise comparison using a mixed-effects ordinary least square model. **b)** The underlying cingulum tracts between PCC and MPFC obtained from tractography between these regions are shown. Implementing Connectometry analysis elucidates regional differences in gFA between the two groups along the tract profile which are colour coded in accordance with their t-score. Red represents the tract segments that are maximally reduced in patients whereas white illustrates the segments that are not different. The specific portion of cingulum tracts which are aberrant are magnified in the inset figures. The box plot depicts that the residuals of mean gFA associated with the aforementioned aberrant portion of cingulum tracts is significantly reduced ($p = 0.01, d = 0.90$) in patients compared to controls.

quantified in the corresponding box plot ($p = 0.01, d = 0.90$) in Figure 4.2(b). Consistent replication of this trend across a wide range of tract length and t-score thresholds is illustrated in Appendix C.1(a). These results give an indication that the loss of white-matter integrity in the cingulum tracts demonstrated here might be a plausible basis for the reduced functional connectivity between the regions connected by it (i.e., PCC and ventral MPFC in (McGill et al., 2012)).

Note that the application of conventional whole-tract based approach in which summary statistics is derived by averaging gFA across the entire tract profile (i.e., ignoring partial abnormalities), failed to detect any significant difference as illustrated in Appendix C.5. As expected, this is mainly because the partial abnormalities of the cingulum tracts are eclipsed by the normal segments (shown in white in Figure 4.2(b)).

4.4.2 White matter structures with altered connectivity

We identified four pairs of structural connections that were consistently altered between patients and controls across a large range of t-score and tract length thresholds (Figure 4.3(c)). The cingulum tract aberrations discussed in the previous section are shown again in Figure 4.3 alongside other white-matter abnormalities detected. Apart from cingulum tracts, we also found that the integrity of the white matter tracts in the column and body of fornix was significantly compromised in patients. Tracts from fornix detected at an illustrative threshold of $t = 1.94$ and length $= 30mm$ from connectometry analysis are shown in Figure 4.3(a). As depicted by the box plot in Figure 4.3(b), gFA residuals averaged across the tract and compared between the two groups is significantly reduced ($p = 0.02, d = 0.87$) in IGE patients.

Similarly, we detected substantial microstructural abnormality in the white matter segments of the bilateral superior longitudinal fasciculus. We found that the fibre integrity of superior longitudinal fasciculus was compromised in patients with IGE for a wide range of thresholds. In Figure 4.3(a), we plot the abnormal segments of superior longitudinal fasciculus at exemplary threshold values of $t = 1.94$ and length $= 30mm$. Significant reduction of mean gFA across the tract in these segments for IGE patients at $p = 0.002$ and $d = 1.34$ are shown in the box plot in Figure 4.3(b).

In contrast, we found that the white matter tracts forming part of the bilateral cortico-thalamic radiations between the thalamus and the precentral gyrus, have an enhanced structural integrity in patients with IGE. This was evident from the connectometry analysis where these tracts showed an increased gFA association in IGE patients across a wide range of t-score and tract length thresholds. In Figure 4.3(a), these tracts are plotted at an illustrative threshold value of $t = 1.94$ and length $= 30mm$. Aberrant increase of gFA associated with these thalamo-cortical radiations are quantified in the box plot (Figure 4.3(b)) at $p = 0.005$

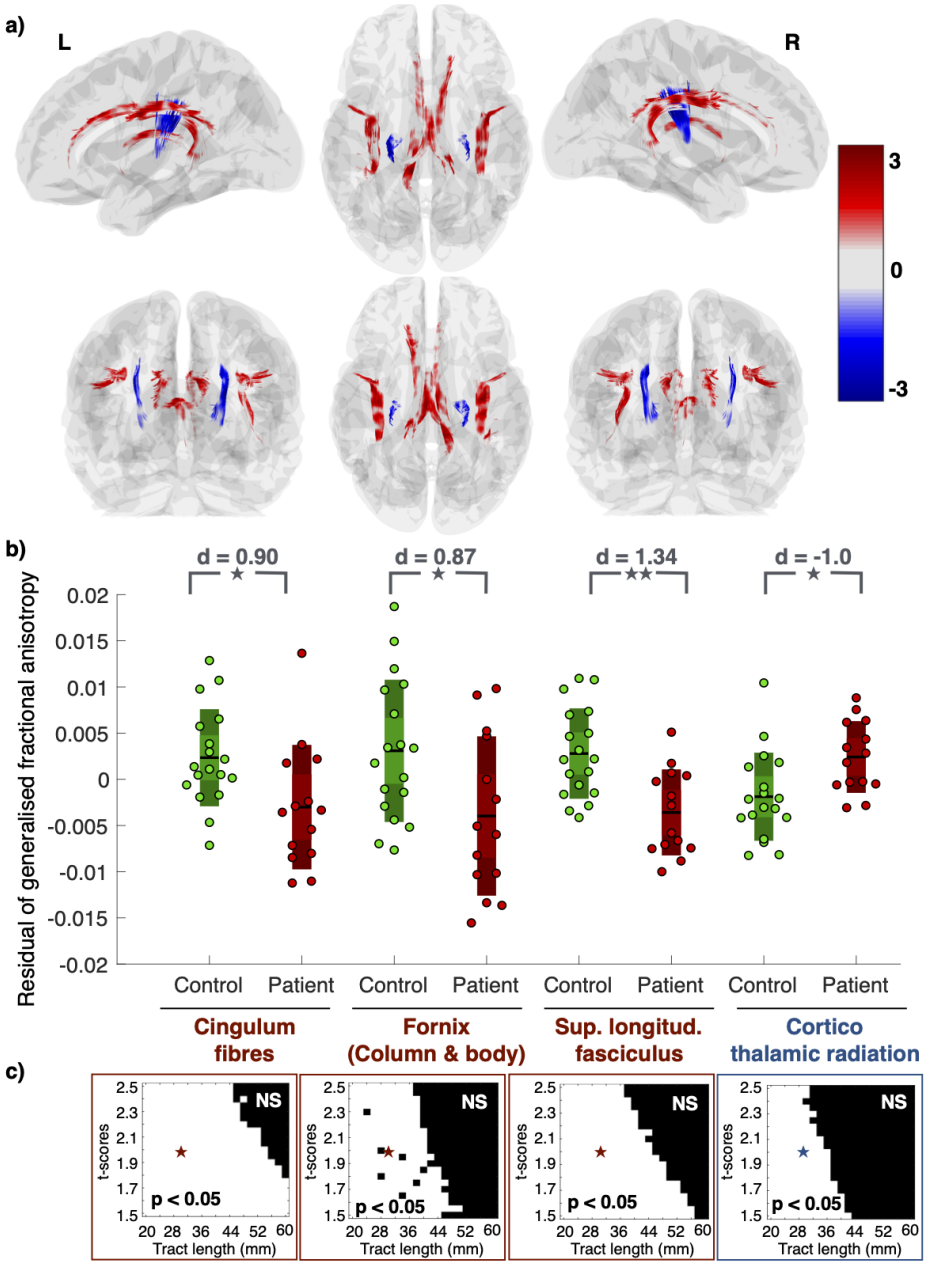

Fig. 4.3 **Alterations in generalised fractional anisotropy in white matter tracts. a)** gFA associated with the white matter tracts in bilateral cingulum, column and body of fornix, superior longitudinal fasciculus, and the parts of cortico-thalamic radiations terminating in the precentral gyrus are aberrant for a wide range of thresholds in connectometry analysis. These tracts are shown overlaid on the brain schematic in different views. Tracts are colour coded in accordance with their *t*-scores where the warmer colour for higher positive *t*-score indicates a reduced gFA in patients and the cooler colour for lower negative *t*-score indicates increased gFA associated with the tracts in patients compared to controls. (continued)

Fig. 4.3 **b)** The comparison of mean gFA across the tracts between patients and controls for each aberrant region is shown in the box plot. The p-value for each region is indicated by stars in grey (double star for $p < 0.005$ and single star for $0.005 < p < 0.05$) along with the effect sizes (d-scores). **c)** The white region in the two dimensional panels depict the threshold values for which the micro-structural alterations are significantly different in connectometry analysis. Stars in red/blue represent exemplary threshold values of $t = 1.94$ and tract length $= 30mm$ at which the results are shown in **a)** and **b)**.

and $d = -1.0$ by comparing the mean gFA underlying these tracts between IGE patients and controls.

In summary, we have demonstrated that the tracts in bilateral cingulum, fornix, and superior longitudinal fasciculus have reduced gFA, but parts of bilateral thalamo-cortical radiations have increased gFA in patients. This pattern of reduced structural integrity in cortico-cortical connections and enhanced structural integrity in thalamo-cortical connections was confirmed upon analysing each white matter region of the JHU atlas and a few other ROIs (for completeness) from Destrieux atlas which are illustrated in Appendix C.1. Visually also this pattern of alteration is evident from seeding the whole-brain in connectomery analysis illustrated in Appendix C.2. Taken together, our findings suggest that in idiopathic generalised epilepsy, there is a trend towards a loss of white-matter integrity in cortico-cortical connections, whereas thalamo-cortical connections tend to be abnormally enhanced. In Figure 4.4(a), we show the optimal decision boundary for discriminating patients and controls. Note that the patients (controls) with increased (decreased) fibre integrity in cortico-thalamic tracts and decreased (increased) fibre integrity in cortico-cortical tracts are above (below) the positively-sloped decision boundary. We incorporate this information to inform the analysis of the dynamical model in section 4.4.3.

4.4.3 Epileptogenesis mechanisms due to connectivity alterations

Diffusion MRI can tell us which tracts are aberrant in patients, however, it does not tell us their direction, or how this may lead to epileptogenesis mechanistically. We therefore incorporate the structural white-matter connectivity changes demonstrated in the previous section into a dynamical model to examine whether such changes could contribute to epileptogenesis.

Model dynamics

We implemented a neural population model with cortical and thalamic subsystems illustrated in Figure 4.4(b) to investigate the mechanisms of seizures due to connectivity alterations. We are specifically interested in the four parameters of this model which reflect our neuroimaging findings: (i) cortico-cortical (PY→PY) connectivity C1, (ii) cortico-thalamic relay nuclei (PY→TC) connectivity C7, (iii) cortico-reticular (PY→RE) connectivity C8, and (iv) thalamo-cortical (TC→PY) connectivity C9. These parameters are highlighted in Figure 4.4(b).

In Figure 4.4(c), we have charted the model dynamics for variations in cortico-cortical parameter (C1) with respect to cortico-thalamic parameters (C7, C8, and C9). In the blue regime of the parameter space, the system resides in the background state of fixed point dynamics. This represents seizure free activity, similar to most models (Breakspear et al., 2006; Jirsa et al., 2014; Sinha et al., 2016; Wang et al., 2012). In the orange regime, however, the model exhibits spike-wave dynamics. Spike-wave discharges are typically noted as the clinical marker of pathological seizure activity in many types of IGE syndrome. Therefore, the orange regime of the parameter space represents the pathological region where seizures would ensue. In addition, the model is also capable of producing monostable fast oscillatory dynamics in the region of 20-30 Hz (grey regions), which could represent additional seizure patterns (Wang et al., 2012, 2017). For the purpose of this study, we consider both the orange and grey region to be epileptogenic. Note that we do not assume a specific dynamic mechanism by which seizures occur (i.e., if the seizure occurs due to some slow parameter change; or due to spontaneous noise-driven transitions, which are possible in bistable states (Baier et al., 2012; Silva et al., 2003; Wang et al., 2014)). Rather we only wish to highlight parameter regions that can support seizure dynamics in principle (in other words, where a seizure attractor exists or co-exits). Our model also features a bistable region, where fixed-point and SWD attractors coexist (Appendix C.4), thus we are not excluding any particular mechanism of ictogenesis. In our modelling framework, connectivity parameters for patients would assume a value such that the dynamics are placed in the epileptogenic (orange, grey) region where seizures occur whereas, the connectivity parameter for controls will be in seizure free (blue) region. Nonetheless, we have shown the subdivisions of the parameter space with exact dynamics in the bifurcation plot, capturing the minima and maxima of simulated time-series for representative parameter values in Appendix C.4.

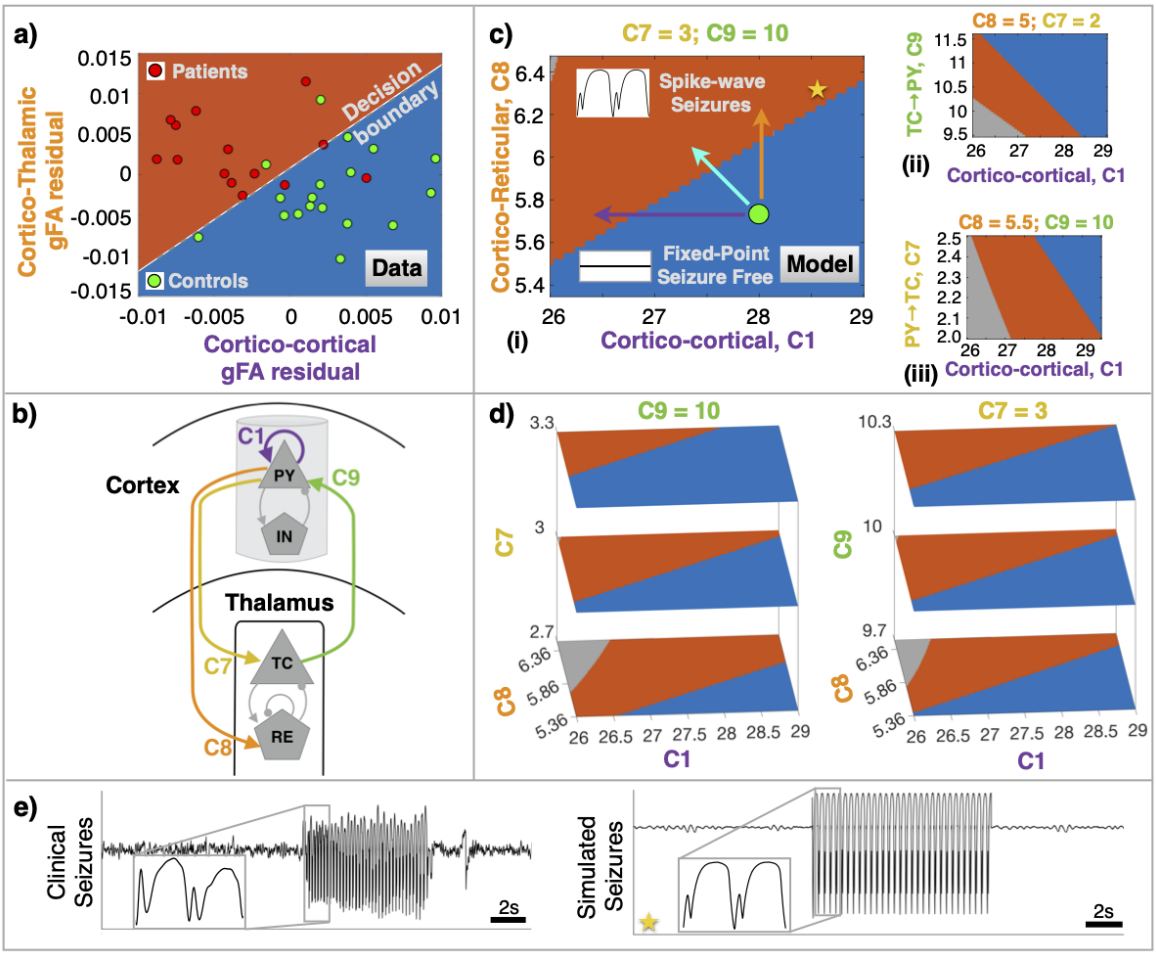

Fig. 4.4 **Computational model combined with neuroimaging analysis predicts potential mechanism of epilepsy manifestation. a)** Discriminatory decision boundary between patients and controls inferred from a logistic regression model by incorporating the residuals of mean gFA of combined cortico-cortical and cortico-thalamic alterations as features. **b)** Schematic of thalamo-cortical dynamical model. C1 represents the lumped cortico-cortical connections, C9 is the connection from thalamus to cortex, C7 indicates the connection from cortex to thalamocortical relay cells, and C8 is the connection from cortex to thalamic reticular nucleus. **c)** Model dynamics colour-coded by behaviour in parameter space. C1 is shown against C7, C8, and C9, with representative two-dimensional slices of the parameter space. The blue region marks the fixed-point dynamics representative of healthy seizure-free activity. The orange and grey regions exhibit spike-wave and fast oscillatory seizure dynamics. Arrows indicate potential ways in altering connectivity that can render a healthy brain to become epileptogenic, according to the model. **d)** Three dimensional slices indicating that the bifurcation orientation is preserved in C8-C1 slices even with changes in C7 and C9 parameters. **e)** An example clinical seizure in IGE is compared with the one simulated from the model in the bistable regime. The model parameter is marked with a corresponding star in **c)**.

An example of clinical seizure recorded from the EEG of an IGE patient is shown in Figure 4.4(e). Note the spike-wave discharges (SWD) occurring during seizures. In addition to the clinical spike-wave dynamics, we also show SWD-like signals generated by our model. As evident, in the model, many key features of clinical spike-wave seizures can be reproduced, including repeating SWD oscillations, morphology of SWD, change in frequency, and fast spike followed by a slow wave.

Connectivity alteration inducing seizure dynamics

The tracts obtained from diffusion MRI analysis are not directed, even though fibre tracts in the human brain are directed. To investigate this, in the model we incorporated directional thalamo-cortical connectivity parameters, which may allow us to predict specific thalamic connections that could lead to seizure dynamics. We scanned each directed thalamic connectivity parameter in the model (C7, C8, C9) with respect to the cortico-cortical connectivity parameter (C1) and determined the bifurcation orientation separating the normal and pathological dynamics as shown in Fig. 4.4(c). With connectivity alterations unconstrained in the model, a number of parameter changes in e.g., C1, C7, C8, C9 can lead to epileptogenic dynamics. Therefore, we constrain the model by validating the orientation of bifurcation in parameter space with the orientation of decision boundary between patients and controls which we previously detected from our imaging data (Fig. 4.4(a)). Using imaging data is crucial to constrain the parameter space of the model within biologically informed boundaries. These constraints facilitate making model-based predictions while also maintaining concordance with the imaging observations.

Imaging analysis in previous sections revealed that the patients have a decreased cortico-cortical connectivity and increased thalamo-cortical connectivity. Thus, the decision boundary has a positive slope with patients (controls) occupying the space above (below) the decision boundary. This observation concords with the bifurcation orientation between cortico-thalamic connections to reticular nucleus (PY$\rightarrow$RE, C8) with respect to cortico-cortical connections (PY$\rightarrow$PY, C1) as shown in Figure 4.4 (panel c(i)). In this panel, the seizure and seizure free regime are separated with a positive slope with the former above the later. This, however, is not the case in Figure 4.4 (panel c(ii)) for C1 vs. C9 and in Figure 4.4 (panel c(iii)) for C1 vs. C7. In both these panels, the bifurcation orientation between the region supporting spike-wave and fixed-point dynamics have a negative slope that does not agree with the dMRI data. Therefore, the model implicates the role of thalamic reticular nuclei in seizures which was not otherwise observable from neuroimaging analysis alone.

Note the bifurcation orientation between cortico-reticular connections (C8) with respect to cortico-cortical connections (C1) is preserved with slight perturbations in parameter C7 and C9 as shown in Figure 4.4(d), suggesting robustness of the result presented.

An exemplary point representing the control population in the region of the normal seizure free dynamics is shown by a circle in green. The model predicts various routes that may place the healthy dynamics in controls to the pathological regime where spike-wave dynamics manifest. As illustrated by the arrows, reduction of cortico-cortical (C1) parameter (purple line), increase in C8 parameter (orange line), or a combination of the two (cyan line) can induce a bifurcation to spike-wave dynamics in the model.

Putting together our model predictions, it appears that the localised alterations in white matter structures contribute to the mechanism of seizures in IGE. After model validation (matching the decision boundary from the dMRI data to our bifurcation orientation), our proposed model suggests that epilepsy manifest due to enhancement of white matter connections *from* cortex *to* reticular nuclei coupled with reduction in cortico-cortical connections. Additionally, the model predicts that reducing the cortico-reticular connectivity can place the model in the normal seizure free regime again, thus offering a target which may be of therapeutic value in IGE.

4.5 Discussion

The main objectives of this study were a) to determine any anatomical abnormalities in white-matter structures in patients with mixed syndrome IGE, and b) to suggest plausible mechanisms of the pathogenesis in IGE.

We applied diffusion MRI Connectometry to identify localised structural connectivity abnormalities not evident using conventional whole-tract based approaches (Figure 4.2(a, b)). In doing so we identified a likely anatomical substrate for the reduced DMN functional connectivity already demonstrated in the same subjects by (McGill et al., 2012).

Analysing the whole-brain white matter structure, we found that patients have decreased cortico-cortical connections consistently in parts of cingulum tracts, fornix, and superior longitudinal fasciculus. However, patients have increased connection strength between thalamic and precentral areas. To understand potential mechanisms, we incorporated our imaging findings into a computational model of thalamocortical interactions. Our modelling framework suggests increased cortico-reticular connectivity coupled with loss of cortico-cortical strength mechanises epileptogenesis in IGE. To our knowledge, this is the first study that combines diffusion imaging with computational modelling to underscore the pathophysiology of IGE being due to impaired white matter structure underlying cortical regions and cotico-thalamic projections of reticular nucleus.

Methodological considerations

In terms of cohort, our sample size of 14 patients is small; however, this is comparable to several previous studies of diffusion MRI analysis in IGE (Focke et al., 2013; Lee et al., 2014; Liu et al., 2011), and reflects the fact that diffusion weighted imaging is not routine in the clinical management of patients with IGE. The sample size distribution of 14/18 at $p = 0.05$ can detect effect size more than 1.2 with 95% statistical power but effect size of 0.9 with only 82% statistical power. High effect size occurs in shorter tracts at high t-scores indicating that we are adequately powered to detect more significant abnormal tracts at a shorter length. Reassuringly, the pattern of abnormalities in tracts at shorter length is consistent with the pattern of cortico-cortical reductions and thalamocortical increases. Our patients were also not drug naive; therefore, it is unclear how our results may be confounded with the effects of medication. Finally, the association between the loss of structural connectivity and functional connectivity between MPFC and PCC should not be simplistically assumed as one driving the

other. Honey et al. 2009 has suggested interregional distance, direct, and indirect connectivity may be additional contributory factors amongst others. Our report of consistent finding across modalities needs more investigation on the exact causal relationship by considering other contributory factors. Although McGill et al. 2012 reports a significant correlation between functional connectivity and epilepsy duration, we did not detect any significant correlation between clinical parameters (i.e., age of onset, epilepsy duration) and altered white-matter structure. Regardless, any correlation does not imply causation; for the given cohort of patients, it remains unclear if these alterations are a) cause of epilepsy, or b) effect of prolonged seizures. A longitudinal study of drug naive cohort is required to disentangle these cause-effect relationships and potential drug effects.

Different approaches can be applied to analyse diffusion MRI. Track based spatial statistics (TBSS) has been widely applied in various studies (Smith et al., 2006), including in epilepsy (Focke et al., 2013; Gong et al., 2017; Groppa et al., 2012; Lee et al., 2014; Li et al., 2010; McGill et al., 2014; O'Muircheartaigh et al., 2011). TBSS is a skeleton-based approach in which a mean FA skeleton is constructed and compared between the groups. While TBSS is an automated approach which has overcome some of the drawbacks of VBM based approaches (such as smoothing, alignment, and reproducibility issues), it still has some limitations. Summarising FA maps into a mean skeleton incurs loss of data; this may not make use of the information from the crossing fibres (Abhinav et al., 2014b). These problems have been overcome in diffusion MRI Connectometry which uses multiple fibre skeleton (multiple fibre orientations per voxel) to sample the diffusion quantities on ODFs. It incorporates q-space diffeomorphic reconstruction, a model-free reconstruction approach based on generalised q-sample imaging which has been shown to resolve the crossing fibre problem efficiently (Abhinav et al., 2014b; Yeh and Tseng, 2013; Yeh et al., 2013b, 2010, 2011).

Converging evidence of connectivity dysfunction

The role of the thalamus in the pathogenesis of epileptic seizures has been long recognised (Avoli, 2012; Gloor, 1979). Simultaneous EEG-fMRI analysis has shown bilateral thalamic activation and deactivation of default mode network (Gotman et al., 2005; Moeller et al., 2010). This has further been corroborated with Positron Emission Tomography (PET) studies in which focal increases in thalamic blood flow have been reported (Prevett et al., 1995). Although a decrease in thalamo-cortical functional connectivity has been suggested between thalamus and frontal cortex (Kim et al., 2014), we did not detect any differences in the

corresponding anatomical connectivity (Appendix C.3), nor was it detected in (McGill et al., 2014). Our findings of bilateral increased thalamo-cortical connectivity are in particular agreement with the study of Groppa et al. 2012 who also demonstrated alterations to FA in the thalamus and juxtacortical precentral areas.

The thalamic reticular nucleus is a part of circuitry normally responsible for generating healthy oscillations, such as sleep spindles (Fuentealba and Steriade, 2005). Several studies have shown that pathological use of this circuitry results in manifestation of generalised spike-wave discharges (Beenhakker and Huguenard, 2009; Huguenard and McCormick, 2007; Lacey et al., 2012; Meeren et al., 2005). Recently, EEG-fMRI analysis performed on IGE patients during early sleep stages revealed enhanced functional connectivity between thalamus and somatomotor region (which include precentral gyrus), amongst other regions (Bagshaw et al., 2017). These reports essentially complement our finding on abnormally high cortico-reticular anatomical connectivity as one of the contributory structures involved in mechanising epilepsy. We hypothesise based on our findings and from our model that abnormal input to the reticular nucleus from cortex can alter its normal inhibitory mechanism to generate pathological seizure activity.

We observed a reduction in white matter connections including the superior longitudinal fasciculus (SLF), fornix, and cingulum. SLF alterations were previously reported by (Focke et al., 2013) who also found reductions in FA in a cohort of 25 patients. Similarly, a study by (Lee et al., 2014) demonstrated microstructural alterations in thalamo-cortical and cortical-cortical connections in a cohort of 14 patients using diffusion kurtosis imaging. Furthermore, (Liu et al., 2011) showed FA reductions in the SLF in a group of 15 patients with JME. The study of (Liu et al., 2011) is in further agreement with ours since they also demonstrated FA reductions in regions of fornix and cingulum.

In this study, we found that parts the cingulum tracts had reduced tract integrity in patients. This is in agreement with functional MRI reductions between PCC and MPFC in the same cohort of patients investigated by (McGill et al., 2012). Cingulum tracts have been previously identified as the only direct anatomical pathway between PCC and MPFC (Heuvel et al., 2009). While one may expect a loss of function with loss of structure, which is also evident from our results on compromised cingulum fibres, the exact relationship on how (direct, or indirect) anatomy constrains function and vice-versa is unclear. For example, interregional distance as well as direct or indirect connectivity have been suggested to be additional

contributory factors (Chu et al., 2014; Honey et al., 2009). Our result suggests a direct structural correspondence for the previously reported functional alteration.

By combining a dynamical model with imaging findings, we have shown evidence of how the white matter alterations in cortico-cortical and cortico-reticular structures may mechanise seizures. This is one of the key novelties of our study. With regard to the hotly debated topic of where the seizures manifest first, in cortex or in thalamus, we do not resolve that in this study as it would require simultaneous investigation of function and structure. However, there is a general consensus that the pathological mechanisms in generalised epilepsies are due to (i) increases in thalamo-cortical activity and (ii) broad decreases (with some possible regional increase) in cortico-cortical interactions (Blumenfeld, 2002, 2003; Duncan, 2005).

Model consideration

We investigated the mechanism of epilepsy genesis in a two-subsystem neural population model of thalamo-cortical interactions. Note that epilepsy genesis (an increased propensity for seizures) is conceptually different to seizure genesis (mechanism underlying a specific transition to a seizure state), which we do not investigate here (Pitkänen and Engel, 2014). The physiological basis of the model is based on the experimental evidence of connectivity shown by (Pinault and O'brien, 2005) and the references therein. Therefore, the resulting dynamics ensuing in coupled neural populations makes the computer model an apt framework for studying the effect of connectivity alteration between cortex and thalamus–as adopted in several other studies (Chen et al., 2017; Fan et al., 2017, 2016). Other models of seizure discharges comparable to the model incorporated here are: Destexhe 1998 at microscopic scale of individual neurons, Robinson et al. 2002 at a macroscopic scale of neural populations, along with phenomenological models Jirsa et al. 2014, spatially extended models (Goodfellow et al., 2011; Taylor et al., 2013b) amongst others (Bhattacharya et al., 2016; Breakspear et al., 2006; Lytton, 2008; Marten et al., 2009; Yousif and Denham, 2005). The mechanism of SWD generation in these models may share some similarities, e.g., most models utilise the slow-fast bursting mechanism (Izhikevich, 2006). Recently, a single framework of diverse bursting patterns has been suggested, enabling a unified classification of the mechanism and parameter changes leading to SWD in each model (Saggio et al., 2017). Using such a framework would be the next step to compare models and understand the full implication of our highlighted connectivity changes.

Conclusion

Case history and visual inspection of epileptiform activity on EEG are currently the standard tools for clinical diagnosis of IGE. Often case histories are unreliable, and about 10% of epilepsy patients never show epileptiform discharges (Smith, 2005). These EEG negative patients could either have IGE or focal epilepsy. Misdiagnosing epilepsy classification and treating with inappropriate anti-seizure medication incurs high-cost (Juarez-Garcia et al., 2006). There is a need for developing diagnostic biomarkers for accurate epilepsy classification (Pitkänen et al., 2016; Smith, 2005) and some efforts to devise quantitative diagnostic tools based on resting-state EEG have been made (Schmidt et al., 2016). Furthering these attempts, we have identified non-invasive, MRI-based markers for discriminating patients with IGE. Structural changes are likely to occur at a much larger time-scale as compared to the dynamical properties of electrographic activity. Therefore, in a clinical setting, our discriminatory framework may be useful as an anatomical biomarker, although reproduction in a separate dataset would be important to verify its generalisability.

In conclusion, we found that patients with IGE have anatomical abnormalities in white-matter thalamo-cortical and cortico-cortical connections which are strikingly bilateral. We have demonstrated how a computational model can enable us to move beyond statistical observations in data to suggest a possible mechanism of IGE manifestation. Our analysis suggests the importance of increased directed connectivity *from* cortex *to* the thalamic reticular nuclei. The observed change creates a bistability in the network dynamics of our model – permitting the occurrence of occasional pathological epileptiform discharges. Taken together, our work may be of clinical interest for diagnostics, and the mechanistic insight suggests specific structural targets for the next generation of therapies in IGE.

Chapter 5

Discussion

5.1 Summary of key findings and implications

This thesis studied the abnormalities in the whole-brain structural network and white-matter fasciculi of patients with intractable temporal lobe epilepsy and mixed-syndrome idiopathic generalised epilepsy. We statistically quantified abnormalities in the whole-brain and assessed its association with a) seizure outcome after epilepsy surgery in focal epilepsy, b) patient susceptibility to secondary generalised seizure, and c) epileptogenesis mechanisms in primary generalised seizures.

Chapter 2 showed that drug-resistant epilepsy patients are heterogeneous in terms of their brain network abnormalities. Some network abnormalities may remain after surgery, and those remanent network abnormalities associate with persistent seizures after surgery. We harnessed the heterogeneity between patients by combining patient-specific routine clinical attributes with network abnormality data for predicting the probability of seizure recurrence. This chapter showed that it is possible to identify a patient's predisposition to seizure recurrence before they are operated on, which would help counsel patients appropriately before the surgery and get an idea about which patient may need a longer follow-up and closer monitoring after the surgery.

Chapter 3 showed that more and widespread abnormalities are present in patients with drug-resistant TLE and focal to bilateral tonic clinic seizures. The underlying abnormal structural network substrate likely supports the rapid spread of seizure activity in FBTCS. This chapter

showed that it is possible to quantify a patient's susceptibility to FBTCS, which would help identify patients at risk to these severe seizures; thus, it would caution our clinicians before tapering their seizure suppressing medications.

Chapter 4 showed that local abnormalities in major white-matter fasciculi are present in patients with IGE. Even though an IGE patient's MRI appears normal to an expert radiologist, the microstructural alterations to the white-matter structure have a typical pattern of cortico-cortical decreases and cortico-thalamic increases. Though these changes are patient-specific, we can draw a clear decision boundary to separate patients from controls, thus reducing the chances of misdiagnosis. This chapter suggested a likely mechanism of epileptogenesis by implicating the role of cortico-reticular connection; a targeted treatment on these connections might be useful to those at risk of developing epilepsy and can be tested on animal models.

Chapter 2 and Chapter 3 show the relationship between structural network abnormality, seizure recurrence, and the presence of FBTCS. In patients with intractable seizures, node abnormality is significantly increased compared to controls. Increase in node abnormality links with the likelihood of focal seizures recruiting widespread bilateral areas before surgery and seizures persisting after surgery. Chapter 3 and Chapter 4 shows a relationship between widespread network changes in secondary-widespread seizures and focal changes in primary-widespread seizures. Primary-widespread seizure in IGE, controlled with seizure suppressing medication, is associated with widespread, more focal abnormalities in white matter structures. Secondary-widespread seizures, poorly controlled with seizure suppressing medications, are associated with widespread abnormalities. These chapters, taken together, suggest that uncontrolled seizures induce abnormalities in the brain network, and those abnormalities drive a patient to intractability. Conversely, controlled seizures would restrain the progression of abnormalities, and when those abnormalities plummet to a baseline control level, epilepsy patients remit from seizures.

While this thesis addresses some of the critical treatment challenges outlined in chapter 1, several steps remain before translating our approach into clinical practice. The following sections will discuss the challenges to be addressed and some avenues for future research in light of our findings.

5.2 Challenges to be addressed

This thesis raises a critical question of whether the diffusion abnormalities reflect the underlying pathology that causes a patient to have poor seizure outcomes and greater seizure spread, or are they the consequence of epilepsy and a biomarker of damage by seizures. All studies in this thesis were cross-sectional in design. Even though we quantified, mapped, and discovered an association with diffusion MRI abnormalities, we could not ascertain any causative relations to surgical outcomes and seizure spread. Though some studies hypothesize that the white matter changes are secondary effects rather than causal, longitudinal studies are needed to answer this question (Hatton et al., 2020).

The experiments in this thesis were not sufficient to elucidate the pathophysiological mechanism of ictogenesis or epileptogenesis. As described in this thesis, diffusion MRI abnormalities would be useful to be considered alongside routine clinical data to enable better patient stratification. However, it is essential to note that correlations are not mechanisms; a mechanism can explain many correlations. Disease-modifying treatments—counteracting epileptogenesis, seizure modification, and cure—necessitates an understanding of pathophysiological mechanisms (Pitkänen and Engel, 2014; Pitkänen et al., 2016). Animal models informed with computational approaches described in this thesis presents an excellent opportunity to elucidate the pathophysiological mechanisms of epilepsy (Liou et al., 2018).

All studies in this thesis were retrospective in design with data acquired at a single epilepsy centre. This thesis could only include the data for temporal lobe epilepsy patients and a small sample of mixed-syndrome IGE patients. All patients were taking anti-epileptic drugs and were not drug-naive. The uncertainties about treatment outcomes are known to be even higher for extra-temporal lobe and non-lesional epilepsy patients. The effect of anti-epileptic drugs on brain networks is unclear. These are confounding factors that can limit the translation of our work into clinical practice. Therefore, a large scale replication study on a heterogeneous cohort of epilepsy patients from multiple centres is crucial. To enable these endeavours, we have made all the codes and data presented in this thesis publicly available. However, there would still be challenges associated with data harmonisation, which some studies are beginning to tackle by applying methods like ComBat (Hatton et al., 2020; Yamashita et al., 2020).

5.3 Avenues for future research

5.3.1 Functional network abnormalities

Refractory focal epilepsy patients have increased functional network connectivity in seizure onset regions of the brain—resection of these hyperconnected brain areas associated with increased chances of seizure freedom (Englot et al., 2015; Lagarde et al., 2018; Narasimhan et al., 2020; Shah et al., 2019b). This thesis shows that fewer structural brain network abnormalities remaining after surgery is associated with seizure-free outcome. Are ictogenic regions which are hyperconnected also have increased functional network abnormality? The gap in our understanding requires mapping the functional network abnormalities to reconcile them with structural network abnormalities and hyperconnectivity of seizure onset regions for identifying the epileptogenic network.

We can *hypothesise* that when surgery overlaps with hyperconnected brain areas, which are also abnormal, the patient will have a good seizure outcome and a lower likelihood of seizure relapse. A low concordance between functional network hyperconnectivity and abnormality would lead to persistent seizures post-surgery.

Mapping patient-specific functional network abnormalities require healthy functional connectivity from a population of controls. A standard preprocessing pipeline can estimate the resting-state functional networks from non-invasive modalities, like fMRI, MEG, or EEG for healthy subjects. In invasive modalities such as SEEG/ECoG, computation of healthy functional networks have been made possible by some recently established approaches (Betzel et al., 2019; Frauscher et al., 2018). We can compare every link of the functional connectivity network in patients with the equivalent link in the control population to infer how abnormal the functional connection is. We can then compare the node abnormality from the abnormal/z-scored functional connectivity network and the node strength of the original functional network while relating them to the location of surgery and seizure outcome.

The results from such a study could locate the hubs in the brain, and then grade the hubs as normal or abnormal. Hubs are known to have an association with post-surgery seizure outcome (Gleichgerrcht et al., 2020). Studying normal/abnormal hubs and surgery information may help devise a more targeted treatment, which is now becoming possible with minimally invasive laser ablation procedures.

5.3.2 Coupling between structural and functional networks

Structural and functional brain networks correlate at multiple temporal and spatial scales (Honey et al., 2009). Structural connectivity constrains functional connectivity, and functional connectivity modulates structural connectivity via mechanisms of plasticity (Chu et al., 2014). Surgery disrupts the structural epileptic network to control abnormal functional network dynamics (Shah et al., 2019a). Therefore, it is crucial to investigate the changes in structure-function coupling due to surgery and its link to post-surgical seizure freedom.

We can *hypothesise* that stronger structure-function coupling is associated with seizure free outcomes because structural alteration by surgery can better modulate function in a strongly coupled network.

To test this hypothesis, we would need a structural connectivity matrix, a functional connectivity matrix, and a measure of coupling. Information theory measures are applied routinely on signals recorded from intracranial EEG to estimate functional connectivity matrix. To infer the structural connectivity matrix, we can map each electrode on the pre-operative space of diffusion MRI data and find the connections between electrodes through tractography algorithms. The structure-function coupling can be tested by studying these matrices. We can measure the corresponding functional connectivity for every structural connectivity present between electrodes and assess a correlation as a coupling measure. Virtual surgeries by node resection to this network model can quantify the effect of surgery on the structure-function coupling (Kini et al., 2019; Shah et al., 2019a).

We expect such a framework to elucidate the association between structure-function coupling measure and seizure outcomes after surgery. If such an association is present, surgery in good (poor) outcome patients may likely have overlapped with regions whose removal would boost (dampen) the resulting coupling between structural and functional networks. This study can provide insights on how to perturb the structural epileptic networks for controlling the functional dynamics (Khambhati et al., 2016).

5.3.3 Predicting locations for intracranial electrode placements

Many patients with drug-resistant focal epilepsy undergo intracranial EEG implantation for localising epileptogenic brain tissues. Placing electrodes in the brain and waiting for seizures to occur, some time for days, is arguably one of the most invasive diagnostic tests in medicine.

We can reduce the invasiveness by guiding electrode placements. There is a need to predict where to place the electrodes in the brain to collect data from epileptic networks and how many brain areas need implantation (Duncan et al., 2016).

We can *hypothesise* that a combination of non-invasive whole-brain modalities like fMRI/MEG and MRI can predict the aberrant functional dynamics captured by invasive electrode implantations.

We can test this hypothesis in three steps. First, we need to identify the extent to which whole-brain structural connectivity from MRI can predict functional network dynamics from intracranial EEG data (Shah et al., 2019a). Such predictions enable us in identifying the structural connectivity biomarkers of seizure generation and progression observed on intracranial EEG. Second, we need to determine how much correlation is present between functional connectivity obtained from non-invasive whole-brain MEG/fMRI imaging and functional connectivity from intracranial EEG (Murakami et al., 2016). This analysis will allow us to identify non-invasive functional connectivity biomarkers of seizure generation and spread. Third, we need to combine non-invasive biomarkers of structural and functional connectivity to characterise epileptic network and predict brain tissues for electrode implantation (Betzel et al., 2019; Goni et al., 2013). With the growing precedence of implanting stereotactic EEG over intracranial EEG across epilepsy centres, this study would be hugely beneficial for precise targeting of epileptic network and improving surgical outcomes.

5.4 Concluding remark

Developing practical tools for improving clinical care of epilepsy patients and reducing misdiagnosis were the key goals of this thesis. We believe that quantitative methods are crucial for developing individualised treatments. Quantitative approaches can unify the vast multidisciplinary information, routinely collected from epilepsy patients. Complementing clinical decision-making about a patient's risk, evaluating the efficacy of a treatment, prescribing follow-up timelines, hence, enabling better diagnosis and therapy is the ultimate objective of such quantifications.

Making progress towards these goals, this thesis highlighted the importance of quantifying diffusion MRI abnormalities in drug-resistant focal epilepsy and generalised epilepsy for predicting surgical outcomes and seizure spread. We, as well as other groups, have envisioned

a pipeline for integrating our quantitative approaches into clinical practice (Morgan et al., 2020; Taylor et al., 2018). Our findings are significant because it merges the state of the art network neuroscience, engineering, neurology, and neurosurgery towards making practical tools for improving and standardising patient care in epilepsy.

Appendix A

TLE Surgery Supplementary

A.1 Imaging protocols and pre-processing pipeline

MRI data were acquired on a 3T GE Signa HDx scanner (General Electric, Waukesha, Milwaukee, WI). Standard imaging gradients with a maximum strength of $40mTm^{-1}$ and slew rate $150Tm^{-1}s^{-1}$ were used. All data were acquired using a body coil for transmission, and 8-channel phased array coil for reception. Standard clinical sequences were performed including a coronal 3D T1-weighted volumetric acquisition (matrix, $256 \times 256 \times 170$; in-plane resolution, 0.9375×0.9375 mm with slice thickness 1.1 mm). Diffusion MRI data were acquired using a cardiac-triggered single-shot spin-echo planar imaging sequence with echo time =73 ms. Sets of 60 contiguous 2.4 mm-thick axial slices were obtained covering the whole brain, with diffusion sensitizing gradients applied in each of 52 non-collinear directions (b-value of $1200mm^2s^{-1}$ $\delta = 21ms, \Delta = 29ms$ using full gradient strength of $40mTm^{-1}$) along with 6 non-diffusion weighted scans. The gradient directions were calculated and ordered as described elsewhere (Cook et al., 2007). The field of view was 24×24 cm, and the acquisition matrix size was 96×96, zero filled to 128×128 during reconstruction, giving a reconstructed voxel size of $1.875 \times 1.875 \times 2.4$ mm. The DTI acquisition time for a total of 3480 image slices was approximately 25 min (depending on subject heart rate). These protocols are identical to our previous study (Taylor et al., 2018).

The pre-surgery and surgically-spared networks are generated as follows: the preoperative T1 image were parcellated into 114 cortical and subcortical regions of interest (ROIs) derived from the predefined Geodesic Information Flow atlas and separately in 82 ROIs using the

Freesurfer Desikan-Killiany atlas in the native space of each participant. We registered the parcellated ROIs, resection mask, and tracts from deterministic tractography on dMRI data in native space. The pre-surgical streamline network is the connectivity matrix depicting the number of streamlines connecting two ROIs. The surgically-spared streamline network is inferred after removing the streamlines that intersected the resection mask. By definition, surgery can only cause an immediate reduction in the number of streamlines. Therefore, we specified that the surgically-spared network contains only those network edges which are not expected to change in streamline count following surgery (i.e., edges where their streamlines do not pass through/into the resection cavity).

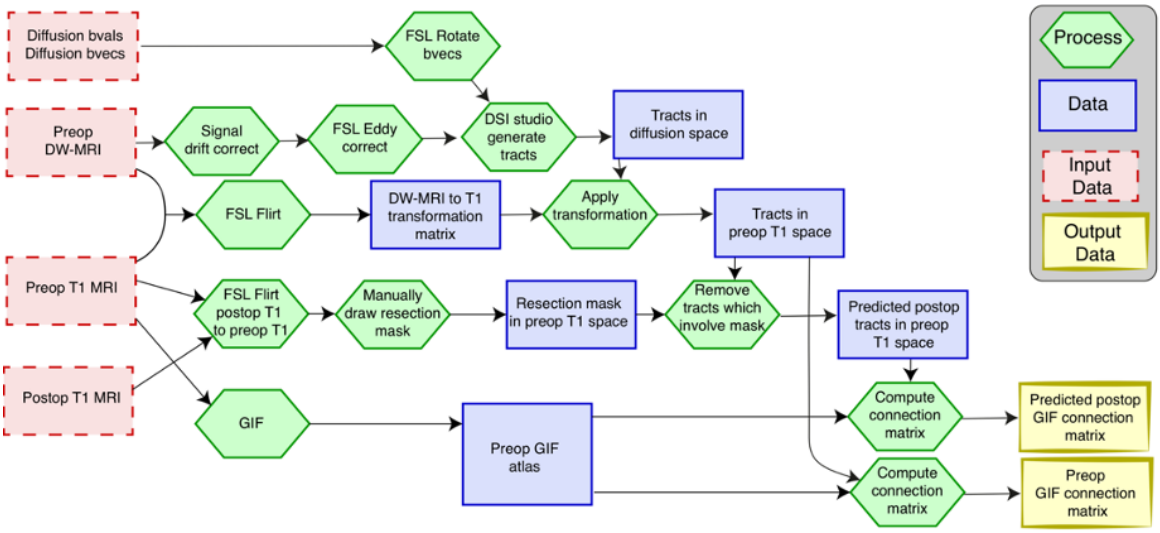

Fig. A.1 Summary of processing pipeline (reproduced from (Taylor et al., 2018)) to generate GIF network. The pipeline is applied to each subject.

We applied the same image pre-processing steps that we previously established on this data in our recent study (Taylor et al., 2018). The image processing pipeline is summarised in the flowchart reproduced from (Taylor et al., 2018).

Preoperative diffusion MRI data were first corrected for signal drift (Vos et al., 2016), then eddy current and movement artefacts were corrected using the FSL eddy_correct tool (Andersson and Sotiropoulos, 2016). The b vectors were then rotated appropriately using the 'fdt-rotate-bvecs' tool as part of FSL (Jenkinson et al., 2012; Leemans and Jones, 2009). The diffusion data were reconstructed using generalised q-sampling imaging (Yeh et al., 2010) with a diffusion sampling length ratio of 1.2. A deterministic fibre tracking algorithm (Yeh et al., 2013b) was then used, allowing for crossing fibres within voxels, with seeds placed at

the whole brain. Default tractography parameters from the 14 February 2017 build of DSI studio software were used as follows. The angular threshold used was 60 degrees and the step size was set to 0.9375mm. The anisotropy threshold was determined automatically by DSI Studio. Tracks with length less than 10 mm and more than 300mm were discarded. A total of 1,000,000 tracts were calculated per subject and saved in diffusion space.

To align the tracts with the ROIs we linearly registered the first non-diffusion-weighted image to the preoperative T1 image and saved the inverse of this transformation matrix using FSL FLIRT. We then multiplied every coordinate in every tract by this transformation matrix to get the tracts in T1 space. The quality of the registration between tracts, ROIs, and the resection mask was confirmed through visual inspection for all subjects. Since networks are constructed in native space, this removes any mismatching of track types due to potential non-linear registration issues which is advantageous compared to previous studies of network change. To generate preoperative connectivity matrices, we looped through all tracts and deemed two regions as connected if the two endpoints of the tract terminate in those regions. This generated a weighted connectivity matrix in which each entry in the matrix represents the number of streamlines connecting two regions. To generate surgically-spared connectivity matrices, we performed the same process as above with one exception. Any tract that had any point within the resection mask was excluded from building the matrix. The inferred surgically-spared network therefore always had fewer streamlines than the preoperative network.

A.2 SVM model design and nested cross-validation

We predicted the patient-specific probability of seizure relapse using 13 preoperative clinical data, pre-surgery node abnormality, and the surgically-spared node abnormality. Preoperative clinical data (mentioned in Table 1, S1) included: sex, epilepsy onset age, age at surgery, epilepsy duration, number of anti-epileptic drugs taken preoperatively, history of status epilepticus, evidence of secondary generalised seizures, side of surgery, preoperative MRI pathology, evidence of hippocampal sclerosis, history of depression, history of psychosis, and history of other psychiatric disorder.

We performed this using support vector machine (SVM) implemented in MATLAB ‘fitcsvm’ classification library (Guyon et al., 2002; Platt, 1999). We applied a linear kernel because this enables the interpretation of weight vectors (i.e., the relative importance of each feature

in the prediction), which were used to rank the importance of metrics in identifying patients who would have suboptimal seizure outcome. SVMs were initially trained with all 15 preoperative metrics: 13 clinical, 1 pre-surgery node abnormality, and 1 surgically-spared node abnormality. To identify the most informative metrics, after each round of SVM training, we removed the least important metric (in terms of its weight vector) and trained a new SVM with the remaining metrics. We repeated this process until only a single metric remained (Fagerholm et al., 2015; Guyon et al., 2002). At each stepwise removal we recorded: a) the performance of classifier in classifying totally seizure free (ILAE 1) and non-seizure free (ILAE 3-6) patients, and b) the Spearman's rank correlation between the predicted probability of seizure relapse for each patient with the actual severity of seizure outcomes at one-year after surgery (ILAE class).

The performance of the classifier was estimated using binary classification. Given that ILAE 2 patients tend to relapse (Table 1, S1), and thus, are in the spectrum between the totally seizure free (ILAE 1) and non-seizure free (ILAE 3-6) patients, we first excluded the ILAE outcome group 2 patients (Fairclough et al., 2017). With these patients removed, our dataset consisted of 43 samples, 34 of which were labelled 1 corresponding to ILAE 1, and 9 were labelled -1, corresponding to ILAE 3-6. On this dataset, we performed nested-cross validation by combining a three-way split of the data (training-validation-testing) with leave-one-out cross-validation (CV) and grid search for SVM parameter (box-constraint) tuning. This was done to avoid upward bias in the metrics of performance estimates (Guyon and Elisseeff, 2003; Tsamardinos et al., 2018). Additionally, we avoided any bias in the selection of the most discriminatory threshold pair (i.e., z-score and percentage abnormality) to determine the node abnormality by computing it at every step of cross-validation after removing the test subject (Smialowski et al., 2009).

Specifically, in nested-cross validation, an external leave-one-out is implemented in which one patient is left out at every step for testing and the remaining patients used for training and validation. Training and validation were performed in the internal leave-one-out CV in which one patient is again left out for validation and the remaining used for model training combined with model parameter tuning. In our analysis, we tuned the model on 100 logarithmically spaced grid points between 1 and 10. At every point, the SVM is trained and its performance tested using the patient left out for validation by estimating AUC. We selected the model parameter that gave the highest cross-validated AUC. The classifier generalisation capability is then evaluated by computing the classification AUC, accuracy, sensitivity, and specificity

using the patient originally left for testing in the external cross-validation. We also noted the probability with which each test patient was classified as non-seizure free. The intuition being that the predictive model, though blind to the non-seizure free outcome categories (i.e., all ILAE 3 to ILAE 6 are labelled as -1), would classify the patients with worse surgical outcome with a higher probability.

To determine where the ILAE outcome group 2 subjects fall on the spectrum, we treated all 8 ILAE outcome group 2 patients as test subjects. SVMs were trained and tuned, as described above, on all the remaining seizure free (ILAE 1) and non-seizure free (ILAE 3-6) patients (43 patients). On the classifier with highest discrimination between the seizure free and non-seizure free patients, we tested the features of ILAE 2 patients to note only the probability of classification to the non-seizure free group. We refer to these probabilities as the likelihood of seizure relapse because a high probability indicates a predicted propensity towards a non-seizure free outcome. Having obtained the likelihood of seizure relapse for all 51 patients, we compared this with the surgical outcome categories at year 1 and the actual seizure relapse in five years post-surgery. Note that the labels for all training data are binary and based on 12-month ILAE1 versus ILAE3-6 outcomes only. The model is therefore blind to severity of outcome (i.e. ILAE class 2, 3, 4, 5), and also blind to outcomes beyond 12 months.

A.3 Inferring imprecise AED information

For one patient, the clinical metadata was incomplete—the number of AEDs taken by patient 43 was imprecise. To infer a value for the number of AEDs for this patient, we investigated the predictive power of the remaining clinical data for AEDs prediction using multiple linear regression. The fitting of the linear regression model was achieved using stats package in R, which uses the Least Squares method to minimise the sum of the squares of residuals. Initially, we included all available clinical data in the linear regression model. However, to overcome multicollinearity and remove redundant predictors we discarded, at each round, the predictor with highest p-value, until the regression model and its coefficients were statistically significant. A significant model ($p = 0.002$) with normally distributed residuals (Shapiro-Test: $p = 0.7159$) was obtained using epilepsy duration as single significant predictor. The model was used to predict, for the patient with missing data, the number of AEDs and its 95% confidence interval.

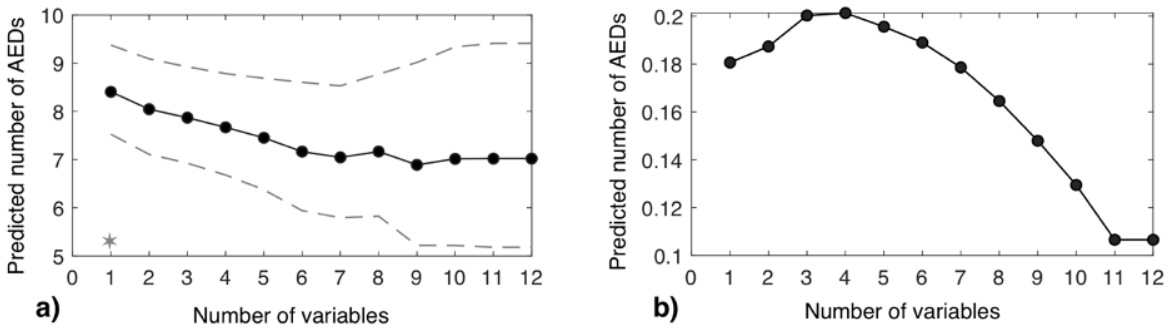

Fig. A.2 Prediction of number of AEDs for the patient with imprecise AED data. The number of variables represents the number of predictors used by the model at each round. In panel a) the solid line represents the predictive AEDs value and the dash lines the upper and lower confidence interval. The adjusted r2 of the model at each round is shown in panel b)

Since number of AEDs cannot be a fraction, we predicted the number of AEDs taken by patient 43 was 8. The following figure shows that the prediction performance remained similar regardless the imprecise data being imputed, left unchanged, or with patient 43 removed from the analysis. Thus, our results are robust to this missing data.

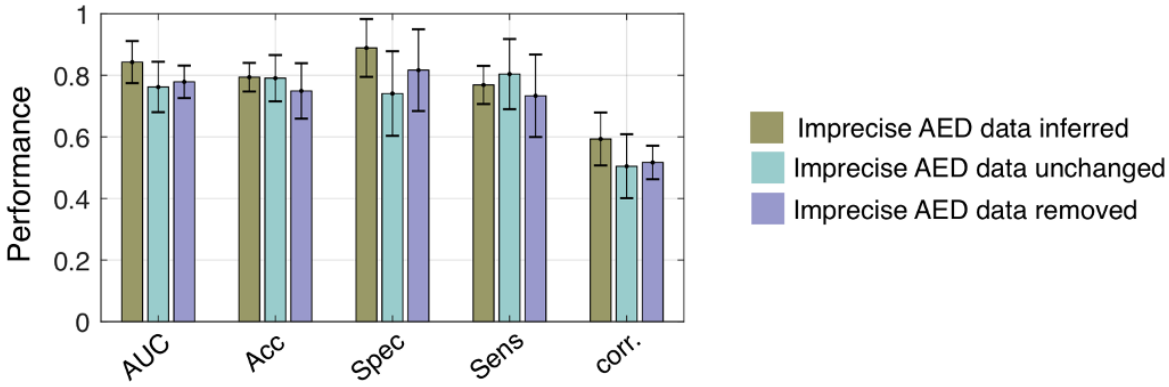

Fig. A.3 Consistent prediction performance was achieved regardless of how the imprecise AED data for patient 43 was treated. The bar plot shows the average performance metrics of SVMs in terms of AUC, accuracy, specificity, and sensitivity. The error bars represent the standard deviation across each step-wise feature removal.

A.4 Consistency across thresholds for pre-surgery and surgically-spared networks

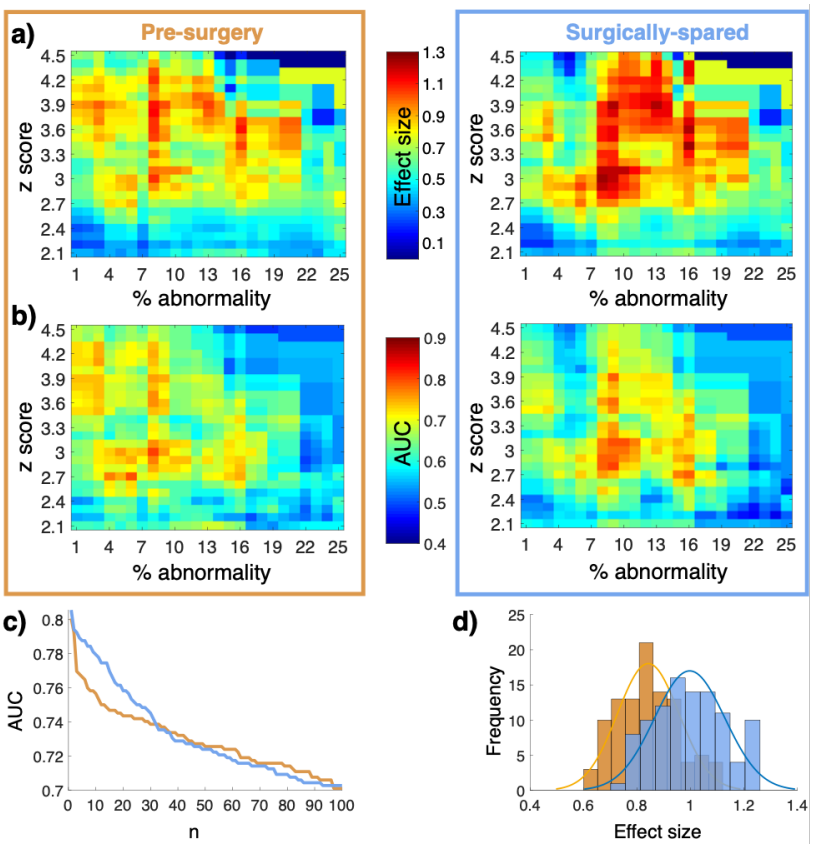

Fig. A.4 Association between node abnormality and surgical outcomes in pre-surgery and surgically-spared network is consistent across thresholds.a) Effect size (d-score) for node abnormality between ILAE 1 and ILAE 3+ groups in pre-surgery and surgically-spared networks. Positive effect size indicates higher node abnormality in ILAE 3+ patients compared to ILAE 1 patients. Medium to large positive effects size, colour coded in red, are evident across a large range of thresholds. b) AUC quantifying the discriminatory value of node abnormality is shown at every point on the threshold grid for pre-surgery and surgically-spared networks. c) 100 highest AUCs sampled from the threshold grid of pre-surgery and surgically-spared networks in panel b) are plotted against each other. Relatively higher AUCs are apparent in surgically-spared networks. d) Histogram of effect size sampled from pre-surgery and surgically-spared networks corresponding to the threshold values of 100 highest AUCs of surgically-spared network.

A.5 Surgically-spared networks are more discriminatory than the pre-surgery network

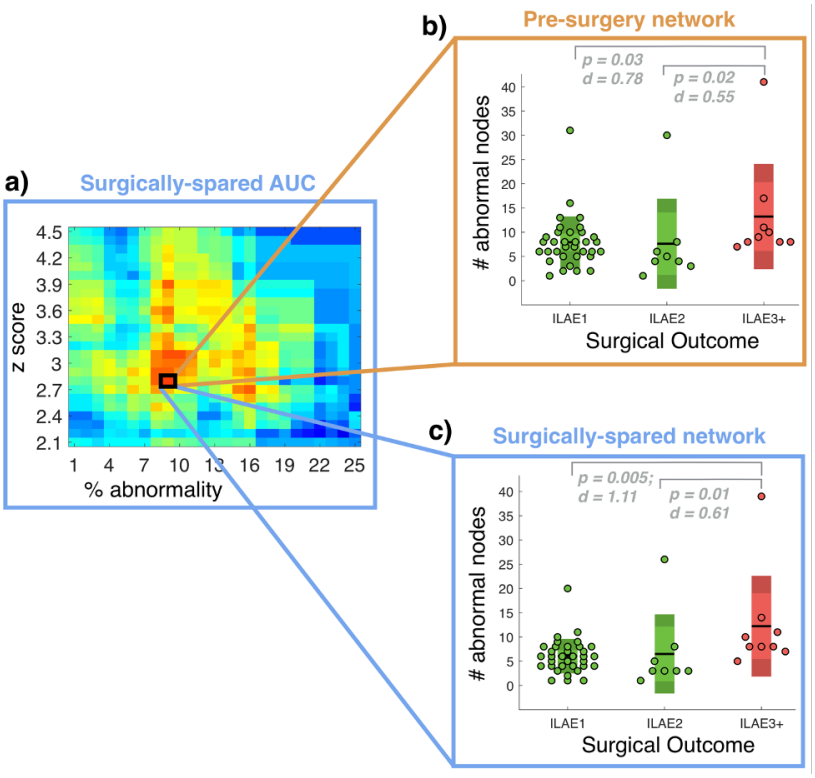

Fig. A.5 Surgically-spared networks are more discriminatory than the pre-surgery networks. a) Corresponding to the threshold of highest AUC, results are shown for pre-surgery and surgically-spared networks. b) Node abnormality computed from pre-surgery network discriminates ILAE1 from ILAE3+ with an effect size of d = 0.78 [95%CI 0.04, 2.1] and ILAE 2 from ILAE 3+ with an effect size of d = 0.55 [95%CI -0.95, 2.0]. Other statistical estimates in pre-surgery network: ILAE1 (n=34) median 7.5 [95%CI 6, 8.5]; ILAE2 (n=8) median 4.5 [95%CI 3, 8]; ILAE3+ median 9 [95%CI 8, 17]. In comparison, node abnormality computed from surgically-spared networks in c) discriminate ILAE1 from ILAE3+ with an effect size of d = 1.11 [95%CI 0.42, 2.2] and ILAE2 from ILAE3+ with an effect size of d = 0.61 [95%CI -0.92 2.04]. Other statistical estimates in surgically-spared network: ILAE1 (n=34) median 6 [95%CI 5, 7.5]; ILAE2 (n=8) median 3 [95%CI 2, 5.5]; ILAE3+ median 8 [95%CI 5, 10].

A.6 Widespread effect of surgery in reducing node abnormality

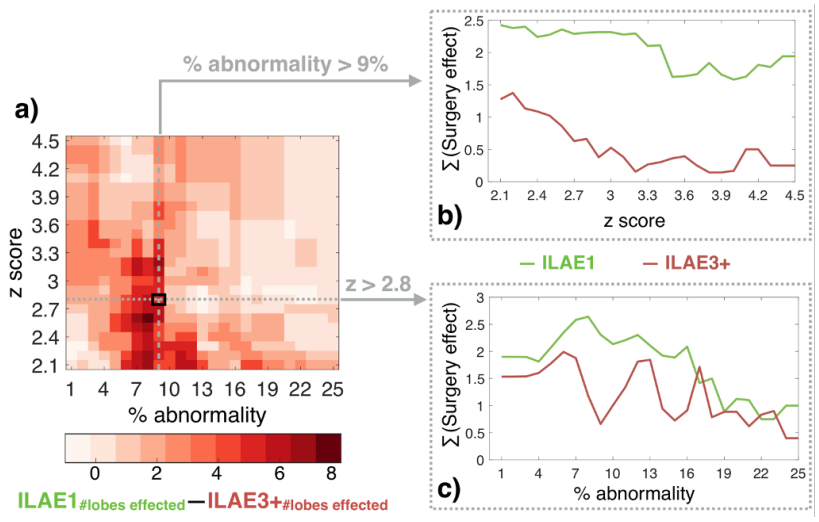

Fig. A.6 The widespread effect of surgery in reducing node abnormality in seizure free group is consistent across the thresholds. Furthering our results in Figure 2.4, we show the difference between the number of lobes effected in seizure free and non-seizure free group across thresholds in panel a). Positive differences in a) indicate that surgery effects the node abnormalities in more brain areas of ILAE 1 group compared to ILAE 3+ group. Along the two slices taken from the grid, the net effect of surgery is shown between ILAE 1 and ILAE 3+ groups in panel b) and c). The effect of surgery at each lobe is computed as: 1 – ratio of proportion of abnormal nodes in ILAE1 to ILAE3+. The net effect of surgery is computed as the sum of the aforementioned ratio across all the ipsilateral and contralateral brain areas.

A.7 Consistency with Desikan-Killiany parcellation scheme

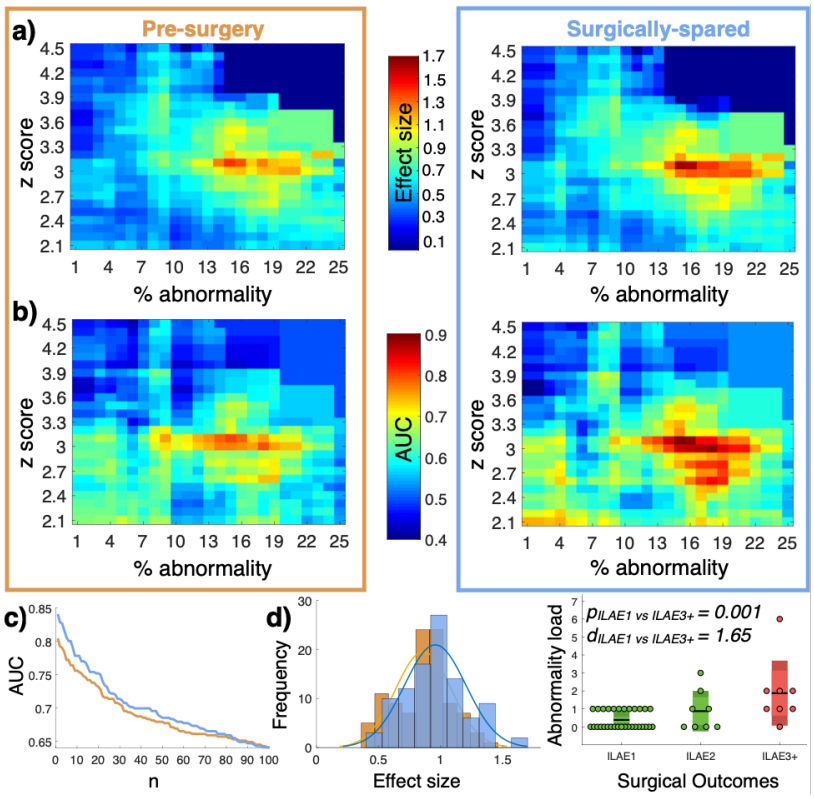

Fig. A.7 With networks inferred using Desikan-Killiany parcellation scheme the association between node abnormality and surgical outcomes in pre-surgery and surgically-spared networks are consistent across thresholds. a) Effect size (d-score) for node abnormality between ILAE 1 and ILAE 3+ groups in pre-surgery and surgically-spared networks. Positive effect size indicates higher node abnormality in ILAE 3+ patients compared to ILAE 1 patients. Medium to large positive effects size, colour coded in red, are evident across a large range of thresholds. b) AUC quantifying the discriminatory value of node abnormality is shown at every point on the threshold grid for pre-surgery and surgically-spared networks. c) 100 highest AUCs sampled from the threshold grid of pre-surgery and surgically-spared networks in panel b) are plotted against each other. Relatively higher AUCs are apparent in surgically-spared networks. d) Histogram of effect size sampled from pre-surgery and surgically-spared networks corresponding to the threshold values of 100 highest AUCs of surgically-spared network. e) At an example point on the threshold grid corresponding to the highest AUC, the box plot shows significantly higher number of abnormal nodes in ILAE 3+ patient than in ILAE 1 patients.

A.8 Change in node abnormality load

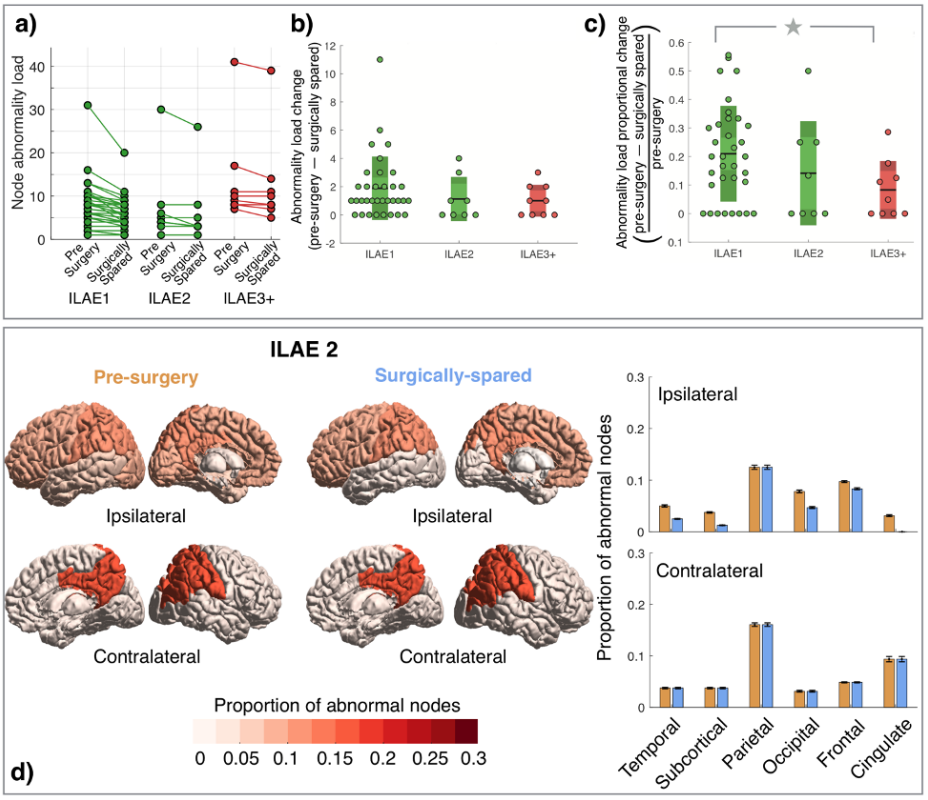

Fig. A.8 Change in node abnormality load between pre-surgery and surgically-spared networks. a) Reduction in the number of abnormal nodes between pre-surgery and surgically-spared networks are shown for ILAE 1, ILAE 2, and ILAE 3+ patients. ILAE 3+ patients have a greater number of abnormal nodes than ILAE 1 patients. Inspecting visually, the reduction of abnormality load, apparent by the slope of the lines, are more in ILAE 1 patients than in ILAE 3+. Reduction in ILAE 2 patients are intermediate to ILAE 1 and ILAE 3+. b) The absolute reduction in abnormal nodes between pre-surgery and surgically spared networks are higher on average in ILAE 1 patients but not statistically significant (p=0.14; d=0.42 [95%CI -0.25, 0.84]). c) The proportional drop in the number of abnormal nodes between pre-surgery and surgically-spared networks relative to the node abnormality load pre-surgery is significantly higher (p=0.01; d=0.81 [95%CI 0.2, 1.4]) in the ILAE 1 patients (n=34, median 0.2 [95%CI 0.14, 0.3]) compared to the ILAE 3+ patients (n=9, median 0.05 [95%CI 0, 0.15]). d) Equivalent of Figure 4 for ILAE 2 patients: Spatial reduction in node abnormality due to surgery in ILAE 2 patients are also intermediate to ILAE 1 and ILAE 3+ patients. Bar plot shows the drop in surgically-spared network compared to pre-surgery network in five ipsilateral (temporal subcortical, occipital, frontal, and cingulate) only.

A.9 Permutation test for regression slope

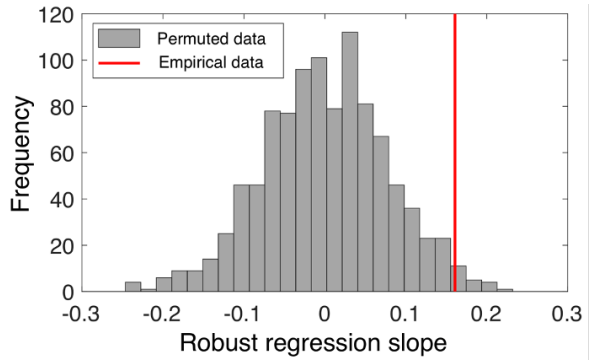

Fig. A.9 Steepness of regression slope obtained from robust regression tested for significance using permutation testing ($p = 0.004$, number of permutations = 1000).

A.10 Association between seizure relapse and combined clinical and network attributes

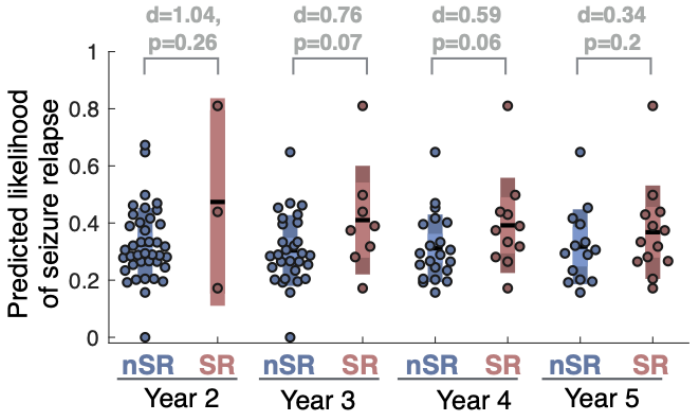

Fig. A.10 On combining network features with clinical attributes association with relapse is lost. The predicted 12-month likelihood of seizure relapse was estimated from the SVM model at an example combination of features that yielded highest classification performance (corresponding to Figure 2.5b-c). Amongst the patients who were initially seizure-free (i.e., ILAE 1 or ILAE 2 at year 1), the likelihood of seizure relapse was not different to those who had a subsequent relapse.

Appendix B

FBTCS Supplementary

B.1 Widespread network alterations in MD networks associate with FBTCS

We applied NBS to compare MD weighted connectivity matrices of FBTCS+ and FBTCS- patient groups with the control group. Figure B.1a) illustrate alteration of each connection quantified by t-scores computed within the NBS analysis for FBTCS+ vs. control group comparison on the left and FBTCS- vs. control group comparison on the right. Positive (negative) t-score indicates increase (decrease) in MD of patients compared to controls. We found that the higher positive t-scores were widespread across many connections in FBTCS+ patients compared to FBTCS- patients. Figure B.1b) Applying NBS analysis, we identified significantly increased subnetwork (connected component) at pre-specified t-score thresholds in FBTCS+ and FBTCS- patient groups compared to control group. The number of edges contained in the altered subnetwork represents the extent of alteration. We detected that the FBTCS+ patients (in orange) have higher extent of alteration than the FBTCS- patients (in teal) across all t-score thresholds. Figure B.1c) An example of significantly increased connected subnetwork in FBTCS+ and FBTCS- patients; MD at every edge of this subnetwork was reduced in patient with respect to controls with $t > 2.5$. While the altered subnetwork is widespread in FBTCS+ patient group (upper panel), it is limited primarily to the regions in the temporal, frontal, and occipital lobes in FBTCS- patient group (lower panel).

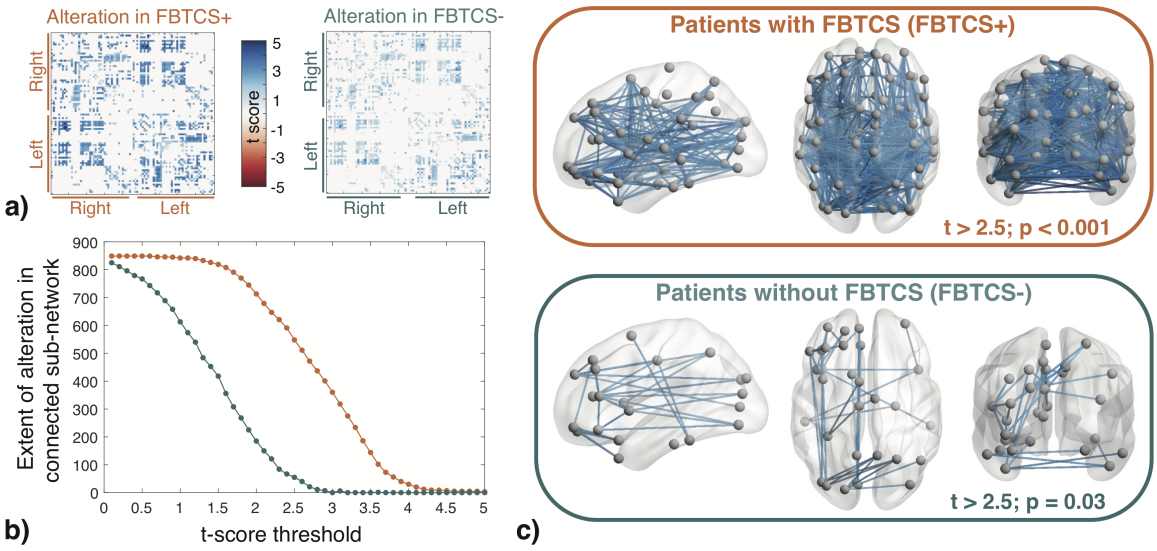

Fig. B.1 Widespread network alterations associate with secondary generalisation of temporal lobe seizures. This figure is equivalent of Figure 3.2 for mean diffusivity weighted whole-brain structural networks.

B.2 Separately analysing the left and right TLE

We repeated the NBS analysis after separating the left and right TLE patients. For the left TLE analysis shown in the left panel Figure B.2(a-b) 32 patients had a history of FBTCS (FBTCS+) and 10 patients had focal-only seizures (FBTCS-). For the right TLE analysis shown in the right panel Figure B.2(c-d) 28 patients had a history of FBTCS (FBTCS+) and 13 patients had focal-only seizures (FBTCS-). As shown in Figure B.2 panel a) and c), we found higher positive t-scores were widespread across many connections in FBTCS+ patients compared to FBTCS- patients in both left and right TLE analyses. Figure B.2b-d) Applying NBS analysis, we detected that FBTCS+ patients (in orange) have higher extent of alteration than FBTCS- patients (in teal) across all t-score thresholds in both left and right TLE patients analysed separately. Due to the reduced statistical power in FBTCS- patient group, we did not detect any subnetwork that was significantly reduced at $p < 0.05$. Examples of significantly reduced connected subnetwork in FBTCS+ and FBTCS- patients are shown in the inset of panel d) for $t > 2$. These findings shown here for separate left and right TLE analysis are consistent with our combined left-right TLE analysis shown in Figure 3.2.

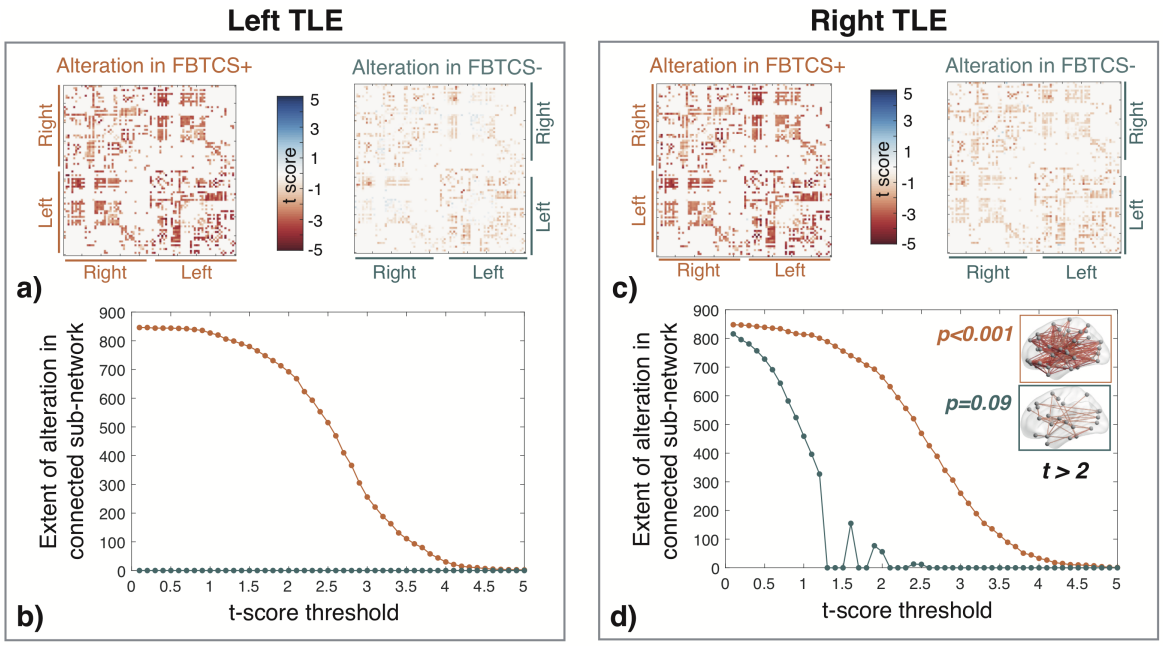

Fig. B.2 Widespread network alterations associate with secondary generalisation of temporal lobe seizures even after separately analysing the left and right TLE patients

B.3 Computation of abnormality load

Figure B.3a-c We standardised (z-score) the FA weighted connectivity matrices for 60 FBTCS+ patients and 23 FBTCS- at each connection with respect to the corresponding connection distribution obtained from 29 controls. Mathematically, this can be represented as $\frac{(\mu_{ij}^{controls} - k_{ij}^{patient})}{\sigma_{ij}^{controls}}$, where $k_{ij}^{patient}$ is the FA of a connection between node i and j in patients, $\mu_{ij}^{controls}$ is the mean FA of connection between node i and j across controls, and $\sigma_{ij}^{controls}$ is the standard deviation of FA of connection between node i and j in controls. Figure B.3d shows the z-transformed connectivity matrices for FBTCS+ patients and Figure B.3e for FBTCS- patients. Note that majority of z scores in these standardised networks are positive, i.e. FA of connections in patients were abnormally reduced. Figure B.3f-g We computed node abnormality at every node (shown on the y-axis) as the ratio of total number of abnormal connections to the total number of connections at that node. We defined abnormal connections as those above a set z-score threshold (shown on the x-axis) ranging from 1.5 to 3.5 in steps of 0.1. Figure B.3f shows the node abnormality for FBTCS+ patients and Figure B.3g for the FBTCS- patients.

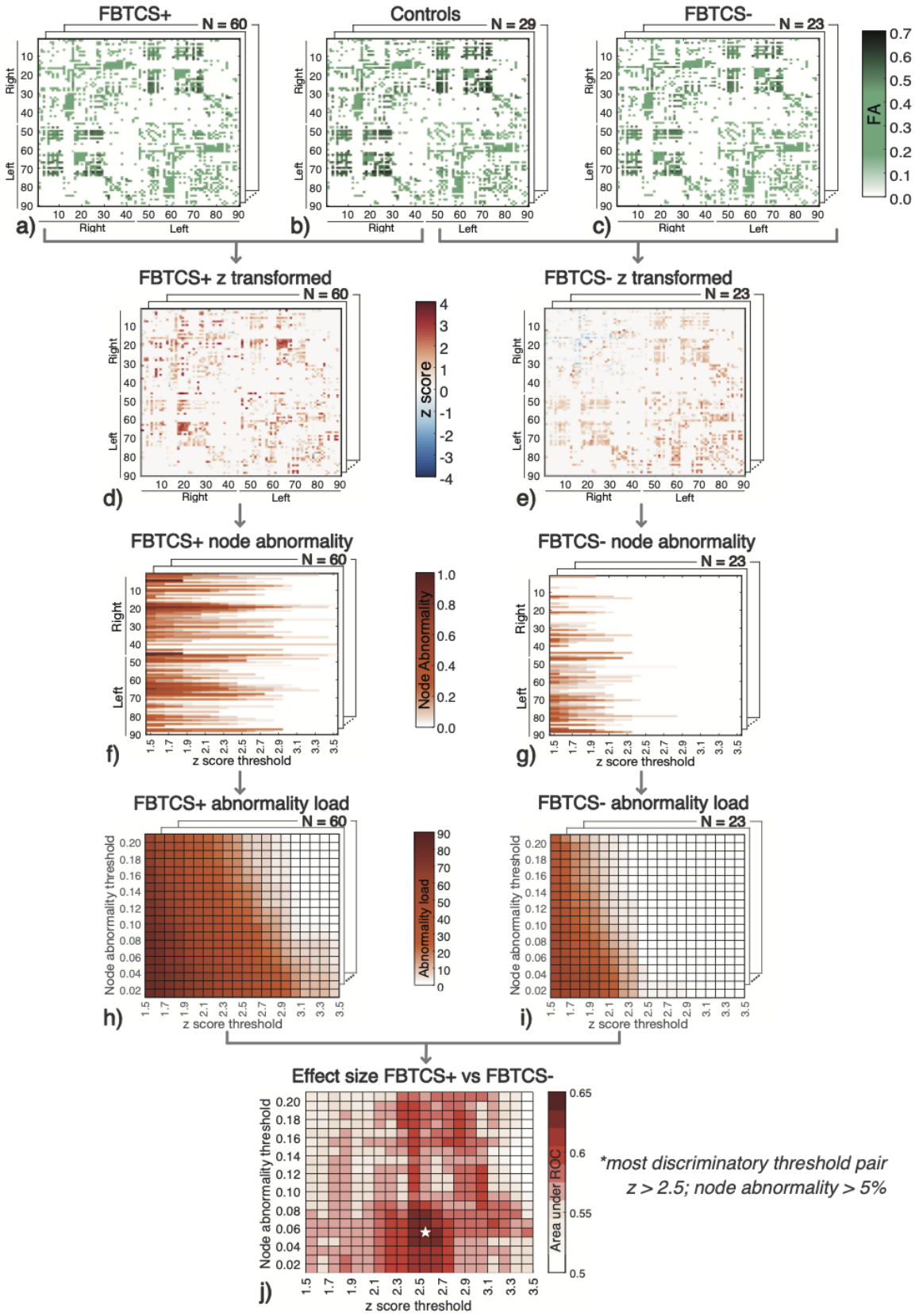

Fig. B.3 Computation of abnormality load

Figure B.3h-i We identified abnormal nodes as those with node abnormality above a set node abnormality threshold. Node abnormality thresholds (ranging from 0.01 to 0.20 in steps of 0.01) are shown on the y-axis corresponding to every z-score threshold shown on the x-axis. The range for z-score and node abnormality thresholds are empirically chosen. We restricted the maximum range for z-score at 3.5 and node abnormality at 0.2 because beyond these threshold values no to very few abnormal connections and nodes were detected in most patients. At every pair of node abnormality threshold and z-score threshold, we identified each node as normal (0) or abnormal (1). We defined abnormality load as the total number of abnormal nodes identified at each pair of thresholds. Abnormality load for FBTCS+ patients are shown in Figure B.3h and FBTCS- patients are shown in Figure B.3i. In Figure B.3j we computed the discrimination between FBTCS+ and FBTCS- patients at every threshold pair. Area under the receiver operator characteristic curve, a non-parametric measure of effect size, is plotted at every threshold pair. While high effect size (shown in red clusters) occurs at many threshold pairs, the star marks the threshold pair with the highest discrimination between FBTCS+ and FBTCS- patients.

B.4 Node abnormality between FBTCS+ and FBTCS-

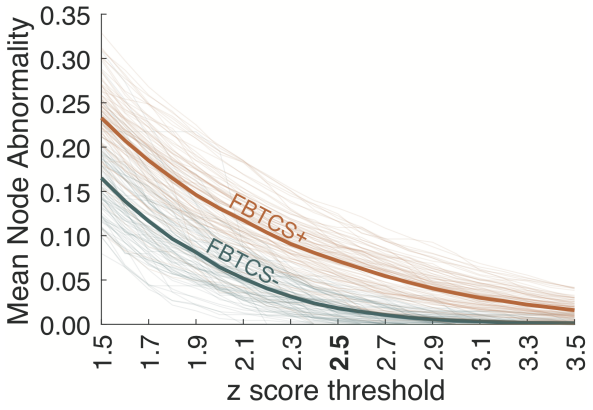

Fig. B.4 Mean node abnormality of FBTCS+ patient group is higher than FBTCS- patient group across the range of z-score threshold.

Solid line plots the mean node abnormality across all ROI in FBTCS+ and FBTCS- patient groups at different z-score thresholds. Shaded lines show the mean node abnormality for each ROI in FBTCS+ and FBTCS- group. Equivalent expanded figure at z-score threshold of 2.5 is detailed in Figure 3.4 of the manuscript.

Appendix C

IGE Supplementary

C.1 Connectometry analysis with seeding pre-defined regions of interest

In this section, we extend our connectometry results of Chapter 4 to all the pre-defined regions of interest (ROIs) in the JHU white matter atlas excluding the ROIs in cerebellum, brain-stem, and corpus callosum. The corpus callosum defined in the JHU atlas overlaps considerably with other ROIs, therefore, we instead chose corpus callosum ROIs from the freesurfer Destrieux atlas. Additionally, thalamus-proper ROI was chosen from the Destrieux atlas because it is not defined in the JHU white-matter atlas.

Connectometry analysis was repeated for each ROI set as seed. The pipeline followed is the same as described in Figure 4.1. All parameters and threshold used are also the same as described in Figure 4.1 and methods in Chapter 4. Results for each ROI are shown in Supplementary Figure C.1 (presented in three parts). Tracts with significantly reduced (increased) gFA in IGE patients are plotted for an example threshold value depicted in red (blue) star in Supplementary Figure C.1.

As shown in Supplementary Figure C.1 panel (a) to (i), we found that only the cortico-cortical tracts have significantly reduced gFA in IGE patients compared to controls. Additionally, a significant increase in gFA was detected for the cortico-thalamic tracts illustrated in Supplementary Figure C.1 panel (h) to (j). In panel (h) and (i), both significant increase and decrease were detected for the seed ROI shown. However, the tracts showing decrease are the

cortico-cortical tracts and increases are the cortico-thalamic tracts emanating via the seeded ROI. Seeding only the thalamic ROIs from the Destrieux atlas (Supplementary Figure C.1 panel (k)) makes it apparent that the cortico-thalamic tracts are increased in IGE patients. Note that in panel (k), in addition to the superior-inferior cortico-thalamic tracts shown in blue, we also detected a few additional tracts shown in red. These are the fornix tracts which are detected due to the partial overlap between the thalamic ROI defined in Destrieux atlas and fornix (seeding thalamus also seeds some parts of fornix). gFA of the fornix tract bundles by itself are not increased in the IGE patients compared to controls. Therefore, the abnormal increase in tract integrity of IGE patients is driven by the superior-inferior cortico-thalamic tracts shown in blue in Supplementary Figure C.1 panel (h)-(k). No significant increase or decrease in gFA was detected between IGE patients and controls for any tracts upon seeding the ROIs shown in panel (l)-(w). Colour coding of the tracts indicate direction as follows: red, left-right; green, anterior-posterior; blue, superior-inferior.

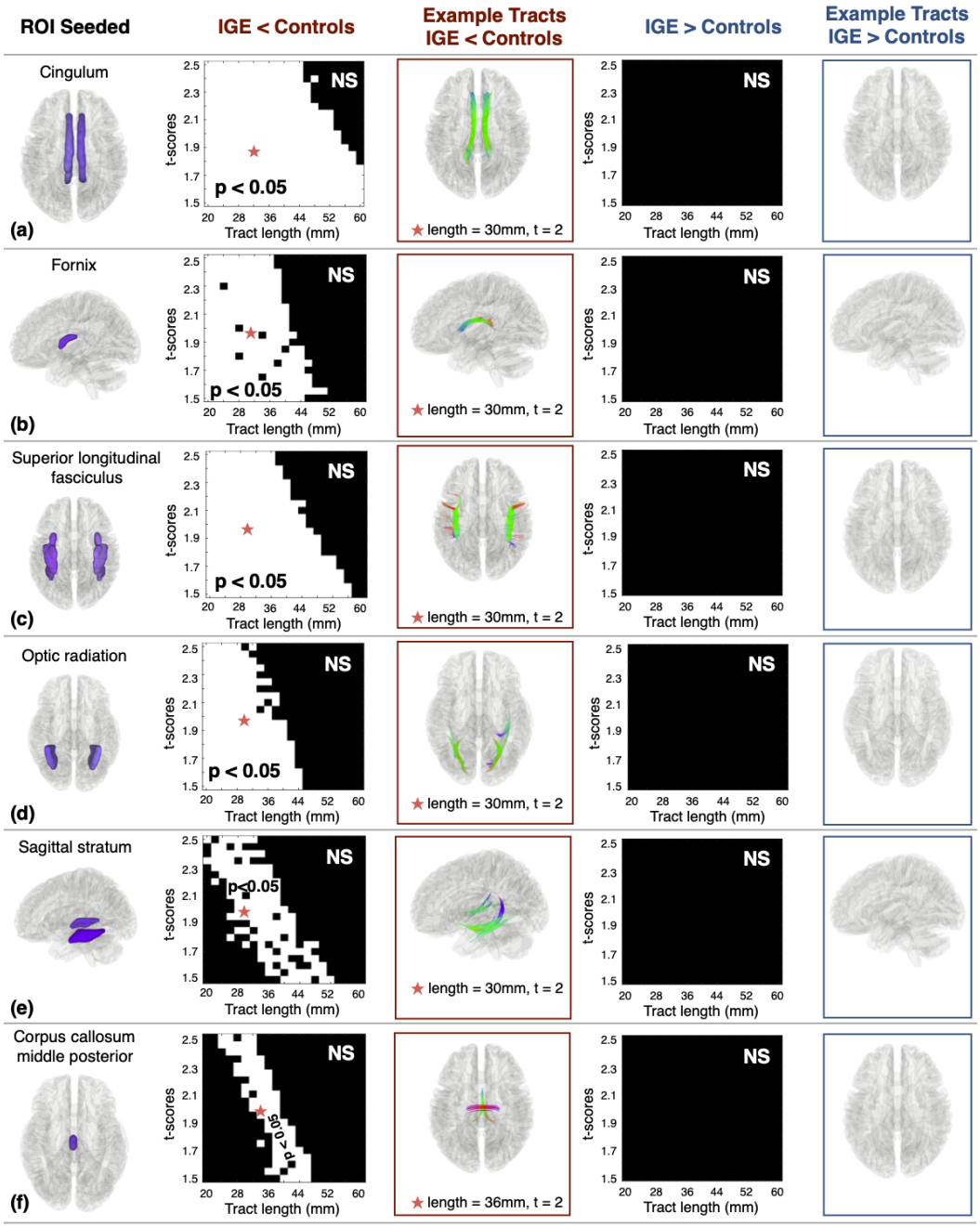

Fig. C.1 Connectometry analysis upon seeding pre-defined regions of interest *(part 1)*

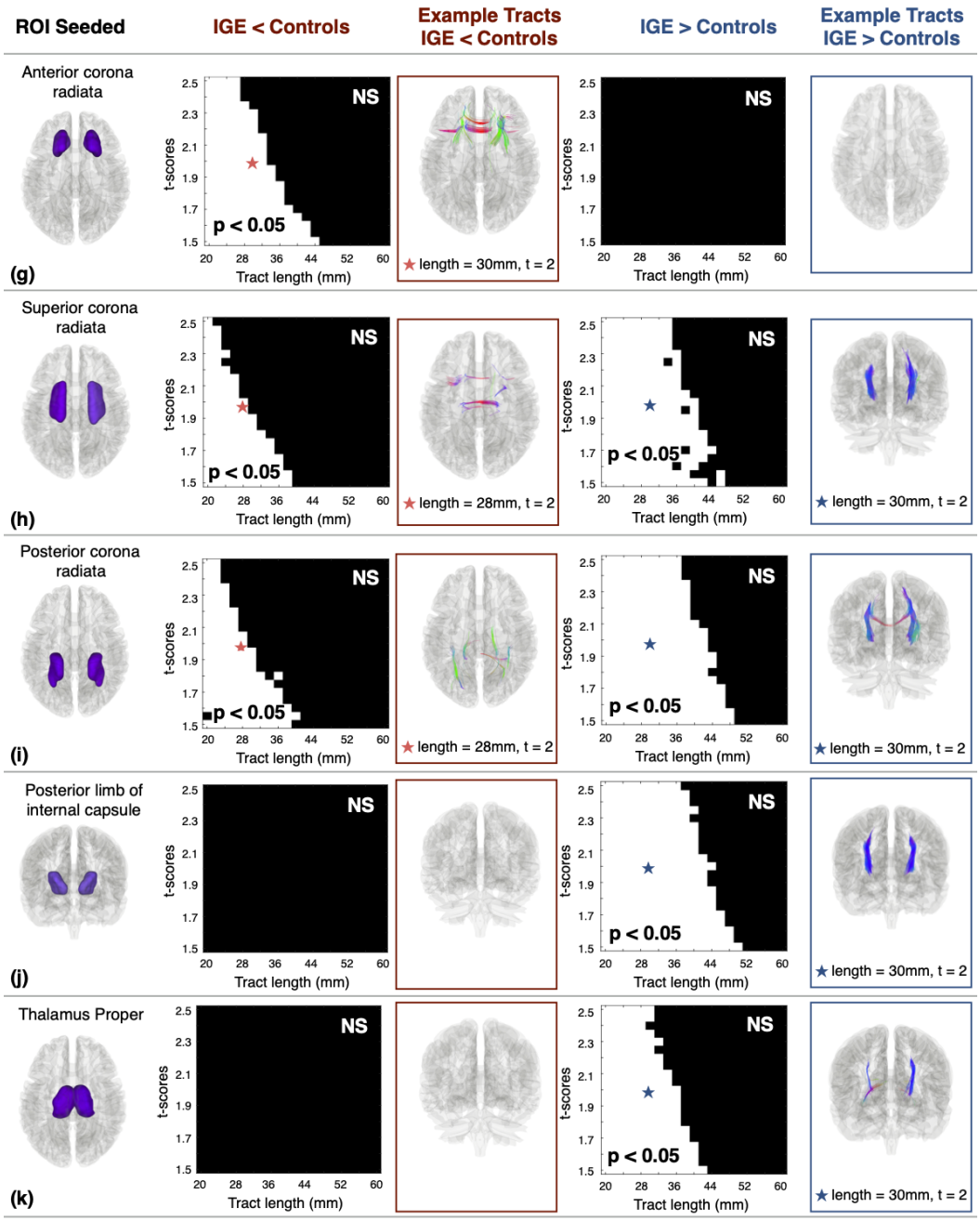

Fig. C.1 Connectometry analysis upon seeding pre-defined regions of interest *(part 2)*

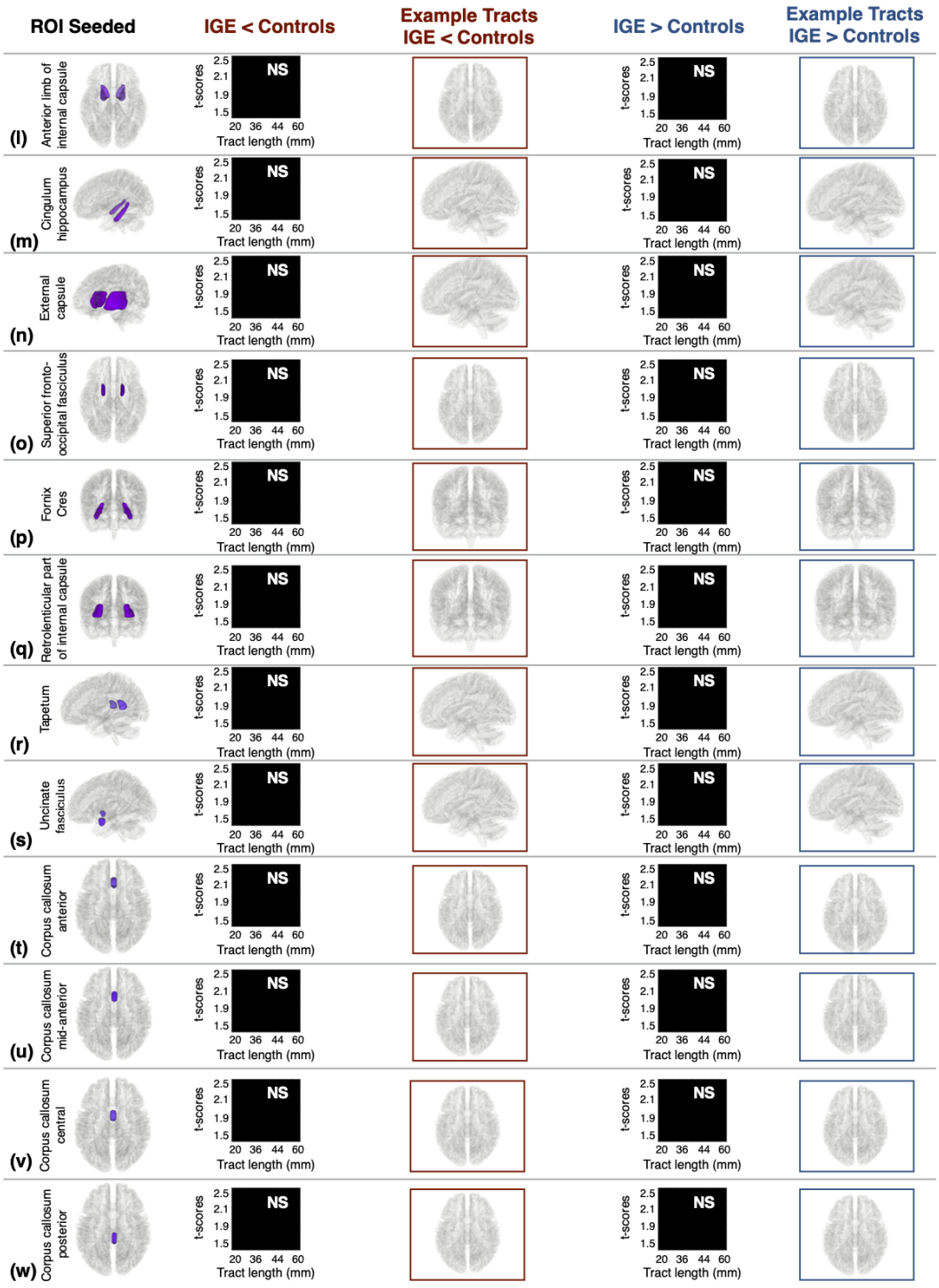

Fig. C.1 Connectometry analysis upon seeding pre-defined regions of interest *(part 3)*

C.2 Connectometry analysis upon seeding the whole brain

We seeded the whole brain in connectometry analysis to visualise the tracts with increased or decreased gFA between IGE patients and controls. As depicted by the white region in panel **(a)** and **(c)**, there indeed are tracts with significantly enhanced and reduced integrity. These tracts are visualised at exemplary pair of threshold values in panel **(b)** an **(d)**. Even though visually it may be difficult to attribute the specific tract bundles that may be driving the increases and decreases of mean gFA between patients and controls, consistent patterns are quite apparent. For example, at thresholds ($t = 2.2$, $l = 32mm$) in panel **(b)** cingulum, fornix, superior longitudinal fasciculus, and optic radiations are reduced, whereas for the same point in panel **(d)** cortico-thamic tracts are increased in IGE patients. These changes can, however, be quantified region specifically upon seeding the individual ROIs (c.f., Supplementary Figure C.1). Colour coding of the tracts indicate direction as follows: red, left-right; green, anterior-posterior; blue, superior-inferior.

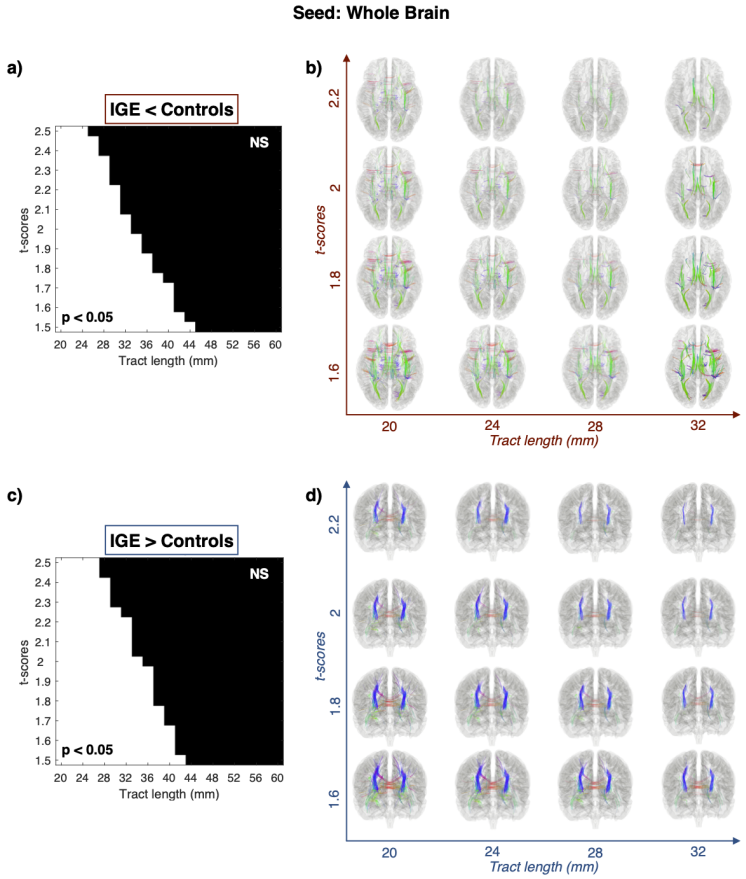

Fig. C.2 Connectometry analysis upon seeding the whole brain.

C.3 Thalamo-frontal white-matter integrity is preserved in IGE patients

Confirming the results in McGill et al. 2014, we also find that the thalamo-frontal white-matter connectivity is preserved in patients with IGE. End to end tracking was performed between thalamus and medial prefrontal cortex ROIs. The thalamo-frontal tracts delineated and the ROIs are shown on the brain schematic. Mean gFA residuals for voxels underlying the delineated thalamo-frontal tracts were compared between the patients and control groups. No significant difference was found in the delineated thalamo-frontal tract integrity. Colour coding of the tracts indicate direction as follows: red, left-right; green, anterior-posterior; blue, superior-inferior.

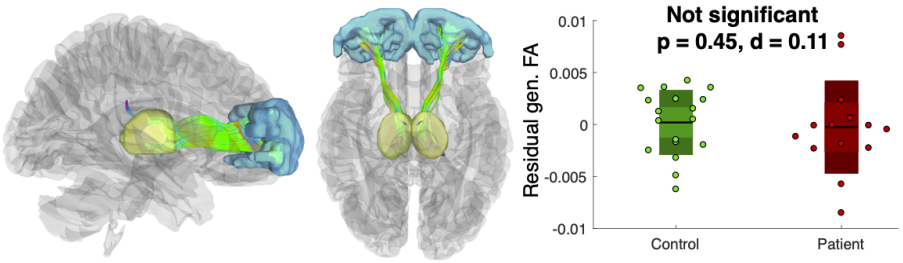

Fig. C.3 Thalamo-frontal white-matter integrity is preserved in IGE patients

C.4 Bifurcation diagram illustrating model dynamics

The fixed point dynamics (FPD) representing seizure free activity is shown in blue in panel **(e)**. The model is bistable in regions shown by panel **(d)**. This means that for those parameter conditions the dynamics can either be a fixed point or a spike-wave (SWD) - i.e. both states coexist. With parameter setting in panel **(c)**, the dynamics become monostable with only spike-wave. In panel **(b)**, the model captures a bistable spike-wave dynamics with fast oscillatory dynamics (OD). Finally, the model is also capable of capturing a monostable fast oscillatory dynamics shown in grey in panel **(a)**.

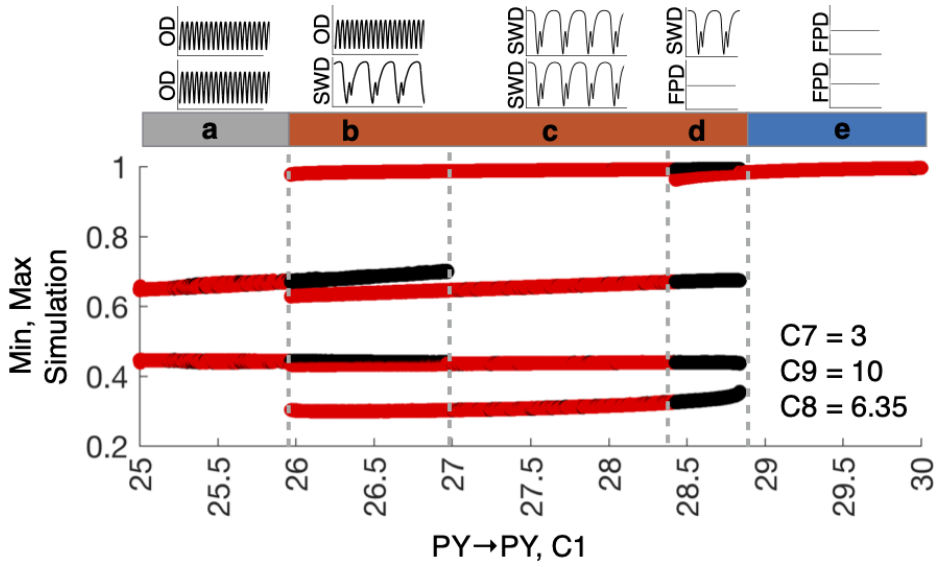

Fig. C.4 Bifurcation diagram illustrating detailed model dynamics.

C.5 Whole-tract based approach is less sensitive in detecting local changes

Panel **a)** to delineate the white-matter tracts in the default mode network (DMN), we incorporated the DMN cortical parcellation scheme estimated by (Yeo et al., 2011) and performed the conventional end-to-end tractography. As evident by the box plot, the residuals of gFA averaged across the entire tract profile in the DMN is lower in IGE patients, but not significantly different than controls ($p = 0.12, d = 0.438$). **b)** Similarly, by conventional end-to-end fibre tracking the cingulum tracts connecting posterior cingulate cortex (PCC) with the medial prefrontal cortex (MPFC) are delineated. The box plot illustrates that the gFA residuals averaged across these tracts are reduced in IGE patients, but not significantly different in statistical sense from the control population ($p = 0.09, d = 0.592$). Colour coding of the tracts indicate direction as follows: red, left-right; green, anterior-posterior; blue, superior-inferior.

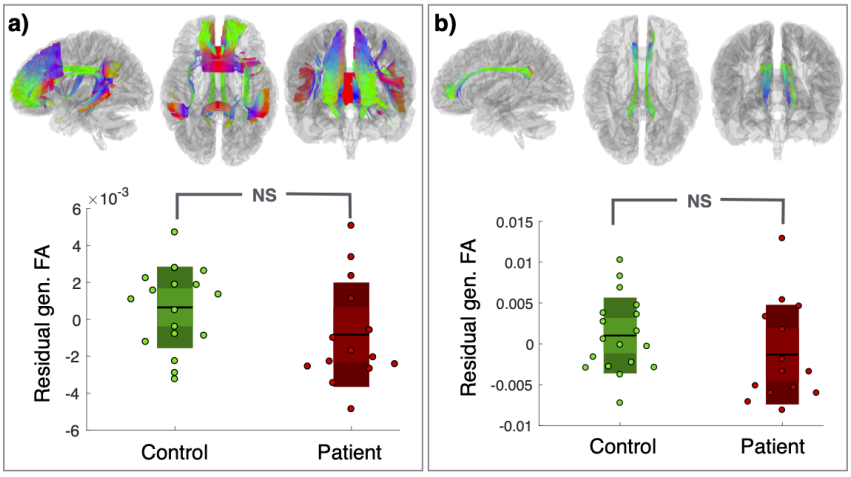

Fig. C.5 Whole-tract based approach is less sensitive in detecting significant regional differences in white matter structures.

C.6 Information on control subjects

Table C.1 Information on control subjects

Control	Gender	Age at MRI
1	Male	40.2
2	Female	35.2
3	Male	45.1
4	Female	25
5	Male	33.1
6	Female	20.9
7	Female	23.7
8	Male	33.3
9	Male	22.8
10	Female	30.5
11	Female	28.9
12	Male	26.9
13	Male	22.3
14	Female	21.7
15	Female	37
16	Female	46.5
17	Male	28.9
18	Male	21.6

C.7 Values of the parameters incorporated in the model

Table C.2 Values of the parameters incorporated in the model.

Parameter	Interpretation	Value
C1	PY→PY connectivity strength	Variable
C2	PY→IN connectivity strength	38
C3	IN→PY connectivity strength	25
C4	RE→RE connectivity strength	0.1
C5	TC→RE connectivity strength	2
C6	RE→TC connectivity strength	1
C7	PY→TC connectivity strength	Variable
C8	PY→RE connectivity strength	Variable
C9	TC→PY connectivity strength	Variable
τ_1	PY timescale	0.033
τ_2	IN timescale	0.013
τ_3	TC timescale	0.065
τ_4	RE timesclae	0.065
h_{py}	Input PY	-5
h_{in}	Input IN	-15
h_{tc}	Input TC	10
h_{re}	Input RE	5
θ	Sigmoid threshold	4
α	Sigmoid steepness	1

References

Abhinav, K., Yeh, F.-C., El-Dokla, A., Ferrando, L. M., Chang, Y.-F., Lacomis, D., Friedlander, R. M., and Fernandez-Miranda, J. C. (2014a). Use of diffusion spectrum imaging in preliminary longitudinal evaluation of amyotrophic lateral sclerosis: development of an imaging biomarker. *Frontiers in human neuroscience*, 8:270.

Abhinav, K., Yeh, F.-C., Pathak, S., Suski, V., Lacomis, D., Friedlander, R. M., and Fernandez-Miranda, J. C. (2014b). Advanced diffusion MRI fiber tracking in neurosurgical and neurodegenerative disorders and neuroanatomical studies: A review. *Biochimica et biophysica acta*, 1842(11):2286–2297.

Amari, S.-i. (1977). Dynamics of pattern formation in lateral-inhibition type neural fields. *Biological Cybernetics*, 27(2):77–87.

Andermann, F. and Berkovic, S. F. (2001). Idiopathic Generalized Epilepsy with Generalized and Other Seizures in Adolescence. *Epilepsia*, 42(3):317–320.

Andersson, J. L. R. and Sotiropoulos, S. N. (2016). An integrated approach to correction for off-resonance effects and subject movement in diffusion MR imaging. *NeuroImage*, 125:1063–1078.

Avoli, M. (2012). A brief history on the oscillating roles of thalamus and cortex in absence seizures. *Epilepsia*, 53(5):779–789.

Bagshaw, A. P., Hale, J. R., Campos, B. M., Rollings, D. T., Wilson, R. S., Alvim, M. K. M., Coan, A. C., and Cendes, F. (2017). Sleep onset uncovers thalamic abnormalities in patients with idiopathic generalised epilepsy. *NeuroImage: Clinical*, 16:52–57.

Baier, G., Goodfellow, M., Taylor, P. N., Wang, Y., and Garry, D. J. (2012). The importance of modeling epileptic seizure dynamics as spatio-temporal patterns. *Frontiers in Physiology*, 3:281.

Bassett, D. S. and Sporns, O. (2017). Network neuroscience. *Nature Neuroscience*, 20(3):353–364.

Baud, M. O., Kleen, J. K., Mirro, E. A., Andrechak, J. C., King-Stephens, D., Chang, E. F., and Rao, V. R. (2018). Multi-day rhythms modulate seizure risk in epilepsy. *Nature Communications*, 9(1):88.

Baud, M. O., Vulliemoz, S., and Seeck, M. (2015). Recurrent secondary generalization in frontal lobe epilepsy: Predictors and a potential link to surgical outcome? *Epilepsia*, 56(9):1454–1462.

Bauer, P. R., Thijs, R. D., Lamberts, R. J., Velis, D. N., Visser, G. H., Tolner, E. A., Sander, J. W., Silva, F. H. L. d., and Kalitzin, S. N. (2017). Dynamics of convulsive seizure termination and postictal generalized EEG suppression. *Brain*, page aww322.

Beenhakker, M. P. and Huguenard, J. R. (2009). Neurons that Fire Together Also Conspire Together: Is Normal Sleep Circuitry Hijacked to Generate Epilepsy? *Neuron*, 62(5):612–632.

Bell, G. S., Tisi, J. d., Gonzalez-Fraile, J. C., Peacock, J. L., McEvoy, A. W., Harkness, W. F. J., Foong, J., Pope, R. A., Diehl, B., Sander, J. W., and Duncan, J. S. (2017). Factors affecting seizure outcome after epilepsy surgery: an observational series. *Journal of Neurology, Neurosurgery & Psychiatry*, 88(11):933–940.

Benbadis, S. R. (2005). Practical Management Issues for Idiopathic Generalized Epilepsies. *Epilepsia*, 46(s9):125–132.

Benjamin, O., Fitzgerald, T. H., Ashwin, P., Tsaneva-Atanasova, K., Chowdhury, F., Richardson, M. P., and Terry, J. R. (2012). A phenomenological model of seizure initiation suggests network structure may explain seizure frequency in idiopathic generalised epilepsy. *The Journal of Mathematical Neuroscience*, 2(1):1.

Benjamini, Y. and Hochberg, Y. (1995). Controlling the False Discovery Rate: A Practical and Powerful Approach to Multiple Testing. *Journal of the Royal Statistical Society: Series B (Methodological)*, 57(1):289–300.

Berg, A. T., Berkovic, S. F., Brodie, M. J., Buchhalter, J., Cross, J. H., Boas, W. V. E., Engel, J., French, J., Glauser, T. A., Mathern, G. W., Moshé, S. L., Nordli, D., Plouin, P., and Scheffer, I. E. (2010). Revised terminology and concepts for organization of seizures and epilepsies: Report of the ILAE Commission on Classification and Terminology, 2005–2009. *Epilepsia*, 51(4):676–685.

Berg, A. T., Mathern, G. W., Bronen, R. A., Fulbright, R. K., DiMario, F., Testa, F. M., and Levy, S. R. (2009). Frequency, prognosis and surgical treatment of structural abnormalities seen with magnetic resonance imaging in childhood epilepsy. *Brain*, 132(10):2785–2797.

Bernasconi, A., Bernasconi, N., Natsume, J., Antel, S. B., Andermann, F., and Arnold, D. L. (2003). Magnetic resonance spectroscopy and imaging of the thalamus in idiopathic generalized epilepsy. *Brain*, 126(11):2447–2454.

Bernasconi, A., Cendes, F., Theodore, W. H., Gill, R. S., Koepp, M. J., Hogan, R. E., Jackson, G. D., Federico, P., Labate, A., Vaudano, A. E., Blümcke, I., Ryvlin, P., and Bernasconi, N. (2019). Recommendations for the use of structural magnetic resonance imaging in the care of patients with epilepsy: A consensus report from the International League Against Epilepsy Neuroimaging Task Force. *Epilepsia*, 60(6):1054–1068.

Bernhardt, B. C., Bonilha, L., and Gross, D. W. (2015). Network analysis for a network disorder: The emerging role of graph theory in the study of epilepsy. *Epilepsy & behavior : E&B*, 50:162–70.

Besson, P., Bandt, S. K., Proix, T., Lagarde, S., Jirsa, V. K., Ranjeva, J.-P., Bartolomei, F., and Guye, M. (2017). Anatomic consistencies across epilepsies: a stereotactic-EEG informed high-resolution structural connectivity study. *Brain*, 140(10):2639–2652.

Betzel, R. F., Medaglia, J. D., Kahn, A. E., Soffer, J., Schonhaut, D. R., and Bassett, D. S. (2019). Structural, geometric and genetic factors predict interregional brain connectivity patterns probed by electrocorticography. *Nature Biomedical Engineering*, 3(11):902–916.

Bhattacharya, B. S., Bond, T. P., O'Hare, L., Turner, D., and Durrant, S. J. (2016). Causal Role of Thalamic Interneurons in Brain State Transitions: A Study Using a Neural Mass Model Implementing Synaptic Kinetics. *Frontiers in Computational Neuroscience*, 10:115.

Blumenfeld, H. (2002). The Thalamus and Seizures. *Archives of Neurology*, 59(1):135–137.

Blumenfeld, H. (2003). From Molecules to Networks: Cortical/Subcortical Interactions in the Pathophysiology of Idiopathic Generalized Epilepsy. *Epilepsia*, 44(s2):7–15.

Blumenfeld, H., Varghese, G. I., Purcaro, M. J., Motelow, J. E., Enev, M., McNally, K. A., Levin, A. R., Hirsch, L. J., Tikofsky, R., Zubal, I. G., Paige, A. L., and Spencer, S. S. (2009). Cortical and subcortical networks in human secondarily generalized tonic–clonic seizures. *Brain*, 132(4):999–1012.

Bone, B., Fogarasi, A., Schulz, R., Gyimesi, C., Kalmar, Z., Kovacs, N., Ebner, A., and Janszky, J. (2012). Secondarily generalized seizures in temporal lobe epilepsy: Secondarily Generalized Seizures. *Epilepsia*, 53(5):817–824.

Bonilha, L., Helpern, J. A., Sainju, R., Nesland, T., Edwards, J. C., Glazier, S. S., and Tabesh, A. (2013). Presurgical connectome and postsurgical seizure control in temporal lobe epilepsy. *Neurology*, 81(19):1704–1710.

Bonilha, L., Jensen, J. H., Baker, N., Breedlove, J., Nesland, T., Lin, J. J., Drane, D. L., Saindane, A. M., Binder, J. R., and Kuzniecky, R. I. (2015). The brain connectome as a personalized biomarker of seizure outcomes after temporal lobectomy. *Neurology*, 84(18):1846–1853.

Bonilha, L. and Keller, S. S. (2015). Quantitative MRI in refractory temporal lobe epilepsy: relationship with surgical outcomes. *Quantitative imaging in medicine and surgery*, 5(2):204–24.

Bonilha, L., Martz, G. U., Glazier, S. S., and Edwards, J. C. (2011). Subtypes of medial temporal lobe epilepsy: influence on temporal lobectomy outcomes? *Epilepsia*, 53(1):1–6.

Borisyuk, G. N., Borisyuk, R. M., Khibnik, A. I., and Roose, D. (1995). Dynamics and bifurcations of two coupled neural oscillators with different connection types. *Bulletin of Mathematical Biology*, 57(6):809–840.

Borisyuk, R. M. and Kirillov, A. B. (1992). Bifurcation analysis of a neural network model. *Biological Cybernetics*, 66(4):319–325.

Breakspear, M., Roberts, J. A., Terry, J. R., Rodrigues, S., Mahant, N., and Robinson, P. A. (2006). A Unifying Explanation of Primary Generalized Seizures Through Nonlinear Brain Modeling and Bifurcation Analysis. *Cerebral Cortex*, 16(9):1296–1313.

Brodie, M. J., Barry, S. J. E., Bamagous, G. A., Norrie, J. D., and Kwan, P. (2012). Patterns of treatment response in newly diagnosed epilepsy. *Neurology*, 78(20):1548–1554.

Brodovskaya, A. and Kapur, J. (2019). Circuits generating secondarily generalized seizures. *Epilepsy & Behavior*, 101(xxxx):106474.

Caciagli, L., Allen, L. A., He, X., Trimmel, K., Vos, S. B., Centeno, M., Galovic, M., Sidhu, M. K., Thompson, P. J., Bassett, D. S., Winston, G. P., Duncan, J. S., Koepp, M. J., and Sperling, M. R. (2020). Thalamus and focal to bilateral seizures: A multi-scale cognitive imaging study. *Neurology*, page 10.1212/WNL.0000000000010645.

Chen, C., Li, H., Ding, F., Yang, L., Huang, P., Wang, S., Jin, B., Xu, C., Wang, Y., Ding, M., Chen, Z., and Wang, S. (2018). Alterations in the hippocampal-thalamic pathway underlying secondarily generalized tonic-clonic seizures in mesial temporal lobe epilepsy: A diffusion tensor imaging study. *Epilepsia*, 60(1):121–130.

Chen, M., Guo, D., Xia, Y., and Yao, D. (2017). Control of Absence Seizures by the Thalamic Feed-Forward Inhibition. *Frontiers in Computational Neuroscience*, 11:31.

Chu, C. J., Tanaka, N., Diaz, J., Edlow, B. L., Wu, O., Hämäläinen, M., Stufflebeam, S., Cash, S. S., and Kramer, M. A. (2014). EEG functional connectivity is partially predicted by underlying white matter connectivity. *NeuroImage*, 108:23–33.

Cohen, J. (1988). Statistical Power Analysis for the Behavioral Sciences.

Cohen-Gadol, A. A., Wilhelmi, B. G., Collignon, F., White, J. B., Britton, J. W., Cambier, D. M., Christianson, T. J. H., Marsh, W. R., Meyer, F. B., and Cascino, G. D. (2006). Long-term outcome of epilepsy surgery among 399 patients with nonlesional seizure foci including mesial temporal lobe sclerosis. *Journal of Neurosurgery*, 104(4):513–524.

Concha, L., Kim, H., Bernasconi, A., Bernhardt, B. C., and Bernasconi, N. (2012). Spatial patterns of water diffusion along white matter tracts in temporal lobe epilepsy. *Neurology*, 79(5):455–462.

Cook, P. A., Symms, M., Boulby, P. A., and Alexander, D. C. (2007). Optimal acquisition orders of diffusion-weighted MRI measurements. *Journal of Magnetic Resonance Imaging*, 25(5):1051–1058.

Dabrowska, N., Joshi, S., Williamson, J., Lewczuk, E., Lu, Y., Oberoi, S., Brodovskaya, A., and Kapur, J. (2019). Parallel pathways of seizure generalization. *Brain*, 142(8):2336–2351.

Deleo, F., Thom, M., Concha, L., Bernasconi, A., Bernhardt, B. C., and Bernasconi, N. (2018). Histological and MRI markers of white matter damage in focal epilepsy. *Epilepsy Research*, 140:29–38.

Deppe, M., Kellinghaus, C., Duning, T., Möddel, G., Mohammadi, S., Deppe, K., Schiffbauer, H., Kugel, H., Keller, S. S., Ringelstein, E. B., and Knecht, S. (2008). Nerve fiber impairment of anterior thalamocortical circuitry in juvenile myoclonic epilepsy. *Neurology*, 71(24):1981–1985.

Destexhe, A. (1998). Spike-and-Wave Oscillations Based on the Properties of GABAB Receptors. *Journal of Neuroscience*, 18(21):9099–9111.

Destexhe, A. and Sejnowski, T. J. (2009). The Wilson–Cowan model, 36 years later. *Biological Cybernetics*, 101(1):1–2.

Devinsky, O., Hesdorffer, D. C., Thurman, D. J., Lhatoo, S., and Richerson, G. (2016). Sudden unexpected death in epilepsy: epidemiology, mechanisms, and prevention. *The Lancet. Neurology*, 15(10):1075–88.

Duncan, J. S. (2005). Brain Imaging in Idiopathic Generalized Epilepsies. *Epilepsia*, 46(s9):108–111.

Duncan, J. S., Winston, G. P., Koepp, M. J., and Ourselin, S. (2016). Brain imaging in the assessment for epilepsy surgery. *The Lancet Neurology*, 15(4):420–433.

Enatsu, R., Jin, K., Elwan, S., Kubota, Y., Piao, Z., O'Connor, T., Horning, K., Burgess, R. C., Bingaman, W., and Nair, D. R. (2012). Correlations between ictal propagation and response to electrical cortical stimulation: a cortico-cortical evoked potential study. *Epilepsy research*, 101(1-2):76–87.

Englot, D. J., Hinkley, L. B., Kort, N. S., Imber, B. S., Mizuiri, D., Honma, S. M., Findlay, A. M., Garrett, C., Cheung, P. L., Mantle, M., Tarapore, P. E., Knowlton, R. C., Chang, E. F., Kirsch, H. E., and Nagarajan, S. S. (2015). Global and regional functional connectivity maps of neural oscillations in focal epilepsy. *Brain*, 138(8):2249–2262.

Englot, D. J., Morgan, V. L., and Chang, C. (2020). Impaired vigilance networks in temporal lobe epilepsy: Mechanisms and clinical implications. *Epilepsia*, 61(2):189–202.

Englot, D. J., Rolston, J. D., Wright, C. W., Hassnain, K. H., and Chang, E. F. (2016). Rates and predictors of seizure freedom with vagus nerve stimulation for intractable epilepsy. *Neurosurgery*, 79(3):345–353.

Fagerholm, E. D., Hellyer, P. J., Scott, G., Leech, R., and Sharp, D. J. (2015). Disconnection of network hubs and cognitive impairment after traumatic brain injury. *Brain*, 138(6):1696–1709.

Fairclough, S., O'Keeffe, A. G., Tisi, J. d., and Duncan, J. S. (2017). Auras and the risk of seizures with impaired consciousness following epilepsy surgery: implications for driving. *Journal of Neurology, Neurosurgery & Psychiatry*, 89(6):599–602.

Fan, D., Liao, F., and Wang, Q. (2017). The pacemaker role of thalamic reticular nucleus in controlling spike-wave discharges and spindles. *Chaos: An Interdisciplinary Journal of Nonlinear Science*, 27(7):073103.

Fan, D., Liu, S., and Wang, Q. (2016). Stimulus-induced Epileptic Spike-Wave Discharges in Thalamocortical Model with Disinhibition. *Scientific Reports*, 6(1):37703.

Faraji, A. H., Abhinav, K., Jarbo, K., Yeh, F.-C., Shin, S. S., Pathak, S., Hirsch, B. E., Schneider, W., Fernandez-Miranda, J. C., and Friedlander, R. M. (2015). Longitudinal evaluation of corticospinal tract in patients with resected brainstem cavernous malformations using high-definition fiber tractography and diffusion connectometry analysis: preliminary experience. *Journal of neurosurgery*, 123(5):1133–44.

Fenichel, N. (1979). Geometric singular perturbation theory for ordinary differential equations. *Journal of Differential Equations*, 31(1):53–98.

Fiest, K. M., Sauro, K. M., Wiebe, S., Patten, S. B., Kwon, C.-S., Dykeman, J., Pringsheim, T., Lorenzetti, D. L., and Jetté, N. (2016). Prevalence and incidence of epilepsy: A systematic review and meta-analysis of international studies. *Neurology*, 88(3):296–303.

Fisher, R. S., Cross, J. H., French, J. A., Higurashi, N., Hirsch, E., Jansen, F. E., Lagae, L., Moshé, S. L., Peltola, J., Perez, E. R., Scheffer, I. E., and Zuberi, S. M. (2017). Operational classification of seizure types by the International League Against Epilepsy: Position Paper of the ILAE Commission for Classification and Terminology. *Epilepsia*, 58(4):522–530.

Focke, N. K., Diederich, C., Helms, G., Nitsche, M. A., Lerche, H., and Paulus, W. (2013). Idiopathic-generalized epilepsy shows profound white matter diffusion-tensor imaging alterations: Diffusion Tensor Alterations in Generalized Epilepsy. *Human Brain Mapping*, 35(7):3332–3342.

Frauscher, B., Ellenrieder, N. v., Zelmann, R., Doležalová, I., Minotti, L., Olivier, A., Hall, J., Hoffmann, D., Nguyen, D. K., Kahane, P., Dubeau, F., and Gotman, J. (2018). Atlas of the normal intracranial electroencephalogram: neurophysiological awake activity in different cortical areas. *Brain*, 141(4):1130–1144.

Fuentealba, P. and Steriade, M. (2005). The reticular nucleus revisited: Intrinsic and network properties of a thalamic pacemaker. *Progress in Neurobiology*, 75(2):125–141.

Gleichgerrcht, E., Keller, S. S., Drane, D. L., Munsell, B. C., Davis, K. A., Kaestner, E., Weber, B., Krantz, S., Vandergrift, W. A., Edwards, J. C., McDonald, C. R., Kuzniecky, R., and Bonilha, L. (2020). Temporal lobe epilepsy surgical outcomes can be inferred based on structural connectome hubs: a machine learning study. *Annals of Neurology*.

Gleichgerrcht, E., Munsell, B., Bhatia, S., Vandergrift, W. A., Rorden, C., McDonald, C., Edwards, J., Kuzniecky, R., and Bonilha, L. (2018). Deep learning applied to whole-brain connectome to determine seizure control after epilepsy surgery. *Epilepsia*, 59(9):1643–1654.

Gloor, P. (1979). Generalized Epilepsy with Spike-and-Wave Discharge: A Reinterpretation of Its Electrographic and Clinical Manifestations1. *Epilepsia*, 20(5):571–588.

Gong, J., Chang, X., Jiang, S., Klugah-Brown, B., Tan, S., Yao, D., and Luo, C. (2017). Microstructural alterations of white matter in juvenile myoclonic epilepsy. *Epilepsy Research*, 135:1–8.

Goni, J., Heuvel, M. P. v. d., Avena-Koenigsberger, A., Mendizabal, N. V. d., Betzel, R. F., Griffa, A., Hagmann, P., Corominas-Murtra, B., Thiran, J. P., and Sporns, O. (2013). Resting-brain functional connectivity predicted by analytic measures of network communication. *Proceedings of the National Academy of Sciences*, 111(2):833–838.

Goodfellow, M., Rummel, C., Abela, E., Richardson, M. P., Schindler, K., and Terry, J. R. (2016). Estimation of brain network ictogenicity predicts outcome from epilepsy surgery. *Scientific reports*, 6(1):29215.

Goodfellow, M., Schindler, K., and Baier, G. (2011). Intermittent spike–wave dynamics in a heterogeneous, spatially extended neural mass model. *NeuroImage*, 55(3):920–932.

Gotman, J., Grova, C., Bagshaw, A., Kobayashi, E., Aghakhani, Y., and Dubeau, F. (2005). Generalized epileptic discharges show thalamocortical activation and suspension of the default state of the brain. *Proceedings of the National Academy of Sciences of the United States of America*, 102(42):15236–15240.

Groppa, S., Moeller, F., Siebner, H., Wolff, S., Riedel, C., Deuschl, G., Stephani, U., and Siniatchkin, M. (2012). White matter microstructural changes of thalamocortical networks in photosensitivity and idiopathic generalized epilepsy: DTI of PPR and IGE. *Epilepsia*, 53(4):668–676.

Guyon, I. and Elisseeff, A. (2003). An Introduction to Variable and Feature Selection. *Journal of Machine Learning Research*, 3:1157—1182.

Guyon, I., Weston, J., Barnhill, S., and Vapnik, V. (2002). Gene Selection for Cancer Classification using Support Vector Machines. *Machine Learning*, 46(1/3):389–422.

Haneef, Z., Stern, J., Dewar, S., and Engel, J. (2010). Referral pattern for epilepsy surgery after evidence-based recommendations: A retrospective study. *Neurology*, 75(8):699–704.

Harden, C., Tomson, T., Gloss, D., Buchhalter, J., Cross, J. H., Donner, E., French, J. A., Gil-Nagel, A., Hesdorffer, D. C., Smithson, W. H., Spitz, M. C., Walczak, T. S., Sander, J. W., and Ryvlin, P. (2017). Practice guideline summary: Sudden unexpected death in epilepsy incidence rates and risk factors: Report of the Guideline Development, Dissemination, and Implementation Subcommittee of the American Academy of Neurology and the American Epilepsy Society. *Neurology*, 88(17):1674–1680.

Hatton, S. N., Huynh, K. H., Bonilha, L., Abela, E., Alhusaini, S., Altmann, A., Alvim, M. K. M., Balachandra, A. R., Bartolini, E., Bender, B., Bernasconi, N., Bernasconi, A., Bernhardt, B., Bargallo, N., Caldairou, B., Caligiuri, M. E., Carr, S. J. A., Cavalleri, G. L., Cendes, F., Concha, L., Davoodi-bojd, E., Desmond, P. M., Devinsky, O., Doherty, C. P., Domin, M., Duncan, J. S., Focke, N. K., Foley, S. F., Gambardella, A., Gleichgerrcht, E., Guerrini, R., Hamandi, K., Ishikawa, A., Keller, S. S., Kochunov, P. V., Kotikalapudi, R., Kreilkamp, B. A. K., Kwan, P., Labate, A., Langner, S., Lenge, M., Liu, M., Lui, E., Martin, P., Mascalchi, M., Moreira, J. C. V., Morita-Sherman, M. E., O'Brien, T. J., Pardoe, H. R., Pariente, J. C., Ribeiro, L. F., Richardson, M. P., Rocha, C. S., Rodríguez-Cruces, R., Rosenow, F., Severino, M., Sinclair, B., Soltanian-Zadeh, H., Striano, P., Taylor, P. N., Thomas, R. H., Tortora, D., Velakoulis, D., Vezzani, A., Vivash, L., Podewils, F. v., Vos, S. B., Weber, B., Winston, G. P., Yasuda, C. L., Zhu, A. H., Thompson, P. M., Whelan, C. D., Jahanshad, N., Sisodiya, S. M., and McDonald, C. R. (2020). White matter abnormalities across different epilepsy syndromes in adults: an ENIGMA-Epilepsy study. *Brain*.

He, X., Chaitanya, G., Asma, B., Caciagli, L., Bassett, D. S., Tracy, J. I., and Sperling, M. R. (2019). Disrupted basal ganglia–thalamocortical loops in focal to bilateral tonic-clonic seizures. *Brain*, 143(1):175–190.

He, X., Doucet, G. E., Sperling, M., Sharan, A., and Tracy, J. I. (2015). Reduced thalamocortical functional connectivity in temporal lobe epilepsy. *Epilepsia*, 56(10):1571—1579.

Hemery, C., Ryvlin, P., and Rheims, S. (2014). Prevention of generalized tonic-clonic seizures in refractory focal epilepsy: A meta-analysis. *Epilepsia*, 55(11):1789–1799.

Heuvel, M. P. v. d., Mandl, R. C., Kahn, R. S., and Pol, H. E. H. (2009). Functionally linked resting-state networks reflect the underlying structural connectivity architecture of the human brain. *Human Brain Mapping*, 30(10):3127–3141.

Higham, D. J. (2001). An Algorithmic Introduction to Numerical Simulation of Stochastic Differential Equations. *SIAM Review*, 43(3):525–546.

Ho, J., Tumkaya, T., Aryal, S., Choi, H., and Claridge-Chang, A. (2019). Moving beyond P values: data analysis with estimation graphics. *Nature Methods*, 16(7):565–566.

Honey, C. J., Sporns, O., Cammoun, L., Gigandet, X., Thiran, J. P., Meuli, R., and Hagmann, P. (2009). Predicting human resting-state functional connectivity from structural connectivity. *Proceedings of the National Academy of Sciences*, 106(6):2035–2040.

Huguenard, J. R. and McCormick, D. A. (2007). Thalamic synchrony and dynamic regulation of global forebrain oscillations. *Trends in Neurosciences*, 30(7):350–356.

Izhikevich, E. M. (2006). Dynamical Systems in Neuroscience.

Janszky, J., Janszky, I., Schulz, R., Hoppe, M., Behne, F., Pannek, H. W., and Ebner, A. (2004). Temporal lobe epilepsy with hippocampal sclerosis: predictors for long-term surgical outcome. *Brain*, 128(2):395–404.

Jehi, L. (2020). Algorithms in clinical epilepsy practice: Can they really help us predict epilepsy outcomes? *Epilepsia*.

Jehi, L., Yardi, R., Chagin, K., Tassi, L., Russo, G. L., Worrell, G., Hu, W., Cendes, F., Morita, M., Bartolomei, F., Chauvel, P., Najm, I., Gonzalez-Martinez, J., Bingaman, W., and Kattan, M. W. (2015). Development and validation of nomograms to provide individualised predictions of seizure outcomes after epilepsy surgery: a retrospective analysis. *The Lancet Neurology*, 14(3):283–290.

Jenkinson, M., Beckmann, C. F., Behrens, T. E. J., Woolrich, M. W., and Smith, S. M. (2012). FSL. *NeuroImage*, 62(2):782–790.

Ji, G.-J., Zhang, Z., Xu, Q., Wei, W., Wang, J., Wang, Z., Yang, F., Sun, K., Jiao, Q., Liao, W., and Lu, G. (2015). Connectome Reorganization Associated With Surgical Outcome in Temporal Lobe Epilepsy. *Medicine*, 94(40):e1737.

Ji, G.-J., Zhang, Z., Xu, Q., Zang, Y.-F., Liao, W., and Lu, G. (2014). Generalized Tonic-Clonic Seizures: Aberrant Interhemispheric Functional and Anatomical Connectivity. *Radiology*, 271(3):839–847.

Jiang, H., Zijl, P. C. v., Kim, J., Pearlson, G. D., and Mori, S. (2006). DtiStudio: Resource program for diffusion tensor computation and fiber bundle tracking. *Computer Methods and Programs in Biomedicine*, 81(2):106–116.

Jirsa, V. K., Proix, T., Perdikis, D., Woodman, M. M., Wang, H., Gonzalez-Martinez, J., Bernard, C., Bénar, C., Guye, M., Chauvel, P., and Bartolomei, F. (2016). The Virtual Epileptic Patient: Individualized whole-brain models of epilepsy spread. *NeuroImage*, 145(Pt B):377–388.

Jirsa, V. K., Stacey, W. C., Quilichini, P. P., Ivanov, A. I., and Bernard, C. (2014). On the nature of seizure dynamics. *Brain*, 137(8):2210–2230.

Jobst, B. C. and Cascino, G. D. (2015). Resective Epilepsy Surgery for Drug-Resistant Focal Epilepsy: A Review. *JAMA*, 313(3):285.

Jobst, B. C., Williamson, P. D., Neuschwander, T. B., Darcey, T. M., Thadani, V. M., and Roberts, D. W. (2001). Secondarily Generalized Seizures in Mesial Temporal Epilepsy: Clinical Characteristics, Lateralizing Signs, and Association With Sleep–Wake Cycle. *Epilepsia*, 42(10):1279–1287.

Juarez-Garcia, A., Stokes, T., Shaw, B., Camosso-Stefinovic, J., and Baker, R. (2006). The costs of epilepsy misdiagnosis in England and Wales. *Seizure*, 15(8):598–605.

Karoly, P. J., Goldenholz, D. M., Freestone, D. R., Moss, R. E., Grayden, D. B., Theodore, W. H., and Cook, M. J. (2018). Circadian and circaseptan rhythms in human epilepsy: a retrospective cohort study. *The Lancet Neurology*, 17(11):977–985.

Karthick, P. A., Tanaka, H., Khoo, H. M., and Gotman, J. (2018). Prediction of secondary generalization from a focal onset seizure in intracerebral EEG. *Clinical Neurophysiology*, 129(5):1030–1040.

Keller, S. S., Ahrens, T., Mohammadi, S., Möddel, G., Kugel, H., Ringelstein, E. B., and Deppe, M. (2011). Microstructural and volumetric abnormalities of the putamen in juvenile myoclonic epilepsy: DTI of JME. *Epilepsia*, 52(9):1715–1724.

Keller, S. S., Glenn, G. R., Weber, B., Kreilkamp, B. A. K., Jensen, J. H., Helpern, J. A., Wagner, J., Barker, G. J., Richardson, M. P., and Bonilha, L. (2016). Preoperative automated fibre quantification predicts postoperative seizure outcome in temporal lobe epilepsy. *Brain : a journal of neurology*, 140(Pt 1):68–82.

Keller, S. S., Richardson, M. P., Schoene-Bake, J.-C., O'Muircheartaigh, J., Elkommos, S., Kreilkamp, B., Goh, Y. Y., Marson, A. G., Elger, C., and Weber, B. (2015). Thalamotemporal alteration and postoperative seizures in temporal lobe epilepsy: MRI and Outcome in Epilepsy. *Annals of Neurology*, 77(5):760–774.

Keller, S. S. and Roberts, N. (2007). Voxel-based morphometry of temporal lobe epilepsy: an introduction and review of the literature. *Epilepsia*, 49(5):741–57.

Khambhati, A. N., Davis, K. A., Lucas, T. H., Litt, B., and Bassett, D. S. (2016). Virtual Cortical Resection Reveals Push-Pull Network Control Preceding Seizure Evolution. *Neuron*, 91(5):1170–82.

Kim, J. B., Suh, S.-i., Seo, W.-K., Oh, K., Koh, S.-B., and Kim, J. H. (2014). Altered thalamocortical functional connectivity in idiopathic generalized epilepsy. *Epilepsia*, 55(4):592–600.

Kini, L. G., Bernabei, J. M., Mikhail, F., Hadar, P., Shah, P., Khambhati, A. N., Oechsel, K., Archer, R., Boccanfuso, J., Conrad, E., Shinohara, R. T., Stein, J. M., Das, S., Kheder, A., Lucas, T. H., Davis, K. A., Bassett, D. S., and Litt, B. (2019). Virtual resection predicts surgical outcome for drug-resistant epilepsy. *Brain : a journal of neurology*, 142(12):3892–3905. Relate the effects of local stimulation to regional control centrality.

Kramer, M. A., Truccolo, W., Eden, U. T., Lepage, K. Q., Hochberg, L. R., Eskandar, E. N., Madsen, J. R., Lee, J. W., Maheshwari, A., Halgren, E., Chu, C. J., and Cash, S. S. (2012). Human seizures self-terminate across spatial scales via a critical transition. *Proceedings of the National Academy of Sciences*, 109(51):21116–21121.

Kuhlmann, L., Lehnertz, K., Richardson, M. P., Schelter, B., and Zaveri, H. P. (2018). Seizure prediction - ready for a new era. *Nature reviews. Neurology*, 14(10):618–630.

Lacey, C. J., Bryant, A., Brill, J., and Huguenard, J. R. (2012). Enhanced NMDA Receptor-Dependent Thalamic Excitation and Network Oscillations in Stargazer Mice. *The Journal of Neuroscience*, 32(32):11067–11081.

Lagarde, S., Roehri, N., Lambert, I., Trebuchon, A., McGonigal, A., Carron, R., Scavarda, D., Milh, M., Pizzo, F., Colombet, B., Giusiano, B., Villalon, S. M., Guye, M., Bénar, C.-G., and Bartolomei, F. (2018). Interictal stereotactic-EEG functional connectivity in refractory focal epilepsies. *Brain : a journal of neurology*, 141(10):2966–2980.

Langfitt, J. T. and Wiebe, S. (2008). Early surgical treatment for epilepsy. *Current opinion in neurology*, 21(2):179–83.

Larivière, S., Bernasconi, A., Bernasconi, N., and Bernhardt, B. C. (2020a). Connectome biomarkers of drug-resistant epilepsy. *Epilepsia*.

Larivière, S., Rodríguez-Cruces, R., Royer, J., Caligiuri, M. E., Gambardella, A., Concha, L., Keller, S. S., Cendes, F., Yasuda, C., Bonilha, L., Gleichgerrcht, E., Focke, N. K., Domin, M., Podewills, F. v., Langner, S., Rummel, C., Wiest, R., Martin, P., Kotikalapudi, R., O'Brien, T. J., Sinclair, B., Vivash, L., Desmond, P. M., Alhusaini, S., Doherty, C. P., Cavalleri, G. L., Delanty, N., Kälviäinen, R., Jackson, G. D., Kowalczyk, M., Mascalchi, M., Semmelroch, M., Thomas, R. H., Soltanian-Zadeh, H., Davoodi-Bojd, E., Zhang, J., Lenge, M., Guerrini, R., Bartolini, E., Hamandi, K., Foley, S., Weber, B., Depondt, C., Absil, J., Carr, S. J. A., Abela, E., Richardson, M. P., Devinsky, O., Severino, M., Striano, P., Tortora, D., Hatton, S. N., Vos, S. B., Duncan, J. S., Whelan, C. D., Thompson, P. M., Sisodiya, S. M., Bernasconi, A., Labate, A., McDonald, C. R., Bernasconi, N., and Bernhardt, B. C. (2020b). Network-based atrophy modeling in the common epilepsies: A worldwide ENIGMA study. *Science Advances*, 6(47):eabc6457.

Lawn, N. D., Bamlet, W. R., Radhakrishnan, K., O'Brien, P. C., and So, E. L. (2004). Injuries due to seizures in persons with epilepsy: A population-based study. *Neurology*, 63(9):1565–1570.

Lee, C. Y., Tabesh, A., Spampinato, M. V., Helpern, J. A., Jensen, J. H., and Bonilha, L. (2014). Diffusional kurtosis imaging reveals a distinctive pattern of microstructural alternations in idiopathic generalized epilepsy. *Acta Neurologica Scandinavica*, 130(3):148–155.

Leemans, A. and Jones, D. K. (2009). The B-matrix must be rotated when correcting for subject motion in DTI data. *Magnetic Resonance in Medicine*, 61(6):1336–1349.

Li, M. C. and Cook, M. J. (2018). Deep brain stimulation for drug-resistant epilepsy. *Epilepsia*, 59(2):273–290.

Li, Y., Du, H., Xie, B., Wu, N., Wang, J., Wu, G., Feng, H., and Jiang, T. (2010). Cerebellum Abnormalities in Idiopathic Generalized Epilepsy with Generalized Tonic-Clonic Seizures Revealed by Diffusion Tensor Imaging. *PLoS ONE*, 5(12):e15219.

Liao, W., Zhang, Z., Mantini, D., Xu, Q., Wang, Z., Chen, G., Jiao, Q., Zang, Y.-F., and Lu, G. (2013). Relationship Between Large-Scale Functional and Structural Covariance Networks in Idiopathic Generalized Epilepsy. *Brain Connectivity*, 3(3):240–254.

Liou, J.-y., Ma, H., Wenzel, M., Zhao, M., Baird-Daniel, E., Smith, E. H., Daniel, A., Emerson, R., Yuste, R., Schwartz, T. H., and Schevon, C. A. (2018). Role of inhibitory control in modulating focal seizure spread. *Brain*, 141(7):2083–2097.

Liu, M., Concha, L., Beaulieu, C., and Gross, D. W. (2011). Distinct white matter abnormalities in different idiopathic generalized epilepsy syndromes: Diffusion Abnormalities in IGE Syndromes. *Epilepsia*, 52(12):2267–2275.

Luo, C., Xia, Y., Li, Q., Xue, K., Lai, Y., Gong, Q., Zhou, D., and Yao, D. (2011). Diffusion and volumetry abnormalities in subcortical nuclei of patients with absence seizures: Abnormal Diffusion in Absence Epilepsy. *Epilepsia*, 52(6):1092–1099.

Lytton, W. W. (2008). Computer modelling of epilepsy. *Nature Reviews Neuroscience*, 9(8):626–637.

Marquand, A. F., Rezek, I., Buitelaar, J., and Beckmann, C. F. (2016). Understanding Heterogeneity in Clinical Cohorts Using Normative Models: Beyond Case-Control Studies. *Biological Psychiatry*, 80(7):552–561.

Marten, F., Rodrigues, S., Suffczynski, P., Richardson, M. P., and Terry, J. R. (2009). Derivation and analysis of an ordinary differential equation mean-field model for studying clinically recorded epilepsy dynamics. *Physical Review E*, 79(2):021911.

McDonald, C. R., Hagler, D. J., Ahmadi, M. E., Tecoma, E., Iragui, V., Gharapetian, L., Dale, A. M., and Halgren, E. (2008). Regional neocortical thinning in mesial temporal lobe epilepsy. *Epilepsia*, 49(5):794–803.

McGill, M. L., Devinsky, O., Kelly, C., Milham, M., Castellanos, F. X., Quinn, B. T., DuBois, J., Young, J. R., Carlson, C., French, J., Kuzniecky, R., Halgren, E., and Thesen, T. (2012). Default mode network abnormalities in idiopathic generalized epilepsy. *Epilepsy & Behavior*, 23(3):353–359.

McGill, M. L., Devinsky, O., Wang, X., Quinn, B. T., Pardoe, H., Carlson, C., Butler, T., Kuzniecky, R., and Thesen, T. (2014). Functional neuroimaging abnormalities in idiopathic generalized epilepsy. *NeuroImage: Clinical*, 6:455–462.

Meeren, H., Luijtelaar, G. v., Silva, F. L. d., and Coenen, A. (2005). Evolving Concepts on the Pathophysiology of Absence Seizures: The Cortical Focus Theory. *Archives of Neurology*, 62(3):371.

Meijer, H. G. E., Eissa, T. L., Kiewiet, B., Neuman, J. F., Schevon, C. A., Emerson, R. G., Goodman, R. R., McKhann, G. M., Marcuccilli, C. J., Tryba, A. K., Cowan, J. D., Gils, S. A. v., and Drongelen, W. v. (2015). Modeling Focal Epileptic Activity in the Wilson–Cowan Model with Depolarization Block. *The Journal of Mathematical Neuroscience (JMN)*, 5(1):7.

Mithani, K., Mikhail, M., Morgan, B. R., Wong, S., Weil, A. G., Deschenes, S., Wang, S., Bernal, B., Guillen, M. R., Ochi, A., Otsubo, H., Yau, I., Lo, W., Pang, E., Holowka, S., Snead, O. C., Donner, E., Rutka, J. T., Go, C., Widjaja, E., and Ibrahim, G. M. (2019). Connectomic Profiling Identifies Responders to Vagus Nerve Stimulation. *Annals of Neurology*, 86(5):743–753.

Moeller, F., LeVan, P., Muhle, H., Stephani, U., Dubeau, F., Siniatchkin, M., and Gotman, J. (2010). Absence seizures: Individual patterns revealed by EEG-fMRI. *Epilepsia*, 51(10):2000–2010.

Morgan, V. L., Englot, D. J., Rogers, B. P., Landman, B. A., Cakir, A., Abou-Khalil, B. W., and Anderson, A. W. (2017). Magnetic resonance imaging connectivity for the prediction of seizure outcome in temporal lobe epilepsy. *Epilepsia*, 58(7):1251–1260.

Morgan, V. L., Rogers, B. P., Anderson, A. W., Landman, B. A., and Englot, D. J. (2020). Divergent network properties that predict early surgical failure versus late recurrence in temporal lobe epilepsy. *Journal of Neurosurgery*, 132(5):1324–1333.

Munsell, B. C., Wee, C.-Y., Keller, S. S., Weber, B., Elger, C., Silva, L. A. T. d., Nesland, T., Styner, M., Shen, D., and Bonilha, L. (2015). Evaluation of machine learning algorithms for treatment outcome prediction in patients with epilepsy based on structural connectome data. *NeuroImage*, 118:219–230.

Murakami, H., Wang, Z. I., Marashly, A., Krishnan, B., Prayson, R. A., Kakisaka, Y., Mosher, J. C., Bulacio, J., Gonzalez-Martinez, J. A., Bingaman, W. E., Najm, I. M., Burgess, R. C., and Alexopoulos, A. V. (2016). Correlating magnetoencephalography to stereo-electroencephalography in patients undergoing epilepsy surgery. *Brain*, 139(11):2935–2947.

Narasimhan, S., Kundassery, K. B., Gupta, K., Johnson, G. W., Wills, K. E., Goodale, S. E., Haas, K., Rolston, J. D., Naftel, R. P., Morgan, V. L., Dawant, B. M., González, H. F. J., and Englot, D. J. (2020). Seizure-onset regions demonstrate high inward directed connectivity during resting-state: An SEEG study in focal epilepsy. *Epilepsia*, 61(11):2534–2544.

Nevado-Holgado, A. J., Marten, F., Richardson, M. P., and Terry, J. R. (2012). Characterising the dynamics of EEG waveforms as the path through parameter space of a neural mass model: Application to epilepsy seizure evolution. *NeuroImage*, 59(3):2374–2392.

O'Muircheartaigh, J., Vollmar, C., Barker, G., Kumari, V., Symms, M., Thompson, P., Duncan, J., Koepp, M., and Richardson, M. (2011). Focal structural changes and cognitive dysfunction in juvenile myoclonic epilepsy. *Neurology*, 76(1):34–40.

Otsu, N. (1979). A Threshold Selection Method from Gray-Level Histograms. *IEEE Transactions on Systems, Man, and Cybernetics*, 9(1):62–66.

Otte, W. M., Eijsden, P. v., Sander, J. W., Duncan, J. S., Dijkhuizen, R. M., and Braun, K. P. J. (2012). A meta-analysis of white matter changes in temporal lobe epilepsy as studied with diffusion tensor imaging. *Epilepsia*, 53(4):659–67.

O'Muircheartaigh, J., Vollmar, C., Barker, G. J., Kumari, V., Symms, M. R., Thompson, P., Duncan, J. S., Koepp, M. J., and Richardson, M. P. (2012). Abnormal thalamocortical structural and functional connectivity in juvenile myoclonic epilepsy. *Brain*, 135(12):3635–3644.

Panayiotopoulos, C. P. (2005). Idiopathic Generalized Epilepsies: A Review and Modern Approach. *Epilepsia*, 46(s9):1–6.

Paz, J. T. and Huguenard, J. R. (2015). Microcircuits and their interactions in epilepsy: is the focus out of focus? *Nature Neuroscience*, 18(3):351–359.

Peng, S.-J. and Hsin, Y.-L. (2017). Altered structural and functional thalamocortical networks in secondarily generalized extratemporal lobe seizures. *NeuroImage: Clinical*, 13:55–61.

Pinault, D. and O'brien, T. J. (2005). Cellular and network mechanisms of genetically-determined absence seizures. *Thalamus and Related Systems*, 3(03):181.

Pitkänen, A. and Engel, J. (2014). Past and present definitions of epileptogenesis and its biomarkers. *Neurotherapeutics : the journal of the American Society for Experimental NeuroTherapeutics*, 11(2):231–41.

Pitkänen, A., Löscher, W., Vezzani, A., Becker, A. J., Simonato, M., Lukasiuk, K., Gröhn, O., Bankstahl, J. P., Friedman, A., Aronica, E., Gorter, J. A., Ravizza, T., Sisodiya, S. M., Kokaia, M., and Beck, H. (2016). Advances in the development of biomarkers for epilepsy. *The Lancet. Neurology*, 15(8):843–56.

Platt, J. (1999). Probabilistic outputs for support vector machines and comparisons to regularized likelihood methods. *Advances in large margin classifiers*.

Prevett, M. C., Duncan, J. S., Jones, T., Fish, D. R., and Brooks, D. J. (1995). Demonstration of thalarnic activation during typical absence seizures using H2 15O and PET. *Neurology*, 45(7):1396–1402.

Proix, T., Bartolomei, F., Guye, M., and Jirsa, V. K. (2017). Individual brain structure and modelling predict seizure propagation. *Brain : a journal of neurology*, 140(3):641–654.

Qiu, W., Gao, Y., Yu, C., Miao, A., Tang, L., Huang, S., Hu, Z., Xiang, J., and Wang, X. (2016). Structural Abnormalities in Childhood Absence Epilepsy: Voxel-Based Analysis Using Diffusion Tensor Imaging. *Frontiers in Human Neuroscience*, 10(SEP2016):483.

Rektor, I., Zákopčan, J., Tyrlíková, I., Kuba, R., Brázdil, M., Chrastina, J., and Novák, Z. (2009). Secondary generalization in seizures of temporal lobe origin: Ictal EEG pattern in a stereo-EEG study. *Epilepsy & Behavior*, 15(2):235–239.

Reus, M. A. d. and Heuvel, M. P. v. d. (2013). Estimating false positives and negatives in brain networks. *NeuroImage*, 70:402–9.

Richardson, M. P. (2012). Large scale brain models of epilepsy: dynamics meets connectomics. *Journal of Neurology, Neurosurgery & Psychiatry*, 83(12):1238–1248.

Robinson, P. A., Rennie, C. J., and Rowe, D. L. (2002). Dynamics of large-scale brain activity in normal arousal states and epileptic seizures. *Physical Review E*, 65(4):041924.

Ryvlin, P., Nashef, L., Lhatoo, S. D., Bateman, L. M., Bird, J., Bleasel, A., Boon, P., Crespel, A., Dworetzky, B. A., Høgenhaven, H., Lerche, H., Maillard, L., Malter, M. P., Marchal, C., Murthy, J. M., Nitsche, M., Pataraia, E., Rabben, T., Rheims, S., Sadzot, B., Schulze-Bonhage, A., Seyal, M., So, E. L., Spitz, M., Szucs, A., Tan, M., Tao, J. X., and Tomson, T. (2013). Incidence and mechanisms of cardiorespiratory arrests in epilepsy monitoring units (MORTEMUS): a retrospective study. *The Lancet Neurology*, 12(10):966–977.

Saggio, M. L., Spiegler, A., Bernard, C., and Jirsa, V. K. (2017). Fast–Slow Bursters in the Unfolding of a High Codimension Singularity and the Ultra-slow Transitions of Classes. *The Journal of Mathematical Neuroscience*, 7(1):7.

Scharfman, H. E. (2007). The neurobiology of epilepsy. *Current Neurology and Neuroscience Reports*, 7(4):348–354.

Schmidt, H., Petkov, G., Richardson, M. P., and Terry, J. R. (2014). Dynamics on Networks: The Role of Local Dynamics and Global Networks on the Emergence of Hypersynchronous Neural Activity. *PLoS Computational Biology*, 10(11):e1003947.

Schmidt, H., Woldman, W., Goodfellow, M., Chowdhury, F. A., Koutroumanidis, M., Jewell, S., Richardson, M. P., and Terry, J. R. (2016). A computational biomarker of idiopathic generalized epilepsy from resting state EEG. *Epilepsia*, 57(10):e200–e204.

Schramm, J. (2008). Temporal lobe epilepsy surgery and the quest for optimal extent of resection: a review. *Epilepsia*, 49(8):1296–307.

Schroeder, G. M., Diehl, B., Chowdhury, F. A., Duncan, J. S., Tisi, J. d., Trevelyan, A. J., Forsyth, R., Jackson, A., Taylor, P. N., and Wang, Y. (2020). Seizure pathways change on circadian and slower timescales in individual patients with focal epilepsy. *Proceedings of the National Academy of Sciences*, 117(20):11048–11058.

Shah, P., Ashourvan, A., Mikhail, F., Pines, A., Kini, L., Oechsel, K., Das, S. R., Stein, J. M., Shinohara, R. T., Bassett, D. S., Litt, B., and Davis, K. A. (2019a). Characterizing the role of the structural connectome in seizure dynamics. *Brain*, 142(7):1955–1972.

Shah, P., Bernabei, J. M., Kini, L. G., Ashourvan, A., Boccanfuso, J., Archer, R., Oechsel, K., Das, S. R., Stein, J. M., Lucas, T. H., Bassett, D. S., Davis, K. A., and Litt, B. (2019b). High interictal connectivity within the resection zone is associated with favorable post-surgical outcomes in focal epilepsy patients. *NeuroImage: Clinical*, 23(April):101908.

Sheikh, S. R., Kattan, M. W., Steinmetz, M., Singer, M. E., Udeh, B. L., and Jehi, L. (2020). Cost-effectiveness of surgery for drug-resistant temporal lobe epilepsy in the US. *Neurology*, 95(10):e1404–e1416.

Shorvon, S. D., Bermejo, P. E., Gibbs, A. A., Huberfeld, G., and Kälviäinen, R. (2018). Antiepileptic drug treatment of generalized tonic-clonic seizures: An evaluation of regulatory data and five criteria for drug selection. *Epilepsy & behavior : E&B*, 82:91–103.

Siegel, A. M., Wieser, H. G., Wichmann, W., and Yasargil, G. M. (1990). Relationships between MR-imaged total amount of tissue removed, resection scores of specific mediobasal limbic subcompartments and clinical outcome following selective amygdalohippocampectomy. *Epilepsy Research*, 6(1):56–65.

Silva, F. L. D., Blanes, W., Kalitzin, S. N., Parra, J., Suffczynski, P., and Velis, D. N. (2003). Epilepsies as Dynamical Diseases of Brain Systems: Basic Models of the Transition Between Normal and Epileptic Activity. *Epilepsia*, 44(s12):72–83.

Silva, N. M. d., Cowie, C. J. A., Blamire, A. M., Forsyth, R., and Taylor, P. N. (2020a). Investigating Brain Network Changes and Their Association With Cognitive Recovery After Traumatic Brain Injury: A Longitudinal Analysis. *Frontiers in Neurology*, 11:369.

Silva, N. M. d., Forsyth, R., McEvoy, A., Miserocchi, A., Tisi, J. d., Vos, S. B., Winston, G. P., Duncan, J., Wang, Y., and Taylor, P. N. (2020b). Network reorganisation following anterior temporal lobe resection and relation with post-surgery seizure relapse: A longitudinal study. *NeuroImage: Clinical*, 27:102320.

Sinha, N., Dauwels, J., Kaiser, M., Cash, S. S., Westover, M. B., Wang, Y., and Taylor, P. N. (2016). Predicting neurosurgical outcomes in focal epilepsy patients using computational modelling. *Brain*, 140(2):319–332.

Sinha, N., Wang, Y., Dauwels, J., Kaiser, M., Thesen, T., Forsyth, R., and Taylor, P. N. (2019). Computer modelling of connectivity change suggests epileptogenesis mechanisms in idiopathic generalised epilepsy. *NeuroImage: Clinical*, 21:101655.

Sinha, N., Wang, Y., Silva, N. M. d., Miserocchi, A., McEvoy, A. W., Tisi, J. d., Vos, S. B., Winston, G. P., Duncan, J. S., and Taylor, P. N. (2020). Structural brain network abnormalities and the probability of seizure recurrence after epilepsy surgery. *Neurology*, 96:747725.

Smialowski, P., Frishman, D., and Kramer, S. (2009). Pitfalls of supervised feature selection. *Bioinformatics*, 26(3):440–443.

Smith, E. H. and Schevon, C. A. (2016). Toward a Mechanistic Understanding of Epileptic Networks. *Current Neurology and Neuroscience Reports*, 16(11):97.

Smith, S. J. M. (2005). EEG in the diagnosis, classification, and management of patients with epilepsy. *Journal of Neurology, Neurosurgery & Psychiatry*, 76(suppl 2):ii2.

Smith, S. M., Jenkinson, M., Johansen-Berg, H., Rueckert, D., Nichols, T. E., Mackay, C. E., Watkins, K. E., Ciccarelli, O., Cader, M. Z., Matthews, P. M., and Behrens, T. E. (2006). Tract-based spatial statistics: Voxelwise analysis of multi-subject diffusion data. *NeuroImage*, 31(4):1487–1505.

Spencer, S. (2002). Neural Networks in Human Epilepsy: Evidence of and Implications for Treatment. *Epilepsia*, 43(3):219–227.

Spencer, S. and Huh, L. (2008). Outcomes of epilepsy surgery in adults and children. *The Lancet Neurology*, 7(6):525–537.

Tavakol, S., Royer, J., Lowe, A. J., Bonilha, L., Tracy, J. I., Jackson, G. D., Duncan, J. S., Bernasconi, A., Bernasconi, N., and Bernhardt, B. C. (2019). Neuroimaging and connectomics of drug-resistant epilepsy at multiple scales: From focal lesions to macroscale networks. *Epilepsia*, 60(4):593–604.

Taylor, P. N., Baier, G., Cash, S. S., Dauwels, J., Slotine, J.-J., and Wang, Y. (2013a). A model of stimulus induced epileptic spike-wave discharges. *2013 IEEE Symposium on Computational Intelligence, Cognitive Algorithms, Mind, and Brain (CCMB)*, pages 53–59.

Taylor, P. N., Goodfellow, M., Wang, Y., and Baier, G. (2013b). Towards a large-scale model of patient-specific epileptic spike-wave discharges. *Biological Cybernetics*, 107(1):83–94.

Taylor, P. N., Kaiser, M., and Dauwels, J. (2014a). Structural connectivity based whole brain modelling in epilepsy. *Journal of Neuroscience Methods*, 236:51–57.

Taylor, P. N., Sinha, N., Wang, Y., Vos, S. B., Tisi, J. d., Miserocchi, A., McEvoy, A. W., Winston, G. P., and Duncan, J. S. (2018). The impact of epilepsy surgery on the structural connectome and its relation to outcome. *NeuroImage: Clinical*, 18:202–214.

Taylor, P. N., Wang, Y., Goodfellow, M., Dauwels, J., Moeller, F., Stephani, U., and Baier, G. (2014b). A Computational Study of Stimulus Driven Epileptic Seizure Abatement. *PLoS ONE*, 9(12):e114316.

Tisi, J. d., Bell, G. S., Peacock, J. L., McEvoy, A. W., Harkness, W. F. J., Sander, J. W., and Duncan, J. S. (2011). The long-term outcome of adult epilepsy surgery, patterns of seizure remission, and relapse: a cohort study. *Lancet (London, England)*, 378(9800):1388–95.

Tsamardinos, I., Greasidou, E., and Borboudakis, G. (2018). Bootstrapping the out-of-sample predictions for efficient and accurate cross-validation. *Machine Learning*, 107(12):1895–1922.

Tuch, D. S. (2004). Q-ball imaging. *Magnetic Resonance in Medicine*, 52(6):1358–1372.

Tzourio-Mazoyer, N., Landeau, B., Papathanassiou, D., Crivello, F., Etard, O., Delcroix, N., Mazoyer, B., and Joliot, M. (2002). Automated Anatomical Labeling of Activations in SPM Using a Macroscopic Anatomical Parcellation of the MNI MRI Single-Subject Brain. *NeuroImage*, 15(1):273–289.

Téllez-Zenteno, J. F. and Wiebe, S. (2008). Long-term seizure and psychosocial outcomes of epilepsy surgery. *Current Treatment Options in Neurology*, 10(4):253–259.

Vakharia, V. N., Duncan, J. S., Witt, J., Elger, C. E., Staba, R., and Engel, J. (2018). Getting the best outcomes from epilepsy surgery. *Annals of Neurology*, 83(4):676–690.

Vollmar, C., O'Muircheartaigh, J., Symms, M. R., Barker, G. J., Thompson, P., Kumari, V., Stretton, J., Duncan, J. S., Richardson, M. P., and Koepp, M. J. (2012). Altered microstructural connectivity in juvenile myoclonic epilepsy: The missing link. *Neurology*, 78(20):1555–1559.

Vos, S. B., Tax, C. M. W., Luijten, P. R., Ourselin, S., Leemans, A., and Froeling, M. (2016). The importance of correcting for signal drift in diffusion MRI. *Magnetic resonance in medicine*, 77(1):285–299.

Wang, Y., Goodfellow, M., Taylor, P. N., and Baier, G. (2012). Phase space approach for modeling of epileptic dynamics. *Physical Review E*, 85(6):061918.

Wang, Y., Goodfellow, M., Taylor, P. N., and Baier, G. (2014). Dynamic Mechanisms of Neocortical Focal Seizure Onset. *PLoS Computational Biology*, 10(8):e1003787.

Wang, Y., Trevelyan, A. J., Valentin, A., Alarcon, G., Taylor, P. N., and Kaiser, M. (2017). Mechanisms underlying different onset patterns of focal seizures. *PLOS Computational Biology*, 13(5):e1005475.

Wellmer, J., Quesada, C. M., Rothe, L., Elger, C. E., Bien, C. G., and Urbach, H. (2013). Proposal for a magnetic resonance imaging protocol for the detection of epileptogenic lesions at early outpatient stages. *Epilepsia*, 54(11):1977–1987.

Whelan, C. D., Altmann, A., Botía, J. A., Jahanshad, N., Hibar, D. P., Absil, J., Alhusaini, S., Alvim, M. K. M., Auvinen, P., Bartolini, E., Bergo, F. P. G., Bernardes, T., Blackmon, K., Braga, B., Caligiuri, M. E., Calvo, A., Carr, S. J., Chen, J., Chen, S., Cherubini, A., David, P., Domin, M., Foley, S., França, W., Haaker, G., Isaev, D., Keller, S. S., Kotikalapudi, R., Kowalczyk, M. A., Kuzniecky, R., Langner, S., Lenge, M., Leyden, K. M., Liu, M., Loi, R. Q., Martin, P., Mascalchi, M., Morita, M. E., Pariente, J. C., Rodríguez-Cruces, R., Rummel, C., Saavalainen, T., Semmelroch, M. K., Severino, M., Thomas, R. H., Tondelli, M., Tortora, D., Vaudano, A. E., Vivash, L., Podewils, F. v., Wagner, J., Weber, B., Yao, Y., Yasuda, C. L., Zhang, G., Bargalló, N., Bender, B., Bernasconi, N., Bernasconi, A., Bernhardt, B. C., Blümcke, I., Carlson, C., Cavalleri, G. L., Cendes, F., Concha, L., Delanty, N., Depondt, C., Devinsky, O., Doherty, C. P., Focke, N. K., Gambardella, A., Guerrini, R., Hamandi, K., Jackson, G. D., Kälviäinen, R., Kochunov, P., Kwan, P., Labate, A., McDonald, C. R., Meletti, S., O'Brien, T. J., Ourselin, S., Richardson, M. P., Striano, P., Thesen, T., Wiest, R., Zhang, J., Vezzani, A., Ryten, M., Thompson, P. M., and Sisodiya, S. M. (2018). Structural brain abnormalities in the common epilepsies assessed in a worldwide ENIGMA study. *Brain*, 141(2):391–408.

Wiebe, S., Blume, W. T., Girvin, J. P., Eliasziw, M., and Group, Effectiveness and Efficiency of Surgery for Temporal Lobe Epilepsy Study (2001). A Randomized, Controlled Trial of Surgery for Temporal-Lobe Epilepsy. *The New England Journal of Medicine*, 345(5):311–318.

Wieser, H. G., Blume, W. T., Fish, D., Goldensohn, E., Hufnagel, A., King, D., Sperling, M. R., Lüders, H., and Pedley, T. A. (2008). Proposal for a New Classification of Outcome with Respect to Epileptic Seizures Following Epilepsy Surgery. *Epilepsia*, 42(2):282–286.

Wieshmann, U. C., Milinis, K., Paniker, J., Das, K., Jenkinson, M. D., Brodbelt, A., Crooks, D., and Keller, S. S. (2015). The role of the corpus callosum in seizure spread: MRI lesion mapping in oligodendrogliomas. *Epilepsy Research*, 109(1):126–133.

Wijk, B. C. M. v., Stam, C. J., and Daffertshofer, A. (2010). Comparing Brain Networks of Different Size and Connectivity Density Using Graph Theory. *PLoS ONE*, 5(10):e13701.

Wilson, H. R. and Cowan, J. D. (1972). Excitatory and Inhibitory Interactions in Localized Populations of Model Neurons. *Biophysical Journal*, 12(1):1–24.

Winston, G. P., Cardoso, M. J., Williams, E. J., Burdett, J. L., Bartlett, P. A., Espak, M., Behr, C., Duncan, J. S., and Ourselin, S. (2013a). Automated hippocampal segmentation in patients with epilepsy: Available free online. *Epilepsia*, 54(12):2166–2173.

Winston, G. P., Daga, P., White, M. J., Micallef, C., Miserocchi, A., Mancini, L., Modat, M., Stretton, J., Sidhu, M. K., Symms, M. R., Lythgoe, D. J., Thornton, J., Yousry, T. A., Ourselin, S., Duncan, J. S., and McEvoy, A. W. (2014). Preventing visual field deficits from neurosurgery. *Neurology*, 83(7):604–611.

Winston, G. P., Stretton, J., Sidhu, M. K., Symms, M. R., and Duncan, J. S. (2013b). Progressive white matter changes following anterior temporal lobe resection for epilepsy. *NeuroImage. Clinical*, 4:190–200.

Xue, K., Luo, C., Zhang, D., Yang, T., Li, J., Gong, D., Chen, L., Medina, Y. I., Gotman, J., Zhou, D., and Yao, D. (2014). Diffusion tensor tractography reveals disrupted structural connectivity in childhood absence epilepsy. *Epilepsy Research*, 108(1):125–138.

Yamashita, A., Sakai, Y., Yamada, T., Yahata, N., Kunimatsu, A., Okada, N., Itahashi, T., Hashimoto, R., Mizuta, H., Ichikawa, N., Takamura, M., Okada, G., Yamagata, H., Harada, K., Matsuo, K., Tanaka, S. C., Kawato, M., Kasai, K., Kato, N., Takahashi, H., Okamoto, Y., Yamashita, O., and Imamizu, H. (2020). Generalizable brain network markers of major depressive disorder across multiple imaging sites. *PLOS Biology*, 18(12):e3000966.

Yan, B. and Li, P. (2012). The emergence of abnormal hypersynchronization in the anatomical structural network of human brain. *NeuroImage*, 65:34–51.

Yang, L., Li, H., Zhu, L., Yu, X., Jin, B., Chen, C., Wang, S., Ding, M., Zhang, M., Chen, Z., and Wang, S. (2017). Localized shape abnormalities in the thalamus and pallidum are associated with secondarily generalized seizures in mesial temporal lobe epilepsy. *Epilepsy & Behavior*, 70:259–264.

Yang, T., Guo, Z., Luo, C., Li, Q., Yan, B., Liu, L., Gong, Q., Yao, D., and Zhou, D. (2012). White matter impairment in the basal ganglia-thalamocortical circuit of drug-naïve childhood absence epilepsy. *Epilepsy Research*, 99(3):267–273.

Yeh, F.-C., Badre, D., and Verstynen, T. (2016). Connectometry: A statistical approach harnessing the analytical potential of the local connectome. *NeuroImage*, 125:162–171.

Yeh, F.-C., Panesar, S., Fernandes, D., Meola, A., Yoshino, M., Fernandez-Miranda, J. C., Vettel, J. M., and Verstynen, T. (2018). Population-averaged atlas of the macroscale human structural connectome and its network topology. *NeuroImage*, 178:57–68.

Yeh, F.-C., Tang, P.-F., and Tseng, W.-Y. I. (2013a). Diffusion MRI connectometry automatically reveals affected fiber pathways in individuals with chronic stroke. *NeuroImage: Clinical*, 2:912–921.

Yeh, F.-C. and Tseng, W.-Y. I. (2011). NTU-90: A high angular resolution brain atlas constructed by q-space diffeomorphic reconstruction. *NeuroImage*, 58(1):91–99.

Yeh, F.-C. and Tseng, W.-Y. I. (2013). Sparse Solution of Fiber Orientation Distribution Function by Diffusion Decomposition. *PLoS ONE*, 8(10):e75747.

Yeh, F.-C., Verstynen, T. D., Wang, Y., Fernández-Miranda, J. C., and Tseng, W.-Y. I. (2013b). Deterministic diffusion fiber tracking improved by quantitative anisotropy. *PloS one*, 8(11):e80713.

Yeh, F.-C., Wedeen, V. J., and Tseng, W.-Y. I. (2010). Generalized ${q}$-Sampling Imaging. *IEEE Transactions on Medical Imaging*, 29(9):1626–1635.

Yeh, F.-C., Wedeen, V. J., and Tseng, W.-Y. I. (2011). Estimation of fiber orientation and spin density distribution by diffusion deconvolution. *NeuroImage*, 55(3):1054–1062.

Yeo, B. T. T., Krienen, F. M., Sepulcre, J., Sabuncu, M. R., Lashkari, D., Hollinshead, M., Roffman, J. L., Smoller, J. W., Zöllei, L., Polimeni, J. R., Fischl, B., Liu, H., and Buckner, R. L. (2011). The organization of the human cerebral cortex estimated by intrinsic functional connectivity. *Journal of Neurophysiology*, 106(3):1125–1165.

Yoo, J. Y., Farooque, P., Chen, W. C., Youngblood, M. W., Zaveri, H. P., Gerrard, J. L., Spencer, D. D., Hirsch, L. J., and Blumenfeld, H. (2014). Ictal spread of medial temporal lobe seizures with and without secondary generalization: An intracranial electroencephalography analysis. *Epilepsia*, 55(2):289—295.

Yousif, N. A. B. and Denham, M. (2005). A population-based model of the nonlinear dynamics of the thalamocortical feedback network displays intrinsic oscillations in the spindling (7–14 Hz) range. *European Journal of Neuroscience*, 22(12):3179–3187.

Zalesky, A., Fornito, A., and Bullmore, E. T. (2010). Network-based statistic: Identifying differences in brain networks. *NeuroImage*, 53(4):1197—1207.

Zhang, Z., Liao, W., Chen, H., Mantini, D., Ding, J.-R., Xu, Q., Wang, Z., Yuan, C., Chen, G., Jiao, Q., and Lu, G. (2011). Altered functional–structural coupling of large-scale brain networks in idiopathic generalized epilepsy. *Brain*, 134(10):2912–2928.

Zijlmans, M., Zweiphenning, W., and Klink, N. v. (2019). Changing concepts in presurgical assessment for epilepsy surgery. *Nature Reviews Neurology*, 15(10):594–606.